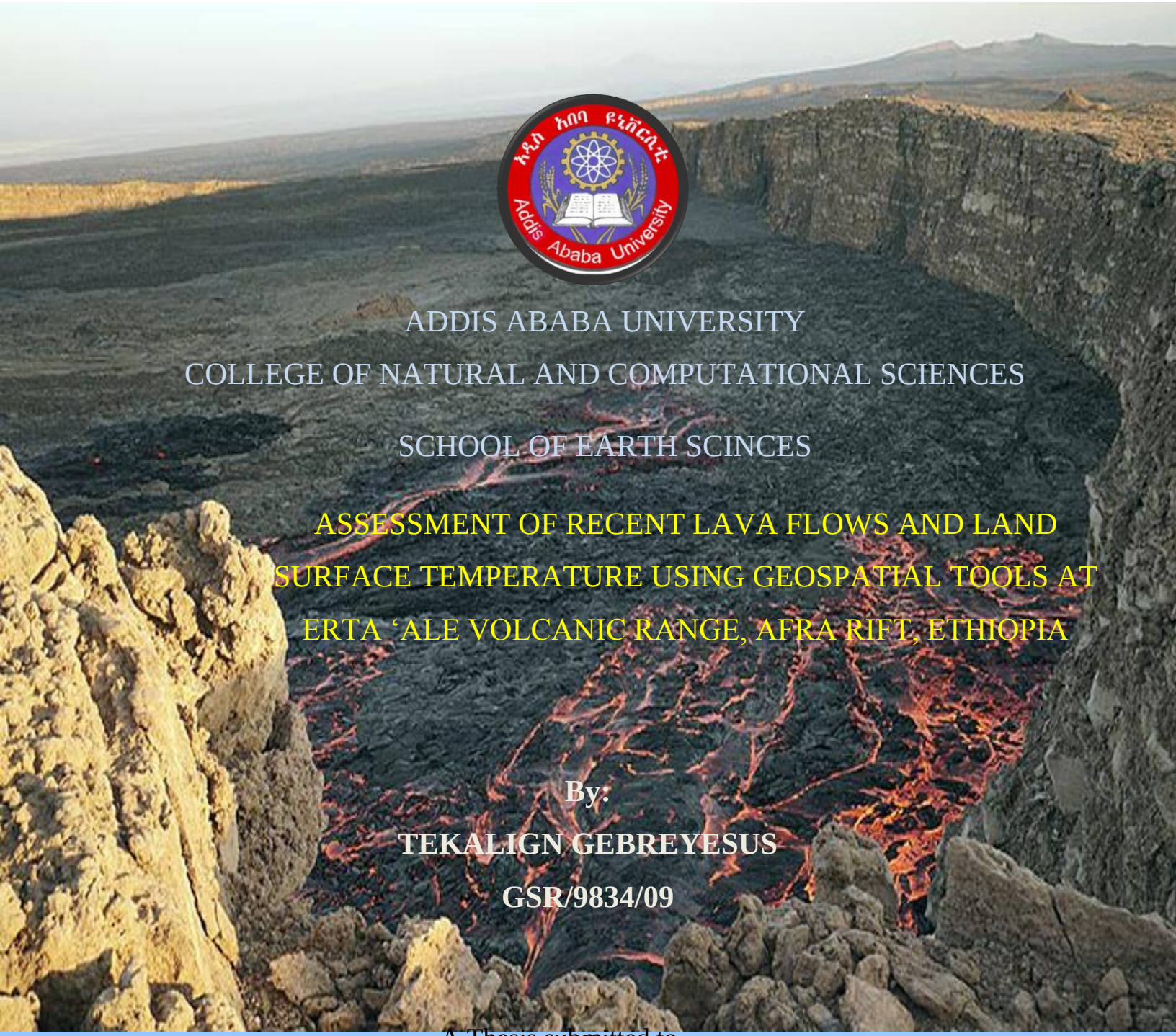

ADDIS ABABA UNIVERSITY

COLLEGE OF NATURAL AND COMPUTATIONAL SCIENCES

SCHOOL OF EARTH SCINCES

ASSESSMENT OF RECENT LAVA FLOWS AND LAND SURFACE TEMPERATURE USING GEOSPATIAL TOOLS AT ERTA ‘ALE VOLCANIC RANGE, AFRA RIFT, ETHIOPIA

By:

TEKALIGN GEBREYESUS

GSR/9834/09

A Thesis submitted to

School of graduate studies of Addis Ababa University in Partial Fulfillment of the requirements for the Degree of Masters of Science in Remote Sensing and Geo-informatics

Cover photo:
(Global volcanic program, 2017)
Erta ‘Ale

Addis Ababa, Ethiopia
May, 2018

ADDIS ABABA UNIVERSITY

COLLEGE OF NATURAL AND COMPUTATIONAL SCIENCES

SCHOOL OF EARTH SCIENCES

ASSESSMENT OF RECENT LAVA FLOWS AND LAND SURFACE TEMPERATURE USING GEOSPATIAL TOOLS AT ERTA ‘ALE VOLCANIC RANGE, AFAR RIFT, ETHIOPIA

By:

TEKALIGN GEBREYESUS

GSR/9834/09

Advisor:

Dr. K. V. Suryabhagavan

Co-Advisor:

Gezahegn Yirgu (Prof.)

A Thesis submitted to

School of graduate studies of Addis Ababa University in Partial Fulfillment of the requirements for the Degree of Masters of Science in Remote Sensing and Geo-informatics

Addis Ababa, Ethiopia

May, 2018

Addis Ababa University

School of Graduate Studies

Declaration

This is to certify that thesis prepared by **Tekalign Gebreyesus**, entitled: "**Assessment of *Recent Lava Flows and Land Surface Temperature using Geospatial Tools at Erta 'Ale Volcanic Range Afar Rift, Ethiopia***" and submitted in partial fulfillment of the requirements for the degree of Masters of Science in Remote sensing and Geo-informatics complies with the regulations of the University and meets the accepted standards with respect to the originality and quality.

By:

Tekalign G/yesus Signature_____ Date_____

Signed by the Examining committee:

Examiner:

1 Dr. Tesfaye Korme Signature_____ Date _____

2 Dr. Ameha Atinafu Signature_____ Date _____

Advisor:

Dr. K.V. Suryabhagavan Signature_____ Date _____

Co-Advisor:

Prof. Gezahegn Yirgu Signature_____ Date _____

Chairman:

Dr. Ameha Atinafu Signature_____ Date _____

Acknowledgements

First of all, I praise and thanks to the "GOD", the Almighty and his Mother Saint "Marry" for his divine blessings showered up on me throughout my life to complete this work and that make all of this happen!

I express my deep sense of gratitude and indebtedness to my thesis guider Dr. K.V. Suryabhagavan, Associate Professor, School of Earth Sciences, College of Natural and Computational Science, Addis Ababa University, for his guidance and valuable suggestions during the research work.

I am equally indebted to my co-advisor Prof. Gezahegn Yirgu, School of Earth Sciences, College of Natural and Computational Science, Addis Ababa University, for his constant encouragement, helpful discussions and valuable suggestions.

I also wish to thank the Ethiopian Geological Survey of Ethiopia for their kindness in providing the requested necessary data and valuable information to carry out this research work.

I am greatly indebted to all my family members for their helpful nature throughout my assignment my Father (G/yesus W/giorgis) and Mother (Mulunesh W/Mariam) for the care and support throughout my life and during this work. without their cooperation, I would not have completed this thesis in time. I am very thankful to Meseret, D for her valuable help rendered and time spared.

My whole-hearted thanks go to all my friends, whose names could not be mentioned separately because of limitations; for their constant encouragement and cooperation. It gives me immense pleasure to thank everyone who helped me write my thesis successfully.

Table of Contents **Page Number**

Acknowledgements i
List of Tables v
List of Figures vi
Acronyms viii
Abstract ix
CHAPTER ONE 1
INTRODUCTION 1
1.1. Background of the study 1
1.2. Statement of the problem 2
1.3. Objectives of the study 4
1.3.1. General Objective 4
1.3.2. Specific Objectives 4
1.4. Research questions 4
1.5. Significance of the study 4
1.6. The scope of the study 5
1.7. Limitations of the research work 5
1.8. Structure of the thesis 5
CHAPTER TWO 6
LITERATURE REVIEW 6
2.1 Introduction 6
2.2 General overview of volcanoes and land surface temperature 6
2.3 Types of volcanoes and their eruption characteristics 6
2.4 Lava eruptions 7
2.5 History of volcanoes 8
2.6 Remote sensing and geo-informatics 10
2.7 Role of geospatial tools in volcanic lava flow mapping 11
2.8 Land surface temperature retrieval algorithm 12
2.8.1 Single channel algorithms 12
2.8.2 Two channel algorithms 12
2.8.3 Dual-angle algorithms 13
CHAPTER THREE 14

MATERIALS AND METHODS 14
3.1. Description of the study area 14
3.1.1. Location 14
3.1.2. The population of the study area 15
3.1.3. Climate and vegetation cover 15
3.1.4. The topography of the study area 15
3.1.5. Geology 16
3.2. Software and description of data 18
3.2.1. Software used 18
3.2.2. Primary data 18
3.2.2.1. Landsat-8 18
3.2.2.2. Sentinel-2A 20
3.2.3. Secondary data 21
3.3. Methodology 21
3.3.1. Preprocessing of satellite images 21
3.3.1.1. Conversion of S2-A MSI bit into byte reflectance 23
3.3.2. Methods of recent lava flow mapping 24
3.3.2.1. Geospatial object-based image classification 24
3.3.2.1.1. Multi-resolution image segmentation algorithms 25
3.3.2.1.2. Object-based image classification stage 26
3.3.2.1.3. Post classification stage 27
3.3.3. Parameters to calculate the land surface temperature 27
3.3.3.1. Sensor spectral radiance and reflectance 27
3.3.3.2. At-sensor atmospheric brightness temperature 29
3.3.3.3. Vegetation fraction from NDVI 31
3.3.3.4. Estimation of land surface emissivity 32
3.3.3.5. Single channel algorithm for LST retrieval 36
CHAPTER FOUR 37
RESULTS 37
4.1 Lava flow map 37
4.1.1 A volcanic eruption in 2016 37
4.1.2 Lava eruptions in 2017 38

4.2 Recent lava flow field area 47
4.3 Recent lava flow direction 49
4.4 Land surface temperature mapping 50
4.5 The correlation of lava flow field and land surface temperature 56
4.6 Model validation 58
4.6.1 Modis Terra LST series product 58
4.6.2 Accuracy assessment 59
CHAPTER FIVE 60
DISCUSSION 60
CHAPTER SIX 64
CONCLUSION AND RECOMMENDATIONS 64
6.1 Conclusion 64
6.2 Recommendations 65
References 66

List of Tables

Table 3.1: Spectral bands of Landsat 8 and its resolution. 20
Table 3.2: Spectral Band of Sentinel–2A data product with its Resolution 21
Table 4.1: Recent lava flow area cover during (2016−2017) 48
Table 4.2: Distance of recent lava flow from the origin to flow direction 49
Table 4.3: Land surface temperature distribution range over the surface (July 2016). 51
Table 4.4: Land surface temperature distribution range over the surface (January 2017)..... 52
Table 4.5: Land surface temperature distribution range over the surface (February 2017)..... 53
Table 4.6: Land surface temperature distribution range over the surface (June 2017)..... 54
Table 4.7: Land surface temperature distribution range over the surface (September 2017)..... 55
Table 4.8: Land surface temperature distribution range over the surface (November 2017). 56
Table 4.9: The correlation statistics of recent lava flow and land surface temperature..... 57
Table 4.10: Statistical comparison of Landsat-8 thermal Band 10 LST and Modis LST during 2016−2017. 59

List of Figures

Figure 2.1: Distribution of Holocene volcanoes in the world (Global Volcanic program, 2017) . 8
Figure 2.2: Southern crater of Erta ‘Ale lava lake (Global Volcanic Program, 2017). 9
Figure 3.1: Location of Erta ’Ale volcanic range Afar rift, Ethiopia..... 14
Figure 3.2: Geological map of the study area (Source: GSE, 2015). 17
Figure 3.3: The general schematic flow chart of the methodology. 23
Figure 3.4: Image segmentation process..... 26
Figure 3.5: Sensor brightness temperature map (July 2016 and January 2017). 30
Figure 3.6: Sensor brightness temperature map (February and May 2017) 30
Figure 3.7: Sensor brightness temperature map in September and November 2017..... 31
Figure 3.8: Land surface emissivity map (July 2016 and January 2017). 34
Figure 3.9: Land surface emissivity map (February and May 2017)..... 35
Figure 3.10: Land surface emissivity map (June and September 2017). 35
Figure 4.1: January 2016 Erta ‘Ale lava flow on its rim. 37
Figure 4.2: Lava lake of Erta ’Ale volcano map (July 2016). 38
Figure 4.3: Erta ’Ale lava flow map (January 19, 2017). 39
Figure 4.4: Erta ’Ale lava flow (January 19, 2017),. 40
Figure 4.5: New fissures eruption and lava flow map (January 29, 2017). 41
Figure 4.6: New lava flow map (February 2017). 42
Figure 4.7: Lava flow map (March 2017)..... 42
Figure 4.8: Lava flow map (April 2017)..... 43
Figure 4.9: Lava flow map (May 2017)..... 44
Figure 4.10: Lava Flow map (June 2017)..... 45
Figure 4.11: Lava flow map (September 2017)..... 45
Figure 4.12: Lava flow map (November 2017). 46
Figure 4.13: Lava flow map (December 2017)..... 46
Figure 4.14: Recent lava flow map during (2016−2017)..... 47
Figure 4.15: Recent lava flow area coverage in Erta ’Ale volcanic range. 48
Figure 4.16: Recent lava flow direction map in Erta ’Ale volcanic range. 50
Figure 4.17: Land surface temperature distribution map (July 2016). 51
Figure 4.18: Land surface temperature distribution map (January 2017)..... 52
Figure 4.19: Land surface temperature distribution map (February 2017)..... 53

Figure 4.20: Land surface temperature distribution map (June 2017). 54
Figure 4.21: Land surface temperature distribution map (September 2017). 55
Figure 4.22: Land surface temperature distribution map (November 2017). 56
Figure 4.23: The correlation analysis map of the recent volcanic lava flows (a) and the LST distribution (b) 57
Figure 4.24: Scatterplot showing correlation of land surface temperature distribution and recent lava flow..... 58
Figure 4.25: Accuracy assessment (a) recent lava flow map and (b) LST 59
Figure 5.1: Erta ‘Ale's lava lake at the S crater on 29 December 2016. 63

Acronyms

ASTER	Advanced Spaceborne Thermal Emission and Reflection Radiometer
ATSR	Along Track Scanning Radiometer
DA	Dual Angle Algorithm
EARS	Eastern African Rift System
ERS-1	European Remote Sensing Satellite
ESA	European Space Agency
GEOB	Geospatial Object-Based
GIS	Geographical Information System
GMES	Global Monitoring for Environment and Society
GSE	Geological Survey of Ethiopia
INSAR	Interferometric Synthetic Aperture Radar
LST	Land Surface Temperature
MER	Main Ethiopian Rift
MSI	Multispectral Imager
MTL	Metadata File
NDVI	Normalized Difference Vegetation Index
OLI	Operational Land Imagery
SAR	Synthetic Aperture Radar
SCA	Single Channel Algorithm
SRTM	Shuttle Radar Topographic Mission
SST	Sea Surface Temperature
SWA	Split Window Algorithm
SWIR	Short Wave Infrared
TIRS	Thermal Infrared Sensor
TOA	Top of Atmosphere
USGS	United States Geological Survey
UTM	Universal Transverse Mercator
WGS	World Geodetic System

Abstract

Assessment of Recent Lava Flows and Land Surface Temperature Using Geospatial Tools at Erta ‘Ale Volcanic Range Afar Rift, Ethiopia.

Tekalign Gebreyesus, MSc. Thesis

Addis Ababa University, May 2018

Volcanoes are generally found where tectonic plates are diverging or converging. Volcano lies on top of a rupture in the crust of Earth that allows hot lava, volcanic ash, and gases to escape from the magma chamber below the surface. This study is carried out in Afar Depression, north eastern part of Ethiopia specifically on Erta ’Ale volcanic range as it is an area of active extensional deformation and basaltic volcanism taking place. Volcanism results a natural hazard that can cause damages in properties and loss of life. Studies indicate that 9.5 million people live within 30 km proximity of this active volcano in Ethiopia. The objective of this study is to assess and map recent lava eruptions and land surface temperatures from Erta’ Ale volcanic vents during the year 2017 using geospatial tools. The data layers used in this research were Landsat-8 and Sentinel2-A multispectral high-resolution satellite images. The methods used are geospatial object-based image classification using eCognition software for recent lava flow mapping and Single-Channel Algorithm (SCA) for Land surface temperature estimation. The requirements for SCA in this study were normalized difference vegetation index (NDVI) based land surface emissivity and at sensor brightness temperature calculation. The result of LST was mapped. This result was also validated by the MODIS Terra LST products for each result. The recent (2016−2017) volcanic lava eruptions were also mapped and the result indicates, in general, there was no lava eruption in 2016 rather the lava lake rising to the rim and falling. The volcanic lava eruption started in January 2017 from the southern crater of Erta ’Ale lava lake and then followed by the development of a new fissural vents and lava eruption on the southern part of Erta ’Ale volcano within 4.5 km. This lava eruption continued until December 2017 and the resulting lava flows have been mapped. The lava flow directions of the eruptions are eastward and westward from the vent. The area of lava flow field was calculated in square kilometer from no flow to the youngest lava flows with maximum area coverage of 24.24 km^2. The calculated lava flow field was positively correlated with the maximum value of land surface temperature distribution.

Keywords: Erta ‘Ale volcano, New fissure eruption, Recent lava flow, Sentinel-2A

CHAPTER ONE
INTRODUCTION

1.1. Background of the study

The Afar Depression is an area of active extensional deformation and basaltic volcanism from which the Red Sea, the Gulf of Aden and the MER radiate (Abbate *et al.,* 2015). It is the product of a tectonic triple junction (the Afar Triple Junction), where the spreading ridges that form the Red Sea and the Gulf of Aden emerge on land and meet the East African Rift (Ring, 2014). Volcanoes are generally found where tectonic plates are diverging or converging. Therefore, the volcano is a rupture in the crust of a planetary-mass object, such as Earth, that allows hot lava, volcanic ash, and gases to escape from a magma chamber below the surface. Volcanism directly creates and degrades landforms of the earth's surface (Gong *et al.,* 2016) and indirectly provides an age for both the land surface over which the erupted material lies and the succession in which it is intercalated (Thouret, 1999).

The erupted materials basalt and silicic products (Barberi and Varet, 1970) were cool in earth' surface after lava eruption. It emits heat energy due to the climatic nature of the earth making land surface temperature variations in space and time measured by satellite remote sensing (Offer *et al.,* 2014). The volcano contains elliptical summit crater with several steep-sided pit craters, one of them containing a lava lake. According to Brown *et al.* (2015) about 59 volcanic edifices in Ethiopia have documented actively during the Holocene. Erupting volcanoes can pose many hazards, not only in the immediate vicinity of the eruption and large eruptions can affect temperature as ash and droplets of sulfuric acid obscure the sun and cool the Earth's lower atmosphere (or troposphere); but, they also absorb heat radiated from the Earth, thereby warming the upper atmosphere (or stratosphere).

Volcanoes need the continuous monitoring of the environment in which they are located in order to ensure safety in the event of volcanic hazards (Rossi *et al.,* 2016). The majority of recent volcanoes are located within the Afar depression; among the active volcanoes, Erta Ale is one of the few volcanoes in the world that have an almost persistent lava lake. There are two active craters (northern and southern) within a larger oval-shaped caldera exhibit periodic fountaining of lava causing lava lake overflows in Erta 'Ale volcanic range. It is an isolated basaltic shield volcano, rising more than 600 m from below mean sea level in Danakil depression.

Remote sensing provides spectral, spatial, and temporal coverage for both geologic mapping and monitoring at numerous volcanoes throughout the world. The use of satellites and aircraft to monitor active volcanic sites and map the products of eruptions has been ongoing for decades. Progressively more complex image processing techniques have been applied to an increasing number of data sets to derive such characteristics in different countries as the amount of magmatic inflation of a region using interferometric radar (Rosen *et al.*, 1996), the presence of hot spots with short-wave infrared (Abrams *et al.,* 1991), and the volume of sulfur dioxide in plumes using thermal infrared TIR. Such monitoring programs, designed to mitigate volcanic hazards, will need to be expanded in the future as population centers continue to encroach upon dangerous volcanoes.

Landsat-8 has increased capabilities such as new spectral bands in the blue part and cirrus cloud-detection portion of the spectrum, two new thermal bands, improved sensor signal-to-noise performance and several developments in radiometric resolution and duty cycle that allows a significant increase in collection of number of images per day (Roy *et al.*, 2014).

Sentinel-2 mission is a land monitoring constellation of two satellites (Sentinel- 2A and Sentinel-2B) providing global optical imagery with 13 spectral bands using MSI (Multispectral Imager) instrument. The temporal resolution of Sentinel-2 is 10 days with one satellite and will be 5 days with 2 satellites that will create a huge amount of Earth Observation data for several research and application projects with a spatial resolution ranging from 10 m to 60 m.

Landsat 8 satellite with 11 bands and spatial resolution ranging from 15 m panchromatic band to 100 m thermal band. Landsat 8 provides 30 m spatial resolution optical imagery with 8 spectral bands via the operational land imager (OLI) sensor with 16 days temporal resolution (Roy *et al.*, 2014). Several studies report the use of thermal infrared sensors to measure temperatures on active volcanoes such as Etna (Bonneville and Kerr, 1985), Erta Ale (Rothery *et al.*, 1988a, 1988b), Lascar (Glaze *et al.*,1989) and Mount Reboubt (Casadevall, 1991).

1.2. Statement of the problem

According to the report of British Geological Survey (1999) volcanic hazards are series problems that cause damage to properties and loss of life i.e. more than 500 million people mostly in developing countries can be lived under the threat of hazard posed by volcanoes. Ethiopia is one of the countries that 59 volcanic eruptions were recorded during the Holocene (Brown *et al.,* 2015).

The Afar rift is a region where extensional tectonic processes and intense volcanic activity are taking place. The lava from Erta 'Ale lava lake and a new fissural eruption was erupted and flown on earth's surface recently. According to Aspinall *et al.* (2011) a number of active volcanoes of Ethiopia are in close proximity to major cities with 9.5 million people living within 30 km of an active volcano. Most of the volcanoes have little or no documented volcanic history or geology and none of the volcanoes is monitored resulting in high uncertainty indices. The eruptive behavior of these volcanos was very active through the year that makes volcanic lava lake and others are pyroclastics that affect atmospheric temperature as ash and droplets of sulfuric acid obscure the sun and cool the earth's lower atmosphere; however, they also absorb heat radiated from the earth, thereby warming the upper atmosphere and destroy the human life and properties.

Previous studies have described the surface temperatures of Erta Ale lava lake (Oppenheimer and Gezahegn, 2002; Burgi *et al.*, 2002; Michael *et al.,* 2013) but the temporal variability of land surface temperature with the co-relation to the volcanic lava flow area was not analyzed yet. Mapping of potentially active volcanoes remains a basic datum for numerous unstudied volcanic indices (Bonneville, 1992). The developing country, Ethiopia has no properly managed data and well-designed hazard mitigation and reduction strategy especially for this natural and suddenly happening volcanic hazard. Field mapping of young lava flows in volcanoes is logistically difficult, and the utility of optical images from aircraft or satellites for this purpose is greatly reduced by persistent cloud cover (Lu *et al.*, 2010) and modern satellite system Sentinel-2 A optical image was used to map and monitor recent volcanic lava flow extent.

The product of pyroclastic materials such as gases that contain chemical elements is added to the surface that reacting with other elements from the atmosphere thereby increasing the surface temperature resulting in climate change and global warming. Now a day climate change is a global alarming issue and surface temperature is one of the variables to measure the climate change. Therefore, this research generally assessed the recent volcanic lava flow and its land surface temperature.

1.3. Objectives of the study

1.3.1. General Objective

The general objective of this research was to investigate the 2017 lava eruptions and consequent land surface temperatures at Erta 'Ale volcanic center, Afar rift, Ethiopia.

1.3.2. Specific Objectives

- To map the timing and extent of lava flows at Erta' Ale volcanic vents using Sentinel-2A satellite images.
- To analyze and map land surface temperature variability due to lava eruptions using Landsat 8 satellite images.
- To assess the extent and direction of recent lava flow using geospatial technology.
- To evaluate the relationship between lava eruptions and land surface temperatures.

1.4. Research questions

- What is the variability of land surface temperature over the study area?
- What is the extent and direction of the recent lava flow at Erta 'Ale volcanic vents?
- what correlation does volcanic lava flow field and land surface temperature results?

1.5. Significance of the study

The present study was conducted in the Erta 'Ale volcanic range Afar rift, Ethiopia. Mapping the current progress (activity) of the volcano is used for future strategic plan and prediction of its impact. At volcanoes situated in remote or politically unstable locations where ground-based monitoring and fieldwork are hazardous or impossible, airborne and spaceborne remote sensing techniques are particularly useful (Abrams *et al*., 1991; Harris *et al*., 1999). The results from studying and mapping of the extent of a lava flows were used as a datum for other researchers. It is intensively important to interpret the current extent of lava flows and prediction of future eruption to manage its hazard. It also used to evaluate and interpret the land surface temperature distribution causing global warming. Remote monitoring of active lava domes provides insights into the duration of continued lava extrusion and detection of potentially associated explosive activity. Retrieving LST from remote sensing data is an important capability for researching the spatial evolution of the regulation of the heated environment at local and global scales.

1.6. The scope of the study

The scope of this research is assessing the recent lava eruptions (2017) of Erta 'Ale volcano and land surface temperatures at Erta 'Ale volcanic range using remote sensing and GIS tools. This research didn't include the process (how and why) lava formation and flow; the factors that govern lava flows and the impact of geologic structures for a volcanic eruption. It mainly covers mapping of the recent lava flows and land surface temperature distribution in Erta 'Ale volcanic range.

1.7. Limitations of the research work

The present study was attempted with all possible efforts in acquiring required inputs in the form of primary and ancillary data collection, interpretation, and analysis. However, the study has encountered certain limitations. The most challenging limitations of this research work are resource limitations, unavailability of high-resolution TIRS data and different image analysis software. Reducing of these limitations made through using the most important technology that measures and record information without direct contact to the object called remote sensing.

1.8. Structure of the thesis

This thesis is organized into six chapters as follows: The first Chapter introduces introduction, statement of the problem, objectives of the study, research questions, the scope of the study, the significance of the study and limitations of the study. Chapter two concentrates on literature review related to this study that used to develop and adopt different methodologies and grasps information about volcanoes and land surface temperature in general. The third chapter focuses on the general methodology followed, the data used in the study and detail explanation of the study area. Chapter four explains the results, which presents the detailed results from collected data. In this section, volcanoes and land surface temperature were mapped. Moreover, evaluating the relationship of lava flow area and land surface temperature, the spatial map was prepared for comparison of changes in each year. Chapter five presents the discussion part and the last chapter six presents conclusions and recommendations. In this section, key findings and critical points that need further treatment has been forwarded as a recommendation for decision-makers and for future research.

CHAPTER TWO
LITERATURE REVIEW

2.1 Introduction

This section presents the basic concepts of volcanic activities. It is one of the most suddenly happening natural hazard making most of the countries lose their property as well human life in its hazard. Natural disasters occur as the result of the action of the natural forces and tend to be accepted as unexpected and costly overall in terms of loss of human lives and resources. The disaster prevention and preparedness of natural disasters result from forces of climate and geology (Lelisa Seena and Kifle woldemariam, 2006).

2.2 General overview of volcanoes and land surface temperature

Volcanic activity is a surface manifestation of a disordered state within the Earth's interior, which has led to the melting of rock material and the consequent formation of magma. This magma travels to the surface, where it is extravagated from either a fissure or a central vent. In some cases, instead of flowing from the volcano as lava, the magma is exploded into the air by the rapid escape of the gases within it. The fragments produced by the explosive activity of volcanoes are collectively named as pyroclastic materials (Bell, 2002).

Land surface temperature (LST) means the temperature of the surface which we measure directly from the surface of objects. It is also referring to skin temperature of the surface. When it rises it causes environmental unbalance situation like melts in glacier, vegetation change, climatic condition of monsoon countries leading to unpredictable rainfall. It is measured in Kelvin. Thermal infrared remote sensing technology has become one of the important means to study the thermal characteristic of the land surface (Latif, 2014). Land surface temperature (LST) is a key parameter in the physics of the earth surface through the process of energy and water exchange with the atmosphere, which plays an important role in a wide variety of scientific studies, such as ecology, hydrology, and global change studies (Yu *et al.*, 2014).

2.3 Types of volcanoes and their eruption characteristics

The form and structure that a volcano adopts depend upon the type of magma feeder channel, the character of the material emitted and the number of eruptions that occur. The feeder channel is either a central vent or a fissure, which give rise to radically different forms that built largely of pyroclasts grow in height much more rapidly than do those formed of lavas.

The number of eruptions that take place from the same vent allows the recognition of monogenetic (single eruption) and polygenetic (multiple eruptions) volcanoes. Monogenetic central-vent volcanoes are always small and have a simple structure, the eruptive center moving on after the eruption. Example of this type of volcanoes is Paricutin in Mexico. Monogenetic volcanoes do not occur alone but are clustered in fields. Polygenetic central-vent volcanoes are much larger and more complicated. Fissure volcanoes are always monogenetic. The composition and viscosity of magma influence its eruption. For instance, acid magmas are more viscous than basic and so gas cannot escape as readily from them (Bell, 2002). As a consequence, the more acid, viscous magmas are generally associated with the explosive activity, and the volcanoes they give rise to may be built mainly of pyroclastic. Alternatively, fluid basalt magmas construct volcanoes that consist of piles of lavas with very little pyroclastic material.

Eruptions can be classified as effusive or explosive according to the violence with which they occur. Low-viscosity magmas escape as lava flows from effusive volcanoes, whereas if magma has a high viscosity the eruption is explosive. Volcanic eruptions also can be classified on the basis of their size, that is, on the amount of ejectment that is erupted. The most volcanic material is of basaltic composition (Barberi and Vareti, 1970). It is generated within the upper mantle, where temperatures approach the fusion point of the material from which they are derived. Their development appears to be associated with huge rifts and thrusts that fissure the crust and extend into the mantle. However, the small, local magma chambers that supply individual volcanoes need not be located at such depths (Bell, 2002).

2.4 Lava eruptions

Volcanic lava rises from the magma chamber to reach the earth's surface and depending upon the topography of the area start to flow down the slope. The rate of a lava flow can be determined by the gradient of the slope down it moves and its viscosity that governed by its composition, temperature and volatile content (Bell, 2002). This mean lava flow becomes faster on its source and within the distance, it slows due to the contact with the ground, lava becomes cool. Lava flows are the outpouring of hot, molten rock that spread across the ground. They advance slowly enough to allow people to escape, but anything in the pathway of a lava flow can be damaged or destroyed. Buildings and vegetation are commonly set on fire. Land can be rendered unproductive or uninhabitable (Aspinal *et al.,* 2011).

2.5 History of volcanoes

There are an estimated 550 historically active volcanoes and 1300 active volcanoes that have evidence of eruptions during the Holocene (10000 years) in the world (Sparks *et al*., 2013). The East African rift, one of the world's most dramatic extensional structures, has produced the volcanoes ranging from the massive Kilimanjaro to vents in Ethiopia's Danakil Depression that lie below mean sea level (Ring, 2014). Two neighboring volcanoes in Zaire's (today's Democratic Republic of the Congo) Virunga National Park, Nyamuragira, and Nyiragongo, are responsible for nearly two-fifths of Africa's historical eruptions (Simpkin and Siebert, 1994).

The Ethiopian region records about one billion years of geological history and the currently elevated topography of the Ethiopian plateaus are the result of profuse volcanic lava accumulation and successive uplift (Abbate *et al*., 2015). The distribution of active volcanoes around the world is shown in (Fig 2.1). The red points represent the distribution of active volcanoes.

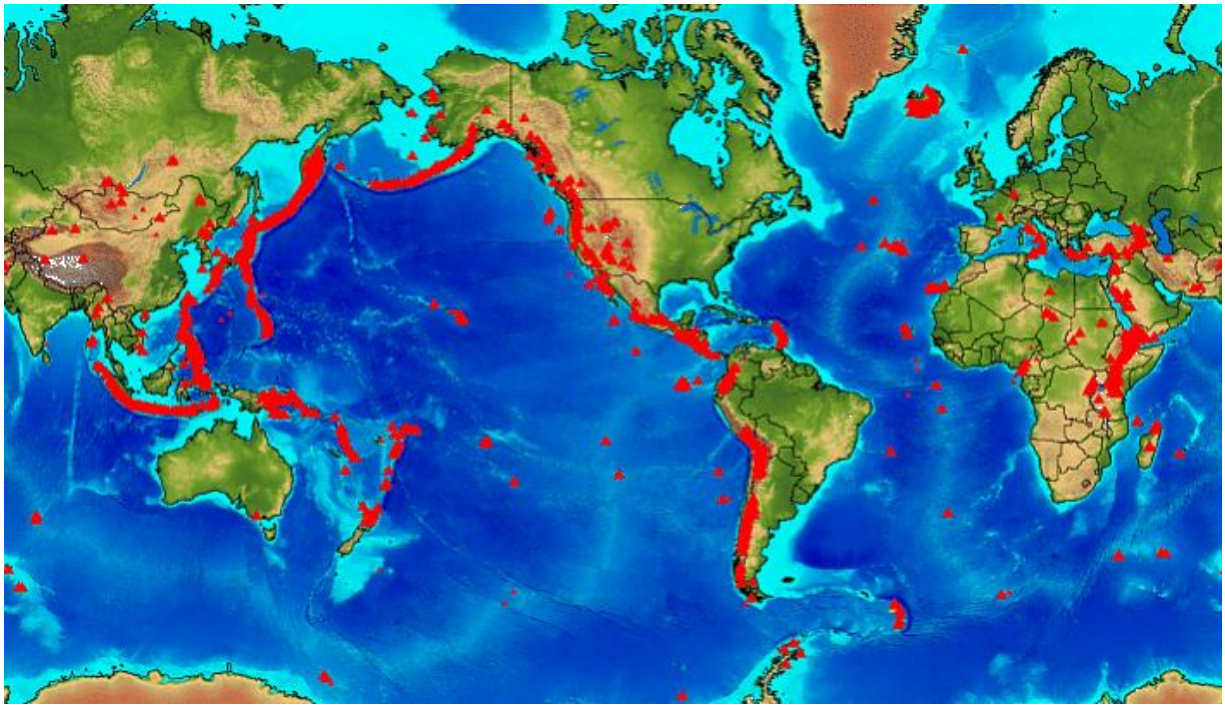

Figure 2.1: Distribution of Holocene volcanoes in the world *(*Global Volcanic program, 2017*)*

The evidence of volcanism associated with rifting in the EARS indicates a long and complex history (Baker *et al.,* 1972; Wagde *et al.,* 2016).

The Afar region is a quasi-triangularly shaped depressed area at the intersection of the Red Sea, Gulf of Aden, and the Main Ethiopian Rift (MER). Due to its 25-million year- long history of rifting and incipient of oceanization, volcanic rocks cover wide areas of the Afar depression (Abbate *et al*., 2015). In north Afar, volcanic edifices are elongate shields with axial fissures (eg. Alu-Dalafilla, Erta Ale, Alayta). The Erta 'Ale lava lake crater was shown in (Fig 2.2). Further south in Afar, central grabens within a faulted and fissured terrain and a central vent area with a subsided edifice are typical (Dubbahu-Manda Hararo, Ardoukoba, Kammourta) (Barnie *et al.*, 2015).

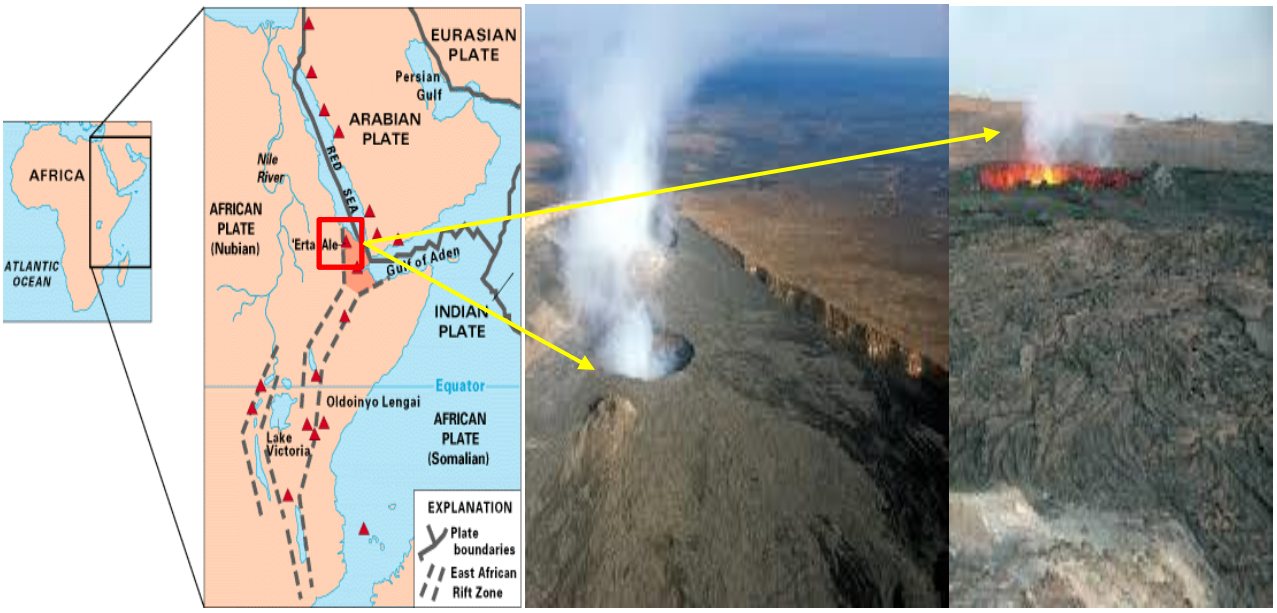

Figure 2.2: Southern crater of Erta 'Ale lava lake (Global Volcanic Program, 2017).

Volcanoes display a wide range of eruption styles, such as lava flows or domes, explosive eruptions that eject volcanic products into the atmosphere and this style and evolution are also dictated by the fluid mechanics governing magma ascent (Gonnermann and Manga, 2007). Effusion rate is critical for assessing lava flow hazards and may be estimated by direct measurements or from the repeated mapping of active or newly emplaced lava flows (Naranjo *et al.*, 2016). According to Aspinal *et al* (2011), volcanoes are very diverse in their styles of the eruption, in their magnitudes, intensities, and frequencies of the eruption. This variety comes about because the processes of magma generation in the earth's interior, the processes that allow magma to reach the Earth's surface and the interaction of erupting volcanoes with surface environments are complex.

Although volcanoes can be broadly classified into different types based on magma chemistry, size and dominant eruptive styles (Gonnermann and Manga, 2007; Gezahegn Yirgu, 2009), each volcano has some distinctive characteristics and each of its eruptions is unique in certain ways. There are several different kinds of volcanic products that make destruction and loss of life such as bombs and blocks, tephra, pyroclastic flows and surges, Lahars and Floods, Volcanic earthquakes, Gas emission (Bell, 2002; Aspinal *et al.*, 2011).

Hazards associated with volcanic activity include destructive floods caused by sudden melting of the snow and ice that cap high volcanoes, or by heavy downfalls of rain (vast quantities of steam may be given off during an eruption), or the rapid collapse of a crater lake (Bell, 2002). These hazards directly or indirectly cause several damages to buildings, vegetation, land, and life living on earth. In general, volcanic hazards are the natural hazard that causes the destruction of properties and loss of life where proximity to active edifices of the volcano through the world. Volcanoes may generate a wide variety of phenomena that can endanger the environment, people, and civil infrastructures. Therefore, volcanic hazard assessment is of paramount importance for the safeguard of the resources exposed to volcanic hazards (Damiani *et al*., 2006).

2.6 Remote sensing and geo-informatics

The Definition of remote sensing in broadest sense is the measurement or acquisition of information of some property of an object or phenomenon, by a recording device that is not in physical or intimate contact with the object or phenomenon under study; e.g., the utilization at a distance (as from aircraft, spacecraft, or ship) of any device and its attendant display for gathering information pertinent to the environment, such as measurements of force fields, electromagnetic radiation, or acoustic energy . The technique employs such devices as the camera, lasers, and radio frequency receivers, radar systems, sonar, seismographs, gravimeters, magnetometers, and scintillation counters (http://www.vtt.fi/ out/rs/ virtual/ defin.html).

Geographical information system is in essence a central repository of an analytical tool for geographic data collected from various sources (Galati, 2006). Remote sensing and geoinformatics are the new geospatial technology that widely used in different application areas in geoscience. Geology is one of the remote sensing application areas that involve the study of landforms, structures, and the subsurface, to understand physical processes creating and modifying the earth's crust.

Geological applications of remote sensing include: surficial deposit or bedrock mapping, lithological mapping, structural mapping, sand and gravel (aggregate) exploration/ exploitation, mineral exploration, hydrocarbon exploration, environmental geology, geobotany, baseline infrastructure, sedimentation mapping and monitoring, event mapping and monitoring geo-hazard mapping and planetary mapping (Levin, 1999). The appearance of geographic information systems (GIS) in the mid- 1960s reflects the progress in computer technology and the influence of quantitative revolution in geography. GIS has evolved dramatically from a tool of automated mapping and data management in the early days into a capable spatial data-handling and analysis technology and, more recently, into geographic information science (Weng, 2010). A geographical information system is the integration of computer package specifically designed for the use of geographical data that performs the comprehensive range of data handling tasks (Weng, 2010).

2.7 Role of geospatial tools in volcanic lava flow mapping

Field mapping of a young lava flow or any volcanic eruption products is logically difficult that remote sensing and GIS (geospatial tools) have the capability to collect information, process, manipulate the data, analyze and present the end result which is geographically referenced. The volcanology community has long recognized the advantages of multispectral and Synthetic Aperture Radar (SAR) remote sensing (RS) techniques. Satellite data in the visible, infrared, and thermal wavelength regions contain reflectance and emittance information about lava surfaces of different origin and age, and therefore can be used to distinguish different lava flows (Lu *et al.*, 2004). Moderate to high spatial resolution and 3D remote sensing (RS) offers a low–cost route to mapping and assessing hazards at volcanoes worldwide. The capabilities of RS techniques are reviewed and an update of recent developments provided, with emphasis on low-cost data, including optical (Landsat, ASTER, SPOT, CORONA), topographic (3D ASTER, SRTM) and SAR data. Applications developed here illustrate capabilities of relevant RS data to identify and map the whole range of hazardous volcanic terrains and derive quantitative data, focusing on mapping and monitoring of volcanic morphology (Kervyn, 2007).

The relation of volcanic activities and geospatial tools (Kervyn *et al*., 2007) Satellite data enables study of diverse volcanic phenomena including Detect hot areas, their temporal and spatial patterns; monitor volcanic clouds; map recently-erupted volcanic or volcano-related deposits such as lahars, debris avalanches;

discriminate fresh volcanic rock surfaces in terms of mineralogical, textural and compositional differences; distinguish weathered volcanic surfaces and assess the terrains' relative age; or identify mechanically weak sectors in a volcanic edifice, characterize volcano morphology and study its changes and assess ground deformation using Interferometric Synthetic Aperture Radar (Zebker *et al.,* 2000). Different kinds of remote sensing technologies were used to monitor and map the volcanic hazards and lava lubes in active volcanic edifices in which difficult to direct measurement of the lava intensity using such as ground penetrating radar (Miyamoto *et al.,* 2005).

2.8 Land surface temperature retrieval algorithm

Different methods and algorithms were developed to retrieve land surface temperature from the thermal remote sensing both single channel and two thermal bands like Split-Window algorithms (SW), Dual Angle algorithm (DA), the Single-Channel algorithm (SC) etc. (Li *et al*., 2013; Latif, 2014). Each algorithm has its own parameters to calculate land surface temperature. For example, split window algorithm requires top of atmospheric brightness temperature and emissivity of the material.

2.8.1 Single channel algorithms

This algorithm mainly used to estimate land surface temperature from one thermal band of the sensor (Sobrino *et al*., 2004) originally developed for Landsat TM-6 and also called mono-window algorithm. It utilizes the radiance measured by a sensor in a single channel to retrieve LST using the general radiance transfer equation.

2.8.2 Two channel algorithms

This algorithm is also called split-window algorithm because it uses two thermal bands of the sensor to retrieve land surface temperature. Other than Landsat 8, sensors have only one thermal band, while TIRS of Landsat 8 has two spectrally adjacent thermal bands called band10 and band11 that is located in the atmospheric window between 10 μm and 12 μm. Split-window (SW) algorithm is suitable and most widely used for LST retrieval due to the simplicity and robustness (Yu *et al*., 2014).

Single channel algorithm is also applicable for land sat 8 thermal sensors. The USGS Landsat website has recommended to use band 10 for SW algorithm. Result for LST retrieval from band 11 show larger uncertainty than band 10, which is consistent with the announced TIRS calibration issue (Yu *et al*., 2014).

2.8.3 Dual-angle algorithms

The multi-angle method is in accordance with different atmospheric absorptions because of the differential path-lengths associated with observing the same object from various viewing angles (Sobrino *et al.,* 1996; Jin *et al.,* 2015). This method was primarily developed based on the first sensor to operate in biangular-mode, the Along Track Scanning Radiometer (ATSR) onboard the first European Remote Sensing Satellite (ERS-1). ATSR can achieve a dual-angle observation of the same region of the Earth's surface within about two minutes. One viewing angle is the with a zenithal angle from 0° to 21.6°, and the other is the forward view with a zenithal angle from 52° to 55° (Jin *et al*., 2015). Assuming that the LST and SST are independent on the VZA and that the atmosphere is horizontally uniform and stable over the observation time, Prata (1993 and 1994) derived a dual-angle method to retrieve the SST and the LST from ATSR data. Sobrino *et al.* (1996) later proposed an improved dual-angle algorithm that incorporates the emissivity on at nadir and the emissivity of at forwarding view.

CHAPTER THREE

MATERIALS AND METHODS

3.1. Description of the study area

The Afar Triangle (also called the Afar Depression) is a geological depression caused by the Afar triple junction, which is part of the Great Rift Valley in East Africa. The Depression overlaps the borders of Eritrea, Djibouti and the entire Afar region of Ethiopia; and it contains the lowest point in Africa, Lake Asal, Djibouti, at 155 m (or 509 ft) below mean sea level.

3.1.1. Location

The Afar depression, is largely desert scrubland with shallow salty lakes and long chains of volcanoes. According to Barberi and Varet, (1970) the Erta 'Ale volcanic range extends from the salt plain in the north, up to lake Afreda in the south. It is geographically bounded by latitude 13º 00' 52"−14º 8' 37"N and longitude 40º05'47"−41º 05' 11"E covering a total area of 2350 km^2. The current study area includes the whole Erta 'Ale volcanic range and the surrounding environment with a total area of 6970 km^2 which is shown (Fig 3.1).

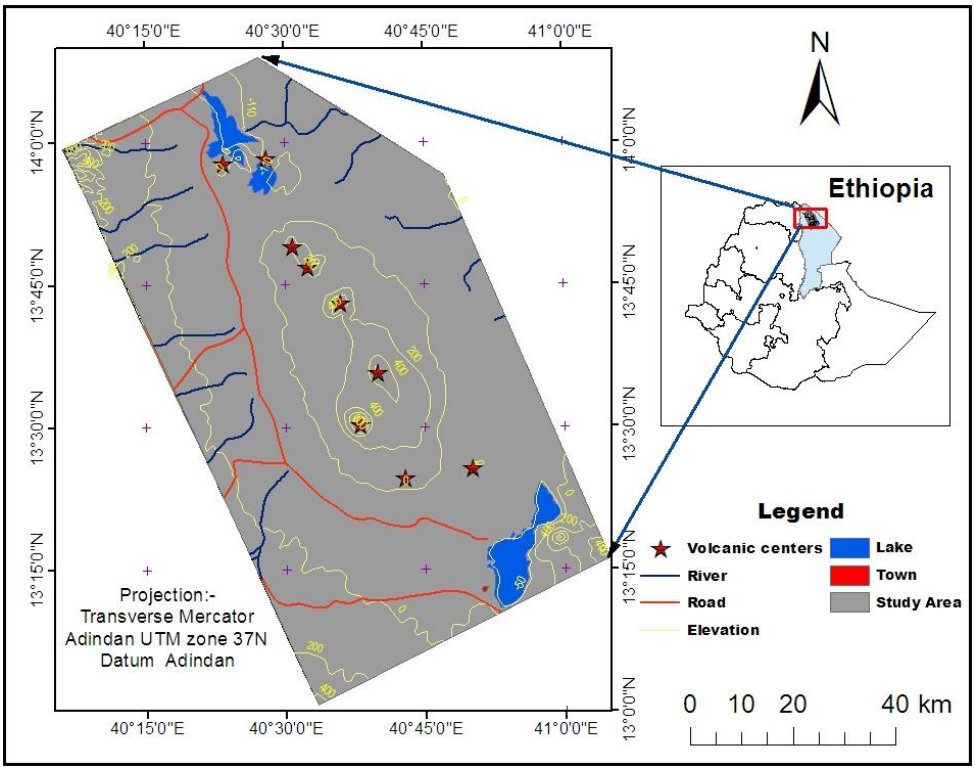

Figure 3.1: Location of Erta 'Ale volcanic range Afar rift, Ethiopia.

3.1.2. The population of the study area

The population of Afar region is largely rural and nomadic. The 2007 E.C census report of Central Statistical Agency describes the total number of Afar population is around 1,276,374. There are about 1.4 million Afar live in three countries: Ethiopia, Djibouti, and Eritrea. Afar is the principal language of the region and it is most closely related to Saho (Ethiopia and Eritrea), and more distantly related to the Somali and Oromo groups of languages. Islam (Sunni) is the principal religion. The region is well known for its early hominid fossil finds including 'Lucy', an Australopithecus afarensis, discovered in 1974, which lived about 3.2 million years ago and more recently in the summer of 2007 the discovery of hominid remains 3.5 – 3.8 million years old.

3.1.3. Climate and vegetation cover

The study area is climatically categorized as arid and semi-arid with temperatures vary from 30^{o}C in highlands to 50^{o}C in summer lowlands. The area receives an annual rainfall of less than 500 mm. The main rainy season falls in the months of July–August and the short rainy season occurs in April–May and the area have bimodal rainfall pattern. The vegetation distribution of the area is mainly dependent on the climate condition of the area. Ethiopia has different types of indigenous vegetation and wildlife. Most commonly vegetation cover types in the study area are woodland, bushland, shrubland, grassland, seasonal marshes and swamps (Central Statistical Agency of Ethiopia, 2007).

3.1.4. The topography of the study area

The Afar Depression is bounded in the east by the NNW-trending Danakil block which extends from the Gulf of Tajura in the southeast to the Gulf of Zula in the northwest. The central part of the Danakil block forms the highest topography where it reaches 2130 m above mean sea level (Alebachew Beyene and Mohamed Abdeselam, 2005). The northern Afar is a low-lying region, alternatively known as the Danakil Depression, which narrows towards the Gulf of Zula. NNW-trending structures, dominate this region. The Ethiopian plateau in the west and the Danakil block in the east bound the northern Afar. The 200 m general elevation of the northern Afar gets progressively lower towards a central zone within the Danakil Depression known as Dallol. At Dallol the elevation drops to 120 m below mean sea level (Vareti, 1973). Despite its generally low elevation, the Danakil Depression is characterized by a number of shield volcanoes such as Erta Ale, Tat Ale, and Alyata. The northern Afar merges to the south with the southwestern and the east-central Afar (Alebachew Beyene and Mohamed Abdeselam, 2005).

3.1.5. Geology

The Afar depression of Ethiopia is a part of the Afro-Arabian rift system which extends 6500 km from Jordan to Dead Sea rift through the red sea, the Gulf of Aden and East Africa rifts (Alebachew Beyene and Mohamed Abdeselam, 2005; Abbate *et al*., 2015). The geology of Danakil depression consists of Precambrian basements, Tertiary and Quaternary volcanic rocks. According to (Alebachew Beyene and Mohamed Abdeselam, 2005) the geological units of the Afar Depression and marginal areas can be divided into four broad groups. The first one is a Neoproterozoic basement, Mesozoic sedimentary rocks, and Eocene–Miocene basalts. This group represents Arabian-Nubian shields that is occupying a part of Danakil and Ali-Sabieh blocks. The second group of geologic units in Afar depression is Miocene igneous rocks. This group of geologic units mainly covers the Mesozoic sedimentary rocks on both the Ethiopian and the Somalian Plateaux and some parts of the marginal areas. The third group is Pliocene volcanic rocks which cover most of the Afar depression. And the last is Quaternary volcanic and sedimentary rocks. This group also covers the Afar depressions which are composed of basaltic flows, scoria cones, and silicic rocks.

Danakil depression is the most volcano-tectonically active zone with several active volcanoes like Erta' Ale, Tat Ale, Gada Ale, Alu, Dalaffila, Borale Ale, Ale Bagu and HayliGub which are all oriented in Northwest-Southeast trends (Geological Survey of Ethiopia, 2015). According to a Geological Survey of Ethiopia (2015), the fault belts of Afar depression can generally be explained in terms of crustal extension acting perpendicular to nearest of the three plate boundaries converging on Afar, problems arise with some intersecting and abutting fault belts in central Afar.

The central part of the Afar Depression is dominated by lowland plains corrugated by horsts and grabens and rare local high relief peaks representing shield volcanoes (Eagles *et al*., 2002; Alebachew Beyene and Mohamed Abdeselam, 2005). According to Abbate *et al*. (2015) the Afar volcanic activities can be assigned to the first stage of continental rifting which lasted about twenty million years, starting from 25 Ma, and a later stage which commenced 4 Ma during which the oceanic floor in the central portion of Afar began to develop.

Two-third of Afar depression extensive volcanic sequence connected with the second stage which is called Plio-Pleistocene Afar Stratoid Series (Abbate *et al*., 2015). There are different types of geological units recorded in Eastern Africa Rift system. Afar depressions or Danakil depression is one of the areas that different tectonic activities can occur.

The Danakil depression is floored principally by Pliocene and younger volcanic rocks, most importantly by the Afar Stratoid series. They are by far the most important geological units in terms of coverage and preservation of igneous features and tectonic activities. The basaltic flows, scoria cones, and alkaline to peralkaline silicic rocks were erupted locally in the Danakil Depression during Quaternary in particular over the past 1 million years. In this zone, widespread fields of fissure lavas are covered by products from spatter cones and explosive phreatic craters. The Continual opening of the Danakil Depression enabled the plate to subside allowing ingression of the sea to inland. This results in deposition of thick salt plain in the south (Mesfin Asfaw and Yohannes Ermias, 2014). Geological setting of the study area and its description are indicated in (Fig 3.2).

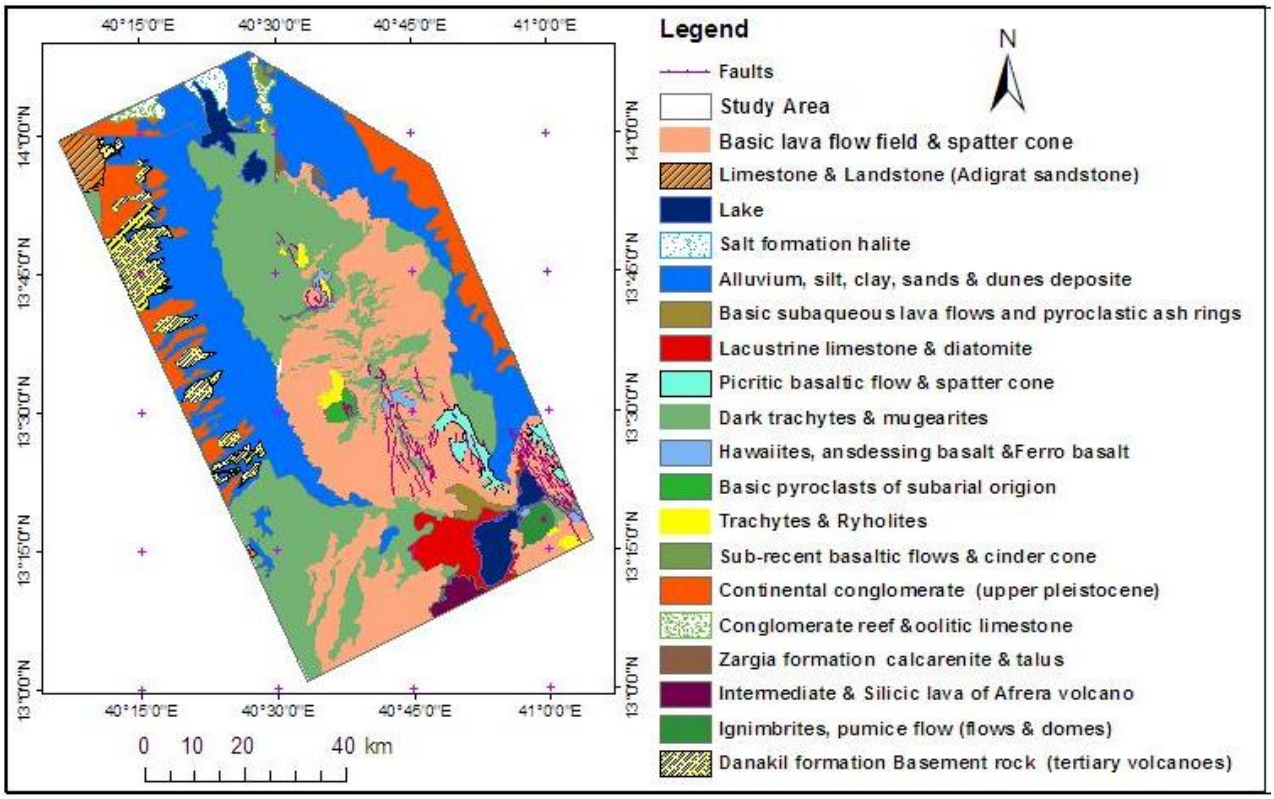

Figure 3.2: Geological map of the study area (Source: GSE, 2015).

3.2. Software and description of data

3.2.1. Software used

In order to achieve the objectives of this study, the following software were utilized:

- ✓ **ERDAS Imagine 2014:** This was used for satellite image pre-processing and post-processing including layer stacking and mosaic.
- ✓ **ArcGIS 10.3:** ArcGIS 10.3 was used for storing and managing geographic data in geodatabase package, compile and edit GIS datasets and display and analyze spatial data in both vector and raster format.
- ✓ **Impact tool software:** This was used for pre-process and layer stacking the Sentinel–2A satellite image.
- ✓ **Trimble's eCognitions software:** eCognition software used for geospatial object-based image classification and image analysis.
- ✓ **Envi 5.1:** This was used for satellite image pre-processing
- ✓ **Microsoft Office Package (2016):** Provides the necessary environment for MS Excel, MS Word, MS Powerpoint and MS Access.

3.2.2. Primary data

Quality of the input data determines the overall work of scientific research result and findings. Especially GIS and remote sensing technology require the best quality of dataset that representing the resolution i.e. (spatial, spectral, radiometric and temporal resolution of data or image) depend upon the project. Remote sensing datasets having very high–resolution imageries are costy and not accessible easily. There are many free and open to access through their website earth resources datasets. The primary datasets that used to compile this research work were mostly satellite imageries i.e. Landsat 8 and Sentinel-2A optical imageries, Digital elevation model, and Google earth images.

3.2.2.1. Landsat-8

According to USGS Landsat (Landsat-8, 2016) data user handbook, the Landsat Program has provided over 40 years of calibrated high spatial resolution data of the Earth's surface to a broad and varied user community including agribusiness, global change researchers, academia, state and local governments, commercial users, national security agencies, the international community, decision-makers, and the public.

Therefore, Landsat images provide information that meets the broad and diverse needs of business, science, education, government, and national security. The mission of the Landsat Program is to provide repetitive acquisition of moderate-resolution multispectral data of the Earth's surface on a global basis. Landsat represents the only source of global, calibrated, moderate spatial resolution measurements of the Earth's surface that are preserved in a national archive and freely available to the public. Landsat-8 is an American Earth observation satellite launched on February 11, 2013. It is the eighth satellite in the Landsat program; the seventh to reach orbit successfully (Landsat 8, 2016). Landsat 8 carries two push-broom instruments: The Operational Land Imager (OLI) and the Thermal Infrared Sensor (TIRS).

The spectral bands of the OLI sensor provide enhancement from prior Landsat instruments, with the addition of two spectral bands: a deep blue coastal / aerosol visible channel (band 1) specifically designed for water resources and coastal zone investigation, and a new shortwave infrared channel (band 9) allowing scientists to measure water quality and improve detection of high, thin clouds. (Gao and Kaufman, 1995). The TIRS instrument collects two spectral bands for the wavelength covered by a single band on the previous TM and ETM+ sensors. This band allows users to apply per pixel filters to the Landsat 8 Operational Land Imager (OLI)-only and Landsat-8 OLI/Thermal Infrared Sensor (OLI/TIRS)-combined data products. It consists of nine spectral bands with a spatial resolution of 30 meters for Bands 1 to 7 and 9. New band 1 (ultra-blue) is useful for coastal and aerosol studies. New band 9 is useful for cirrus cloud detection. The resolution for Band 8 (panchromatic) is 15 m.

Thermal bands (TIRS) 10 and 11 are useful in providing more accurate surface temperatures and are collected at 100 meters. Approximate scene size is 170 km north−south by 183 km east−west but this product for the end-users are resampled to 30 meters in delivered data product (http:// landsat.usgs.gov/ best spectral bands to use. php) which are shown in (Table 3.1).

Table 3.1: Spectral bands of Landsat 8 and its resolution.

No	Spectral Bands	Wavelength (μm)	Resolution (m)
1	Band 1-Coastal/aerosol	0.43−0.45	30
2	Band 2- Blue	0.45−0.51	30
3	Band 3-Green	0.52−0.60	30
4	Band 4-Red	0.63−0.68	30
5	Band 5-Near Infrared	0.84−0.88	30
6	Band 6-Short wavelength Infrared	1.56−1.66	30
7	Band 7-Short wavelength Infrared	2.10−2.30	30
8	Band 8-Panchromatic	0.50−0.68	15
9	Band 9-Circus	1.36−1.39	30
10	Band 10- Long Wavelength Infrared	10.30−11.30	100 resampled 30
11	Band 11- Long Wavelength Infrared	11.50−12.50	100 resampled 30

3.2.2.2. Sentinel-2A

Sentinel-2 is an Earth observation mission developed by European Space Agency (ESA) as part of the Copernicus Program to perform terrestrial observations in support of services such as forest monitoring, land cover changes detection, and natural disaster management. It consists of two identical satellites, Sentinel-2A and Sentinel-2B. Sentinel-2A satellite sensor was successfully launched on June 23, 2015, at 03.51:58 am CEST from a Vega launcher from the spaceport in Kourou, French Guiana. Sentinel-2A satellite is the first optical Earth observation satellite in the European Copernicus program and was developed and built under the industrial leadership of Airbus Defence and Space for the European Space Agency (ESA).

Copernicus is the new name of the European Commission's Earth Observation Program, previously known as GMES (Global Monitoring for Environment and Security). The mission is dedicated to the full and systematic coverage of land surface including major islands globally with the objective to provide cloud-free products typically every 15 to 30 days over Europe and Africa. The span of 13 spectral bands which is shown below (Table 3.2), from the visible and the near-infrared to the shortwave infrared at different spatial resolutions ranging from 10 to 60 m on the ground, takes global land monitoring. The four bands at 10 m resolution for basic land-cover classification; the six bands at 20 m resolution satisfy requirements for enhanced land-cover classification and three bands at 60 m are dedicated mainly to atmospheric corrections and cirrus-cloud screening (Sentinel-2, MSI, 2015).

Table 3.2: Spectral Band of Sentinel–2A data product with its Resolution

No	Sentinel-2 Bands	Central wavelength (μm)	Resolution (m)	Bandwidth (nm)
1	Band 1- coastal aerosol	0.443	60	20
2	Band 2-Blue	0.490	10	65
3	Band 3-Green	0.560	10	35
4	Band 4-Red	0.665	10	30
5	Band 5-Vegetation Red Edge	0.705	20	15
6	Band 6-Vegetation Red Edge	0.740	20	15
7	Band 7-Vegetation Red Edge	0.783	20	20
8	Band 8-NIR	0.842	10	115
9	Band 8A-Narrow NIR	0.865	20	20
10	Band 9-Water vapor	0.945	60	20
11	Band 10-SWIR circus	1.375	60	20
12	Band 11-SWIR	1.610	20	90
13	Band 12-SWIR	2.19	20	180

3.2.3. Secondary data

A secondary source of data that collected from a different organization, institution and individual experts were very important to generate the desired result of this research. The most widely used secondary data for this thesis work are geological survey data, metrological data, and central statistical data. Unpublished and published reports, journal articles, and internet sources were also used and the most important sources of information to understand the situation; analyze the results and write final reports.

3.3. Methodology

The methods used to assess the recent lava flows and land surface temperatures in Erta 'Ale volcanic range was discussed below using the previous scientific research work and the procedures they followed.

3.3.1. Preprocessing of satellite images

Image pre-processing is a process of or functions that involve those operations that are normally required prior to the main data analysis and extraction of information and are generally grouped as radiometric or geometric corrections. Radiometric corrections include correcting the data for sensor irregularities and unwanted sensor or atmospheric noise and converting the data so they accurately represent the reflected or emitted radiation measured by the sensor.

Geometric corrections include correcting for geometric distortions due to sensor-Earth geometry variations, and conversion of the data to real-world coordinates (e.g. latitude and longitude) on the Earth's surface. In order to normalize the data, that is, to minimize the effects of bias arising from atmospheric conditions, solar illumination and view angles, atmospheric calibration is required (Perez Hoyos, 2014). Therefore, Landsat 8 imageries both OLI and TIRS sensor data of the study area with Path and Row number (168, 050 and 051) year 2016−2017 was acquired from the USGS source by using their official website https:// earthexplorer. usgs. gov/. It was preprocessed by image analysis software i.e. Erdas imagine, Envi and ArcGIS to extract useful information from a multispectral band thermal infrared band of the satellite image.

Sentinel-2A satellite image also preprocessed using the Impact tool and eCognition software. It is a compilation of granules of fixed length (approximately 25 km across track and 23 km along track) and area (100 km^2 in UTM/WGS84 projection) available to user in Sentinel-Safe format (https://sentinel.esa.int/ web/sentinel/user-guides/ sentinel-2-msi/ data-formats). The impact tool software is used for extracting the zip data file to unzip and layer stack single Geo tiff images even by converting top of atmospheric reflectance and Projection. Using this software default bands selection [B2, B3, B4, B8, B12, B13] were layer stacked which are corresponding to [B, G, R, NIR, SWIR1, SWIR2] results in a product close to OLI bands (B2–B7) that enable us identify the features using their spectral values. Band 2, 3, 4 and 8 have a spatial resolution of 10 m and band 11 and 13 has 20 m resolution. During preprocessing the 20 m spatial resolution bands were resampled into 10 m. The framework of the study was schematically shown in (Fig 3.3).

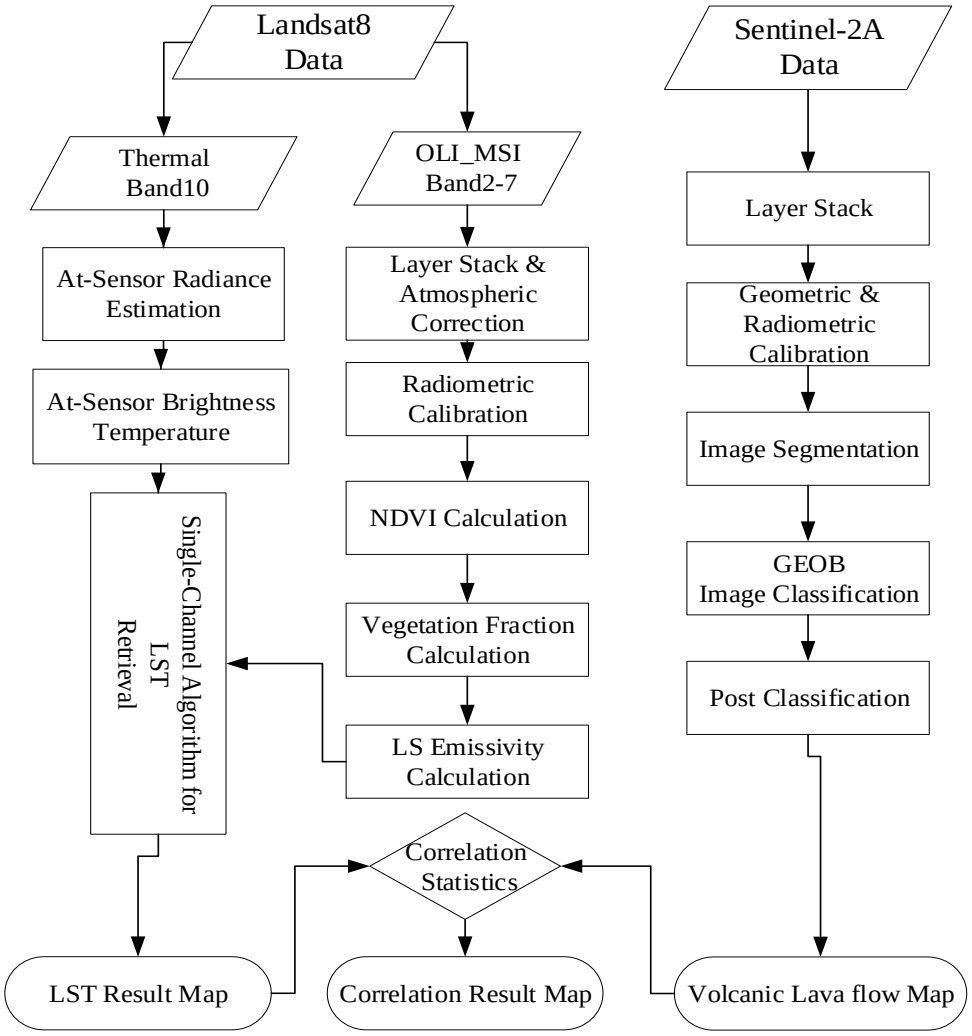

Figure 3.3: The general schematic flow chart of the methodology.

3.3.1.1. Conversion of S2-A MSI bit into byte reflectance

Radiometric resolution of S2 MSI instrument is 12 bit, saved using Unsigned Integer 16-bit data type (UInt16) (https:// sentinel. esa.int/ web /sentinel/user-guides/sentinel-2-msi /resolutions /radiometric) and output radiometric resolution were converted into Byte (8 bit) by using a linear transformation which is shown in equation 3.1.

$$Top\ of\ atmospheric\ reflectance\ byte\ =\ (DN * 0.0255) \quad (3.1)$$

Where,

- $DN =$ digital number of sentinel2 $-$ A satellite image
- $TOARefByte = top\ of\ atmospheric\ Reflectance\ Byte$

Raw sentinel–2A image DN values [0-4095] are converted to TOA reflectance [0,1] using the provided conversion factor (10000) and multiplied by 255 to obtain a byte TOA reflectance [0,255].

False color combination of band 13, band 4 and band 2 was used to identify the recent lava flow of this study in Erta'Ale volcanic range.

3.3.2. Methods of recent lava flow mapping

Volcanic activities mostly mapped using different methods in either direct measurement or remote sensing satellite information. Since lava flow is too hot to direct measure its temperature and map. It is advisable to use the remote sensing data to map such conditions and this new technology is very important to identify, to gather the characteristics of the hazard, to interpret and make an analysis without contact to the physical situation or phenomenon. There are many volcanic edifices in Erta 'Ale volcanic range i.e. in north Afar Alu-Dalafilla, Erta Ale, Alayta and further south, central grabens within a faulted and fissured terrain and a central vent area with a subsided edifice of Dubbahu, Manda Hararo, Ardoukoba and Kammourta (Barnie *et al*., 2015).

Mapping of geological structures is not the same as other natural and man-made resource mapping styles because the characteristics of different lithological units are not uniform and the formation of their structure is also related to different tectonic activities. Therefore, to map the recent lava flow field of Erta 'Ale volcanoes using multispectral sentinel–2A satellite image object-based image (OBI) classification techniques were selected because supervised and unsupervised classification is pixel-based that creates square pixels and each pixel has a class. But object-based image classification technique groups the pixels into representative shapes and sizes (Blaschke, 2010). The eCognition is a software product from the Munich Definiens company, which was founded by the Nobel laureate Gerd Binning which first developed in 1999 (Nussbaum and Menz, 2008). It used to preprocess and analysis the satellite image. Using this software recent lava flows was identified with relation to other geological features. Object-based image analysis classification is in principle suitable for use in all fields of remote sensing.

3.3.2.1. Geospatial object-based image classification

Geospatial object-based image analysis is a synonym for object-based image classification (Blaschke, 2010) utilizing Trimble's eCognition and other software programs have the ability to make smart class decisions based on spectral, shape, size and class relationships utilizing image

objects (image objects are groups of spectrally similar pixels). Object-based image analysis also has the ability to ingest and utilize temporal imagery and ancillary GIS data layers to make smarter class decisions, enhanced classifications and change detection outputs (Blaschke, 2010). It is a series of processing steps, in which the content analysis of the image (satellite or aerial) is applied to the recognition (segmentation), determination (classification), evaluation (accuracy and post-classification assessment) and analysis (e.g. changes, comparisons, mapping) of semantically clear spatial entities (homogeneous areas, structures, objects, phenomena) and not on the analysis of individual pixels (Tatjana *et al.*, 2011).

Within object-based analysis of remote sensing data homogeneous regions (segments) obtained from satellite images are used as basic entities. The object-based analysis consists of various procedures for obtaining segments and their characteristics (attributes), for analyzing these segments, sorting them into classes or objects (classification), verifying them and for error removal (post-classification) (Tatjana *et al*., 2011). There are three steps to classify multi-resolution satellite images in object-based image classification techniques i.e. (i) segmentation and computation of spectral, geometric, textural, conceptual and temporal attributes, (ii) object (semantic) classification and (iii) post-classification (verification, error elimination) and result validation (Tatjana *et al*., 2011).

The recent lava flows both from the Erta 'Ale lava lake and new fissure eruption was analyzed using the eCognition software. The preprocessed satellite image with band combination of 6, 4 and 2, was loaded into the software and multiresolution image segmentation process was carried out. This process used to segment the individual features in the form of spatial objects.

3.3.2.1.1. Multi-resolution image segmentation algorithms

Multiresolution segmentation produces homogenous image objects by grouping pixels. It generates objects with different scales in an image simultaneously. These objects are more meaningful because they represent features in the image.

Segmentation algorithms group individual pixels into segments according to the homogeneity within the segment (pixel value) Aplin and Smith, (2008), the ability to be separated from the neighboring elements (dissimilar), and the shape of homogeneity (Tatjana *et al.*, 2011).

The basic idea behind eCognition is that image objects and the relations between these objects contain important semantic image information (Nussbaum and Menz, 2008).

The image pixels from the image are grouped to form objects with the aid of a multiscale segmentation. The simultaneous formation of several levels of segmentation on different scales is possible and hierarchically linked to each other. Since image objects, image information and processes are present simultaneously on several scales and the relationship between these scales is known, important additional information can be obtained for interpretation purposes and real-world objects of different sizes can be classified (Nussbaum and Menz, 2008; Blaschke, 2010; Tatjana *et al.*, 2011).

The recent lava flows were segmented based on their homogeneous characteristics of pixel values. The band combinations are band 13, band 4, and band 2. Figure 3.4 shows the image segmentation process (b) and the formation of objects (c) on their homogeneity of pixel values. False color composite sentinel image (a) was processed using the eCognition software. New lava flow field was identified easily by relatively homogeneous and a semantically significant group of pixels (Blaschke, 2010) that link together form image objects.

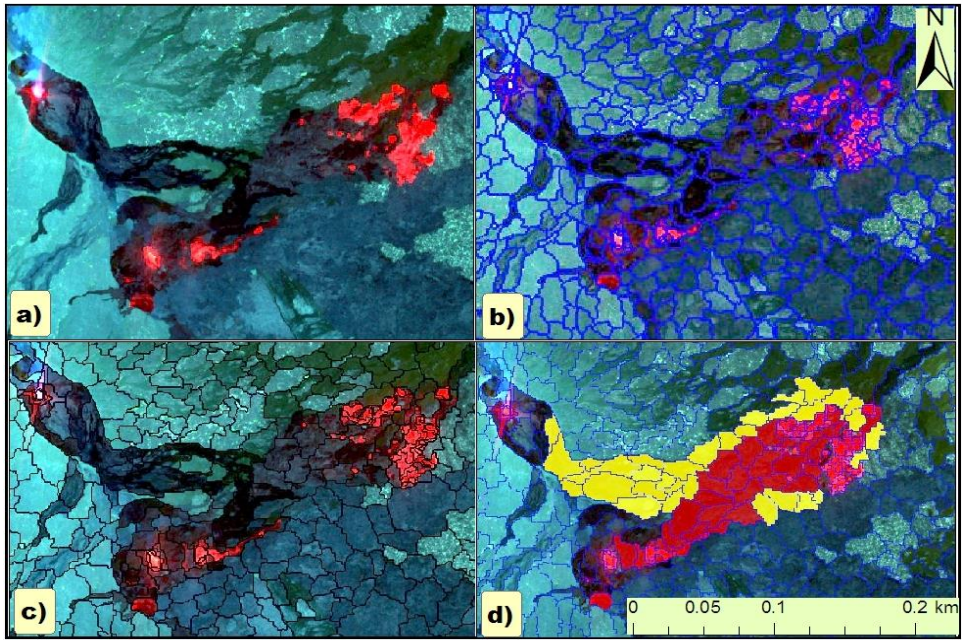

Figure 3.4: Image segmentation process, (a) FCC of sentinel-2A (b) image segmentation, (c) image object and classification view and (d) sampling stage for the classification.

3.3.2.1.2. Object-based image classification stage

The segmented objects were classified using the training object segment which is called semantic classification. The object (semantic) classification uses the segment characteristics to sort them into object classes and the individual segment characteristics (attributes) are compared, and

membership in a particular class is established using the eCognition software (Nussbaum and Menz, 2008; Tatjana *et al.,* 2011).

3.3.2.1.3. Post classification stage

Post classification procedures are predominantly manual; thus, they are time-consuming. They serve to eliminate the evident errors (wrong classifications) and generalize the results. Evident errors were eliminated by visual control, field inspection and/or comparison with the reference source (Nussbaum and Menz, 2008). In order to improve their visual quality and the content of the final result (the thematic map) the obtained object classes need to be generalized (Tatjana *et al.*, 2011). Sentinel2-A data were first preprocessed in Impact tool and then image object-based classification was carried out in eCognition software. Manually, the output was also edited in ArcGIS software to remove specific errors from the software techniques.

3.3.3. Parameters to calculate the land surface temperature

Land surface temperature is mainly generated from solar radiation which accounts for a throughout heating of the land surface and the Earth's interior heat which is responsible for a localized temperature increase (Qin *et al.,* 2011). It is related to surface energy and water balance, at local through global scales, with principal significance for a wide variety of applications, such as climate change, urban climate and the hydrological cycle (Rozenstein *et al*., 2014). Surface temperature retrieval from thermal infrared images is of considerable importance for many applications notably oceanography, global climate change, geology, hydrology and vegetation monitoring (Sobrino *et al.,* 1996). The most important parameters to calculate LST using SC algorithm in this study were an estimation of land surface emissivity and at–sensor brightness temperature from radiometric and geometrically calibrated satellite image.

3.3.3.1. Sensor spectral radiance and reflectance

According to Landsat-8 (2016) handbook the sensor spectral radiance and reflectance was calculated using the standard Landsat-8 data products provided by the USGS EROS center consist of quantized and calibrated scaled (DN) digital numbers.

It represents multispectral image data acquired by both the operational land imager (OLI) and thermal infrared sensor (TIRs). These multispectral image products are delivered in 16-bit unsigned integer formats. This product was also rescaled to the top of atmosphere (TOA) reflectance and/or radiance.

Both OLI and TIRS images were processed in units of absolute radiance using Erdas imagine software and each digital number value of an image was converted to spectral radiance using the radiance scaling factors. The model equation used to convert image digital number value into its sensor spectral radiance was given by Landsat user handbook (http://Landsat handbook.gsfc.nasa.gov/). This Landsat sensors OLI and TIRs band data was converted to top of atmospheric spectral radiance using the radiance rescaling factors provided in Landsat 8 metadata file which is shown in equation 3.2:

$$L\lambda = (ML)(Qcal) + AL \quad (3.2)$$

Where,

- $L\lambda$ = TOA spectral radiance (Watts / (m^2 * srad * μm))
- ML = Radiance multi band 10, from the metadata file.
- AL = Radiance add band 10, from the metadata file.
- $Qcal$ = Quantized and calibrated standard product pixel values of image (DN)

Radiance is the most important factor for brightness temperature retrieval and it was calculated from the thermal infrared sensor of band 10 image DN value using the proposed equation. Similar to the conversion to radiance, the 16-bit integer values in the level1 product were converted to TOA reflectance. Top of atmospheric reflectance with a correction for the sun angle along the sensor was also calculated using equation 3.3:

$$\rho\lambda = \rho\lambda' / sin(\theta SE = \rho\lambda' / cos(\theta SZ) \quad (3.3)$$

Where,

θ_{SZ} = Local solar zenith angle; θSZ = 90° - θSE

ρλ = Top of atmospheric planetary reflectance

θ_{SE} = Local sun elevation angle.

The scene center sun elevation angle in degrees is provided in Landsat 8 metadata and instead of using the scene center solar angle for more accurate reflectance calculations, per pixel solar angles should be used. So, sun angle correction of the Landsat 8 image was calculated using sun angle elevation by subtracting from 90^0 i.e. θSZ = 90° - θSE.

3.3.3.2. At-sensor atmospheric brightness temperature

Thermal infrared sensor data were converted from spectral radiance to brightness temperature, which is the effective temperature viewed by the satellite under an assumption of unity emissivity. The conversion formula is shown in equation 3.4:

$$T = K2/(\ln\frac{k1}{L\lambda} + 1) \quad (3.4)$$

Where,

- T = TOA Brightness Temperature, in Kelvin.
- Lλ = Spectral radiance (Watts/(m^2 * srad * μm))
- K1 = Thermal conversion constant for the band 10 from the metadata file.
- K2 = Thermal conversion constant for the band 10 from the metadata file.

The brightness temperature is not a temperature as ordinarily understood. It characterizes radiation and depending on the mechanism of radiation can differ considerably from the physical temperature of a radiating body (though it is theoretically possible to construct a device which will heat up by a source of radiation with some brightness temperature to the actual temperature equal to brightness temperature). At-sensor brightness temperature is the temperature of a black body in thermal equilibrium with its surroundings would have to be to duplicate the observed intensity of a grey body object at a frequency. This concept is extensively used in radio astronomy and planetary science. The brightness temperature of the study area from TIRS sensor is shown in (Fig 3.5 to 3.7).

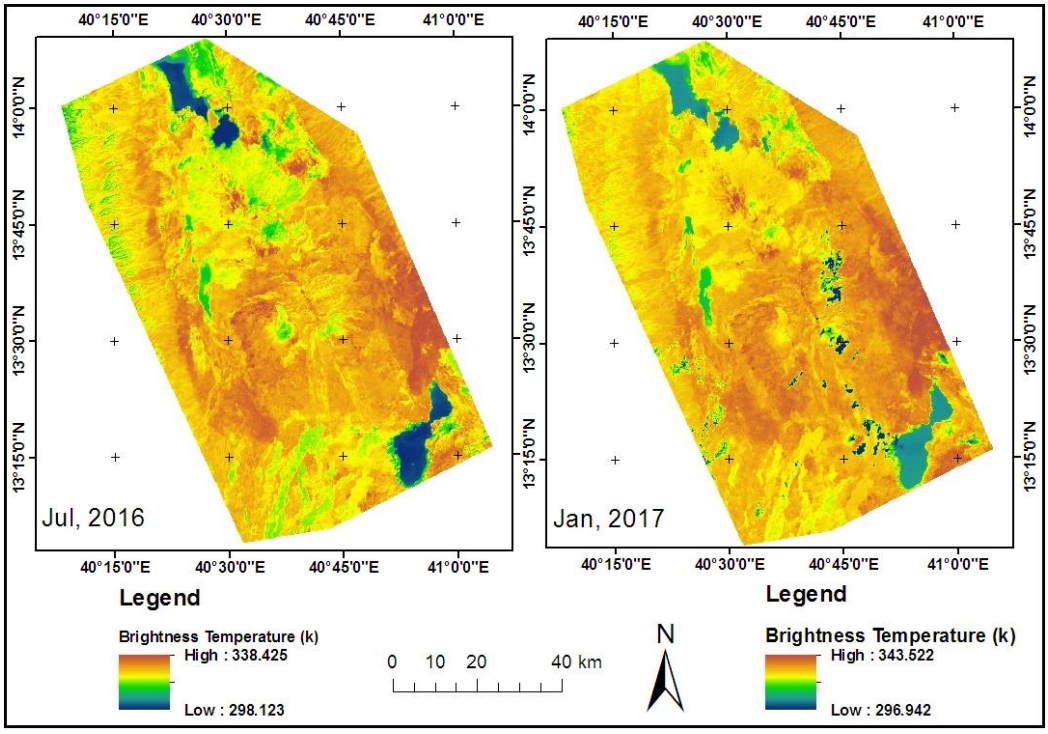

Figure 3.5: Sensor brightness temperature map (July 2016 and January 2017).

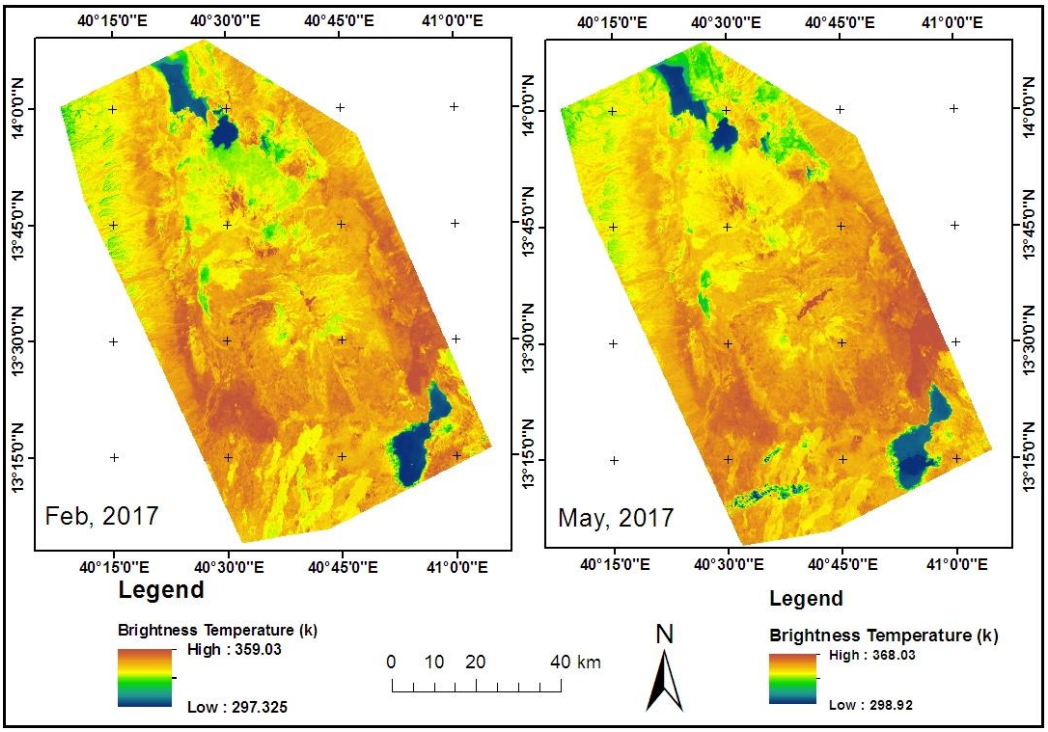

Figure 3.6: Sensor brightness temperature map (February and May 2017)

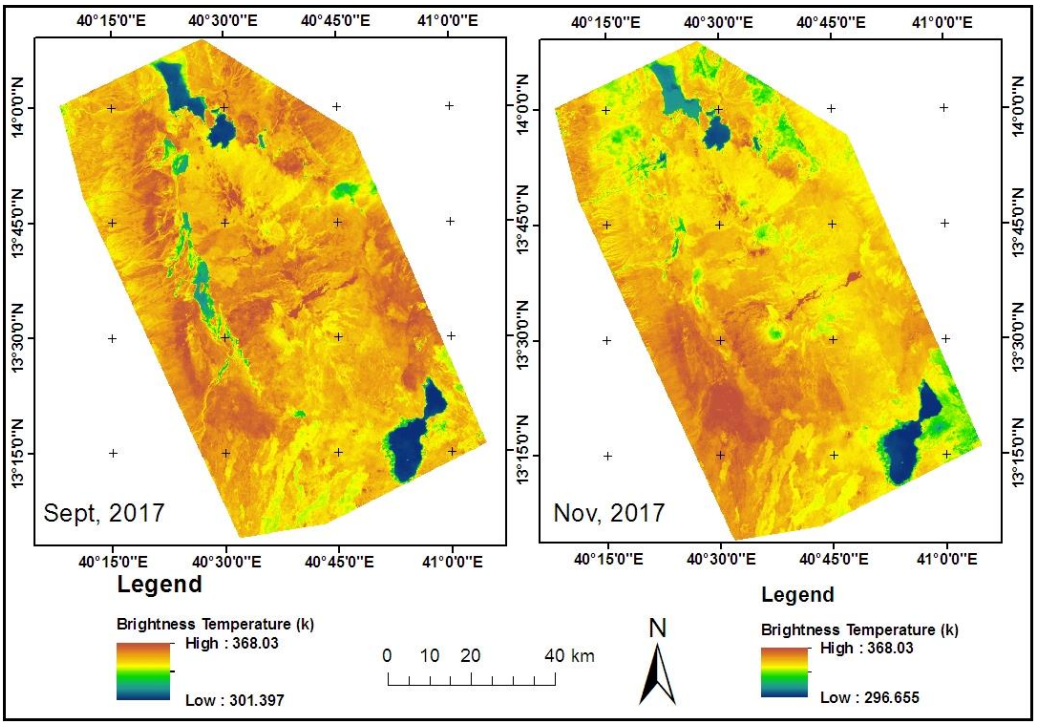

Figure 3.7: Sensor brightness temperature map in September and November 2017.

3.3.3.3. Vegetation fraction from NDVI

Normalized difference vegetation index is a common and widely used index. It is an important vegetation index, widely applied in research on global environmental and climatic change (Gandhi *et al.*, 2015). Radiometrically calibrated Landsat 8 OLI bands were used to calculate the NDVI of the study area. NDVI also used to calculate the Vegetation fraction or Proportion of vegetation for land surface emissivity value. Normalized Difference Vegetation Index (NDVI) quantifies vegetation by measuring the difference between near-infrared (which vegetation strongly reflects) and red light (which vegetation absorbs). Normalized Difference Vegetation Index (NDVI) uses the ratio of the Reflectance of NIR and the Reflectance of red channels using the formula equation:

$$NDVI = \frac{Rnir - Rred}{Rnir + Rred} \quad (3.5)$$

Where,

- NDVI =Normalized difference vegetation index
- Rnir =The reflectance of near-infrared band of Landsat-8 satellite image i.e. band 5
- Rred = The reflectance of red band of Landsat-8 satellite image i.e. band 4

There are a number of image analysis software that used to calculate the NDVI value using the reflected near-infrared and red band of land sat products. Some of this image analysis software are ENVI, Erdas Imagine, Arc GIS and Trimble's eCognition. The behavior of data preprocessing is different for each software resulting different output of NDVI value. The result was calculated using the Arc GIS image analysis Function toolbox. The raw data were layer stacked using Erdas software to calibrate both radiometric and geometric distortions. Band 5 and 4 were extracted using extract band function tool from ArcGIS. Overall image was calculated its NDVI value and its maximum and minimum value were in between -1 and +1.

Vegetation fraction cover is the percentage of the vertical projection of vegetation canopy (including leaves, stems, and branches) in per unit area (Zhang *et al.*, 2006; Qin *et al*., 2011). Vegetation fraction (equation 3.6) can also be derived from NDVI using the formula:

$$PV = \left(\frac{NDVI - NDVIs}{NDVIv - NDVs}\right)^2 \quad (3.6)$$

Where,

- PV = Vegetation fraction (proportion)
- NDVI = Normalized difference vegetation index
- NDVIv = Normalized difference vegetation index of vegetation
- NDVIs = Normalized difference vegetation index of soil

Using this formula, the proportion of vegetation was generated from the NDVI value using remote sensing methods (Tian *et al.*, 2004) and the result was used to calculate the land surface emissivity of the study area. The fraction of vegetation cover (FVC) is an important variable for many land surface biophysical and biogeochemical models and serves as a useful measure of land cover change. Estimating proportion of vegetation with remote sensing technique has become the primary means due to rapid spatial and temporal changes of vegetation cover (Zhang *et al.*, 2006).

3.3.3.4. Estimation of land surface emissivity

Emissivity is defined as the ratio of the energy radiated from a material's surface to that radiated from a blackbody (a perfect emitter) at the same temperature and wavelength and under the same viewing conditions. It is a dimensionless number between 0 (for a perfect reflector) and 1 (for a perfect emitter). The emissivity of the surface of a material is its effectiveness in emitting energy as thermal radiation.

Thermal radiation is electromagnetic radiation and it may include both visible radiation (light) and infrared radiation, which is not visible to human eyes. According to Li *et al.* (2013) land surface emissivity (LSE), as an intrinsic property of natural materials. It is often regarded as an indicator of material composition, especially for the silicate minerals, although it varies with viewing angle and surface roughness (Sobrino *et al*., 2002, 2004). It is very important for soil development and erosion, estimation of sparse vegetation cover and bedrock mapping and exploration (Li *et al*., 2013).

The emissivity of a surface depends not only on the material but also on the nature of the surface. For example, a clean and polished metal surface will have a low emissivity, whereas a roughened and oxidized metal surface will have a high emissivity (Mallick *et al.,* 2012; Li *et al*., 2013). The emissivity also depends on the temperature of the surface as well as wavelength and angle. Knowledge of surface emissivity is important both for accurate non-contact temperature measurement and for heat transfer calculations. (http:// www.npl.co.uk /reference /faqs /what-is-emissivity -and- why- is- it- important- (faq- thermal).

Emissivity is a key variable in LST retrieval. It is calculated using pixel level vegetation fraction from Normal Differential Vegetation Index (NDVI) and this approach proposed by (Sobrino *et al.,* 2002) is applied to calculate emissivity to calculate land surface temperature. Therefore, the emissivity of the land surface in the study area was calculated from Landsat8 OLI imageries that is one of the parameters for LST calculation. Land surface emissivity (E) is a proportionality factor that scales blackbody radiance (Planck's law) to predict emitted radiance, and it is the efficiency of transmitting thermal energy across the surface into the atmosphere. In this sense, emissivity must be known in order to estimate land-surface temperature accurately from radiance measurements. Knowledge of the emissivity spectrum is also useful for terrestrial and planetary geologic studies to map surface materials based on differences in wavelength-dependent spectral features (Sobrino *et al.,* 2004). NDVI Threshold method which is developed by (Sobrino *et al.,* 2004) were used to estimate land surface emissivity. The method proposed obtains the emissivity values from the NDVI considering different cases:

(i) NDVI < 0.2

In this case, the pixel is considered as bare soil (Pv = 0) and the soil emissivity (Es) is assumed as a mean value of 0.97 (Sobrino *et al.,* 2004, 2008; Qin *et al.,* 2011).

(ii) NDVI>0.65

Pixels with NDVI values higher than 0.65 are considered as fully vegetated, and then a constant value for the emissivity is assumed, typically of 0.99 (Sobrino *et al.*, 2004, 2008; Qin *et al.*, 2011).

(iii) 0.2<NDVI>0.65

In this case, the pixel is composed by a mixture of bare soil and vegetation. The emissivity for a mixture of bare soil and vegetation pixel is calculated using the following equation (Sobrino *et al.*, 2004; Qin *et al.*, 2011):

$$LSE = mPV + n \quad (3.7)$$

With, $m = E_v - E_s - (1 - E_s) * F * E_v$,

$$n = E_s + (1 - E_s) * F * E_v$$

where,

E_s = emissivity of soil

E_v = emissivity of vegetation.

F is a shape factor (Sobrino *et al.*, 1990; Qin *et al.*, 2011) whose mean value, assuming different geometrical distributions, is 0.55 and the result of emissivity value is shown in (Fig 3.8 to 3.10).

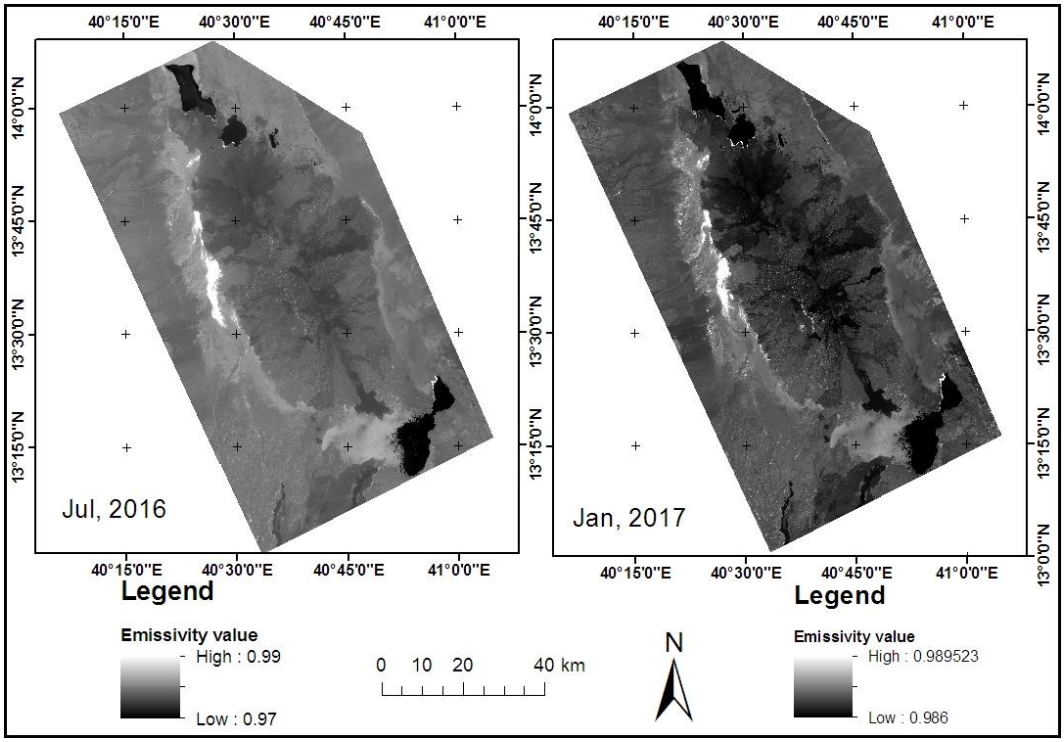

Figure 3.8: Land surface emissivity map (July 2016 and January 2017).

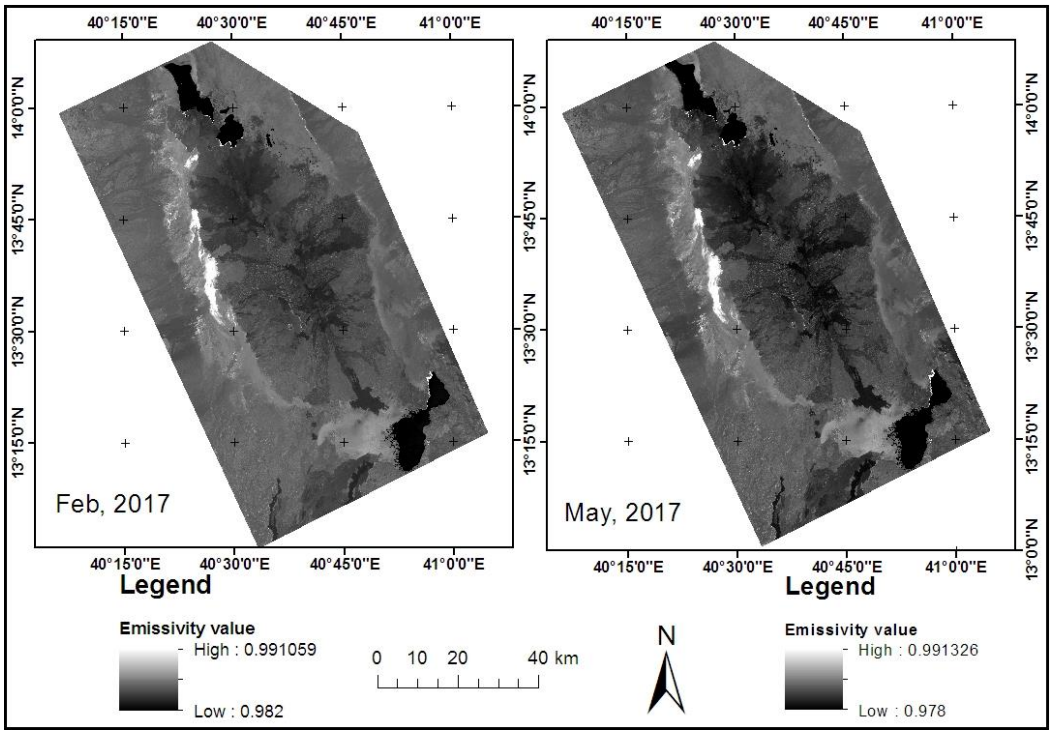

Figure 3.9: Land surface emissivity map (February and May 2017).

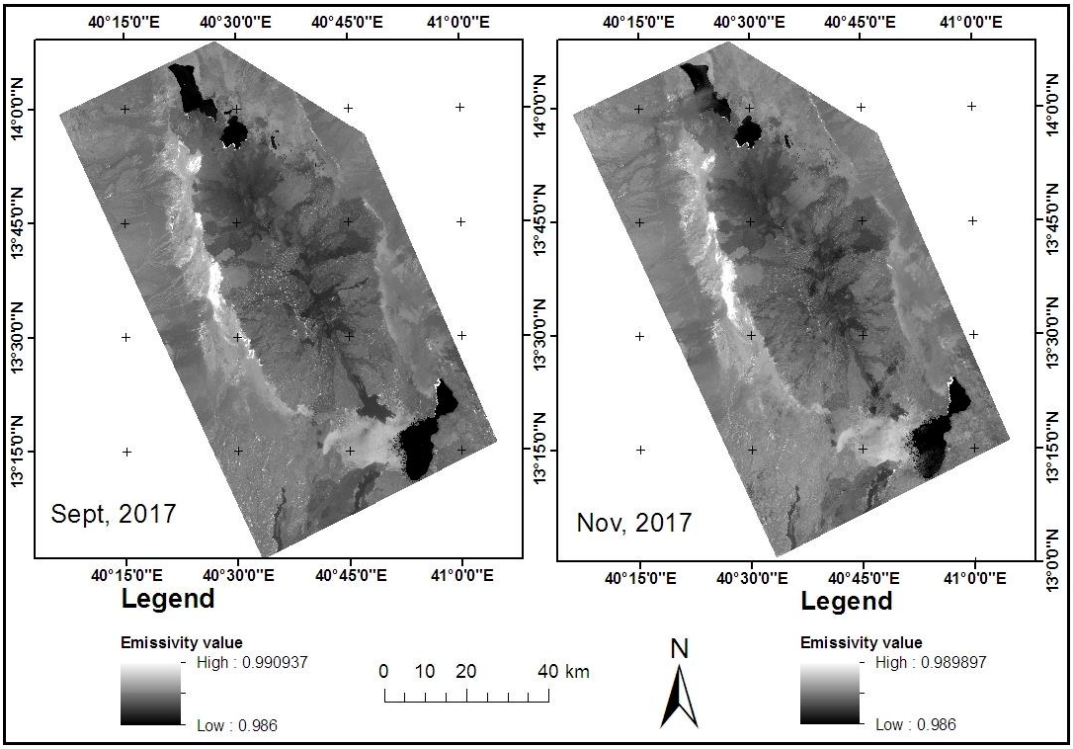

Figure 3.10: Land surface emissivity map (June and September 2017).

3.3.3.5. Single channel algorithm for LST retrieval

To estimate LST a Single-Channel (SC) Algorithm which was proposed by (Artis and Carnahan, 1982) was adopted (used) shown in equation 3.8. The reason for using single channel algorithm to estimate LST was it requires the least number of parameters to calculate temperature (Qin *et al.*, 2011) compared to other LST retrieval algorithms. In addition to this, a thermal band of Landsat-8 has two thermal bands (band10 and band11) that used to retrieve the temperature.

According to Landsat-8 user handbook of (Landsat-8, 2016), band 10 is more accurate than band11 to retrieve land surface temperature. Therefore, LST were retrieved from thermal remote sensor band 10 of Landsat satellite image using single channel method (Artis and Carnahan, 1982; Jimenez-Munoz and Sobrino, 2004; Jimenez-Munoz *et al.*, 2014) because band 10 can give more information and more accurate than band 11 (Xiaolei *et al.*, 2014).

$$LST = \frac{Tsensor}{1+\left(\lambda * \frac{Tsensor}{P}\right)\ln(E)} \quad (3.8)$$

λ = the wavelength of emitted radiance (the average wavelengths for band10 λ = 10.8 µm was used), p = h× c/j in m K, where h is Planck's constant (6.626×10^{-34} J s), c is the velocity of light (2.998×10^{8} m/s), and j is Boltzmann constant (1.38×10^{-23} J/K). T-sensor is at-sensor brightness temperature in K and *E* is the land surface emissivity.

CHAPTER FOUR

RESULTS

4.1 Lava flow map

Volcanic activities in eastern part of Ethiopia is related to the East African Rift system and Erta 'Ale lava lake is one of the active basaltic shield volcanoes. The eruption characteristics of this volcano during 2016−2017 were described and the results are shown in figures.

4.1.1 A volcanic eruption in 2016

From the preprocessed image the result shows that there was no long-distance lava flow of volcanic eruption in the study area from the year of 2016. In mid-January, 2016 at the southern crater the Erta 'Ale volcano lava lake overflowed on its rim was witnessed and captured as shown in (Fig 4.1). This lava overflowing on its rim lasted for a short period and the lake level dropped 5−7 m in February 2016 (Global Volcanism Program, 2017). The current assessment of lava flow using the geospatial technology (tools) indicate in mid-January and November 2016 there was an overflow of the lava lake at the southern crater of the rim. Except these two months, the Erta 'Ale lava lake in the year of 2016 remains active with fluctuating the lake level at the southern crater of the rim.

Figure 4.1: January 2016 Erta 'Ale lava flow on its rim (Source: Global Volcanism Program, 2017. Photos by Hans en Jooske (https://www.vocano adventures.com/ tours/ Danakil /nov2016/ impressions.html).

Except lava level rising on its rim and falling no volcanic fissure eruption and lava flows out of the surface from Erta 'Ale lava lake and around the range of the study which was shown in (Fig 4.2). The base map was sentinel–2A satellite image with the band combination of 13, 4, and 2. The contour map was generated from SRTM (DEM) in 50 m interval and it indicates the direction of lava flow downslope of the area.

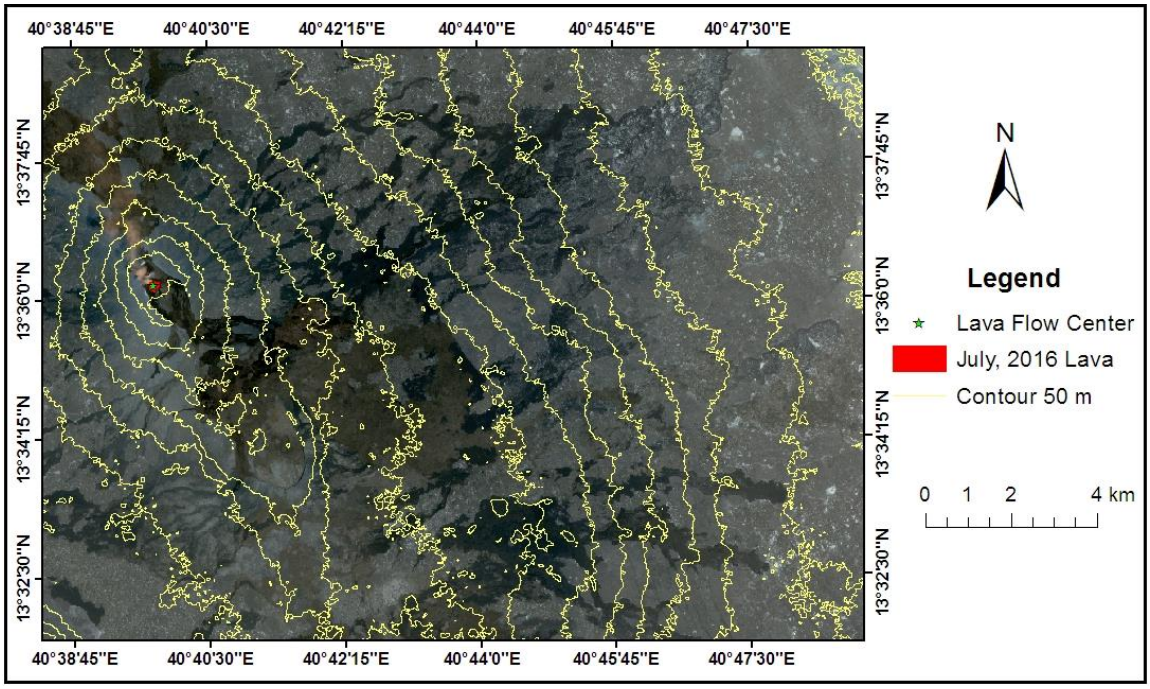

Figure 4.2: Lava lake of Erta 'Ale volcano map (July 2016).

4.1.2 Lava eruptions in 2017

The general assessment result of volcanic lava flows in the year of 2017 indicates that the Erta 'Ale lava lake at the southern crater on January 19, 2017, was overflowed in the summit caldera. There was no new fissure eruption and volcanic activity in the range rather from Erta 'Ale lava lake at the southern crater. A close analysis of the satellite image (19th January 2017) shows that lava flows were not cover the large area and move long distance. It flows from the southern crater of lava lake rim and this lava flow was not continued in February month. Sentinel-2A satellite image (19th January 2017) result indicates that both at the northern and southern crater of Erta 'Ale caldera lava lake was active. This active lava lake from the southern crater overflowed out of the surface 17th January 2017 as the assessment result indicates.

Though the current assessment result shows that lava overflow to south-east and eastern part of the caldera was seen in 19th January 2017 which is shown in (Fig 4.3). The activity of lava lake flow declined and cooled after 21st January 2017 and ceased by the end of January 2017.

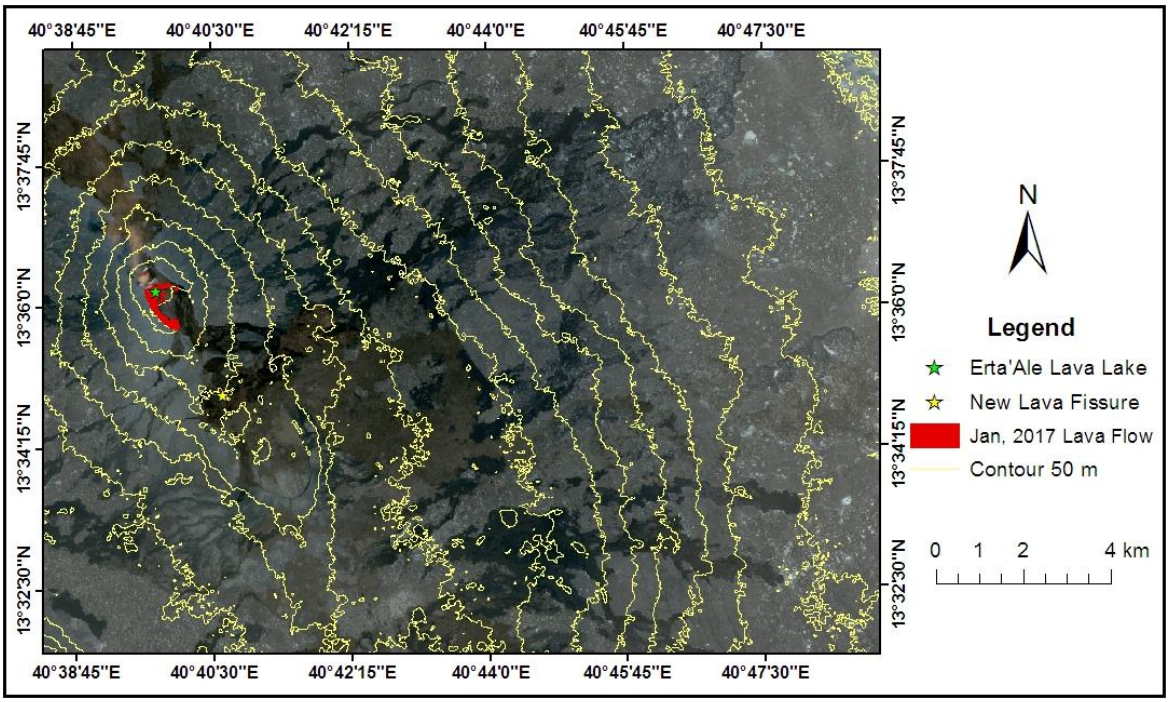

Figure 4.3: Erta 'Ale lava flow map (January 19, 2017).

Recent lava from the volcanic range of Erta 'Ale caldera starts to overflow on the surface from January 2017. This lava flow starts from the southern crater of the Erta 'Ale volcano lava lake. For the first three weeks, there was no new fissure eruption and lava flow through the range which is shown in (Fig 4.4a). In between January 19−29, 2017, lava fountaining was observed along the southern portion of the caldera with new fissure eruption and fed lava flows at eastern flank. The result is presented in (Fig 4.4b). The report of Global Volcanism Program (2017) indicates new fissure eruption start on January 20−21 2017. During the course of the eruption, dramatic lava fountaining and phreatic activity produced ash plumes within few days by covering a large area of lava flow field. Before and during the opening of the flank fissures, large-scale collapses occurred in the summit area, involving both the northern and southern (lava lake containing) pit craters, and generating significant ash plumes that were visible from base camp. The eruptive fissures generated three distinct lava fields into the northeast, to the west, and to the south-southeast directions.

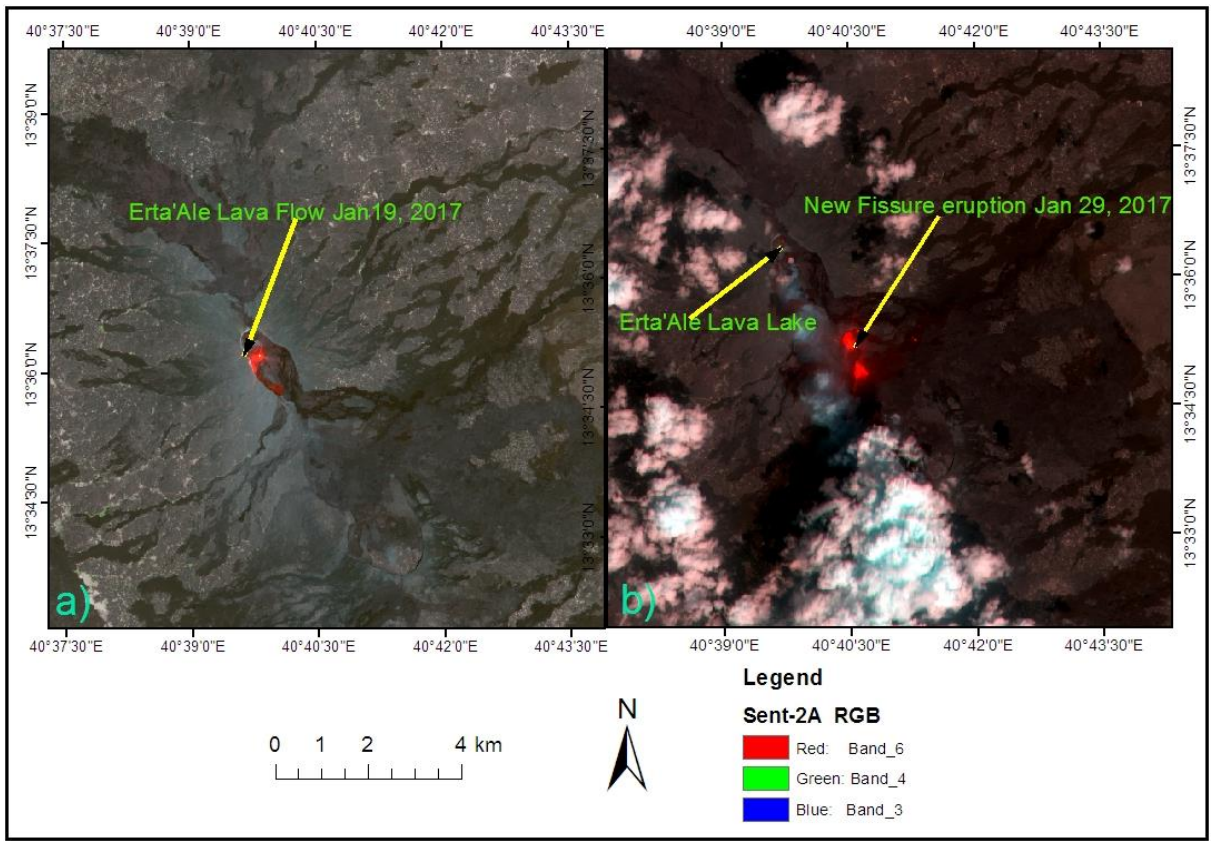

Figure 4.4: Erta 'Ale lava flow (January 19, 2017), (a) and New volcanic fissure eruptions and lava flow (January 29, 2017) (b).

New fissure eruption along the NW–SE flank trending axis of the shield volcano within a distance of 4.5 km was formed from January 19, 2017−January 29, 2017. Therefore, around the end of January 2017, Erta 'Ale volcanic lava which overflows out of the surface was cooled. Generally, there was no lava flows from persistent lava lake after new fissure eruption overflows. The new fissure eruption of lava was overflow in a different direction and covers a large area with compare to the Erta 'Ale lava flow on January 19, 2017, from persistent lava lake. The result is presented in (Fig 4.5). The map describes new fissure eruption and lava flows to a different direction. The east–northward lava flow covers a large area with compare to the south and northward flows. The new fissure eruption at the end of January 2017 indicates that the flow activity and the speed of lava flows were so fast that it covers a large area for a few days.

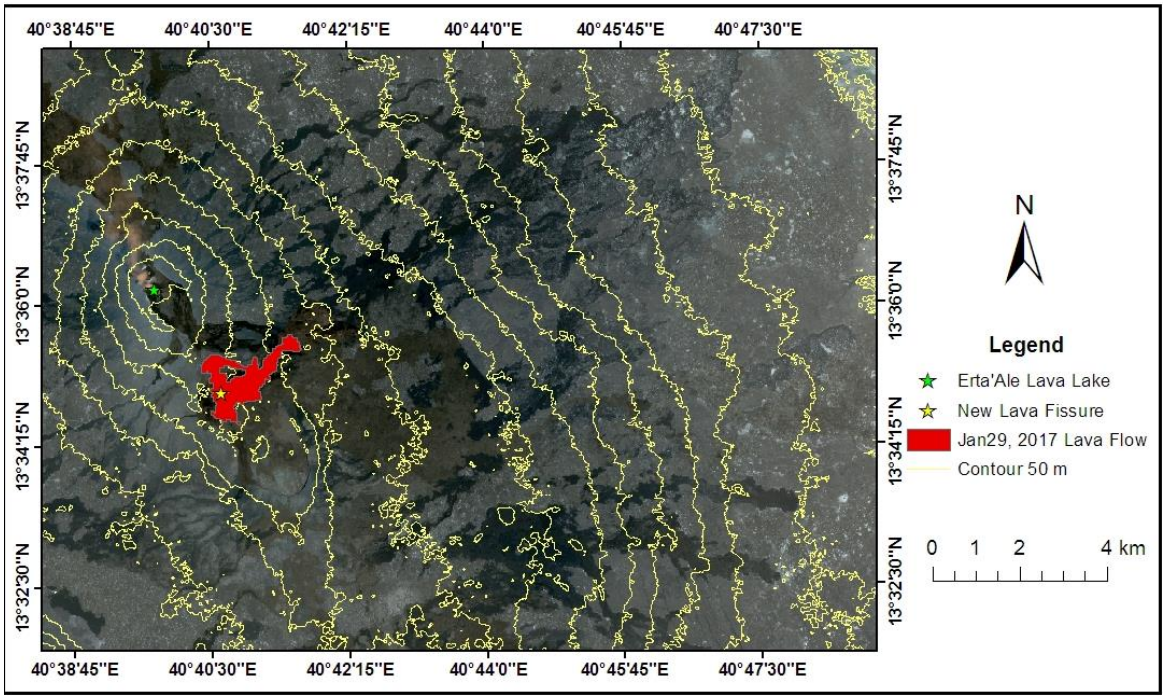

Figure 4.5: New fissures eruption and lava flow map (January 29, 2017).

The new fissure eruption on February 2017 indicates that lava fountain and flow was increased. When lava flows became visible and covering a large area in the southern part of the caldera and eastern direction from the new fissure eruption. New fissure eruption lava flows in north−east, western and southern part in February 2017 was shown in (Fig 4.6). The February volcanic lava flows from the newly opened fissure eruption center was different from the other flows because it includes all directional flow i.e. north, east−north, south and western part of the lava center. The northward and westward lava flow is smaller than southward and east−northward lava flow because it covers a large area during the lava flow. The February lava flows from new fissures eruption indicates that the length of lava flows in south and east direction increase from the January 29 flow. The result of lava which flows from the new opening center to the southern part becomes declined and cooled and it was not continued on March 2017.

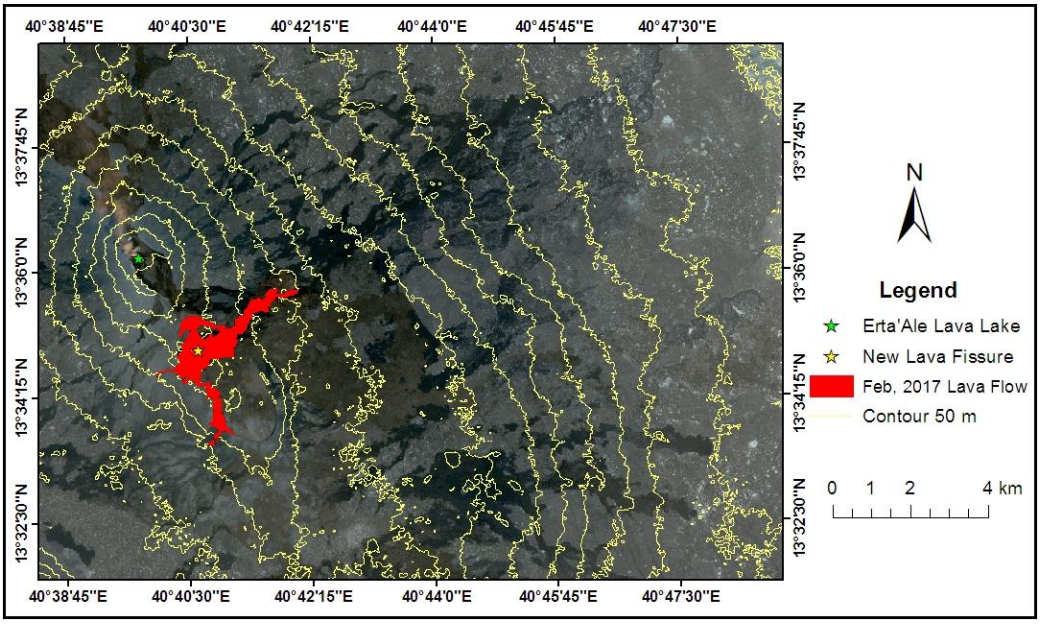

Figure 4.6: New lava flow map (February 2017).

The recent lava flows from the new fissure eruption at the southern flank of persistent lava lake on March 2017 was increased by an area coverage and distance of flooding. The result was shown in (Fig 4.7). The old lava lake, north and south pit of crater did not show any lava flows in this month. The new volcanic fissure eruption which was formed in the southern part of persistent lava lake (caldera) were overflowing to the surface. This flow also continued until April 2017 in the east–northward from the vent.

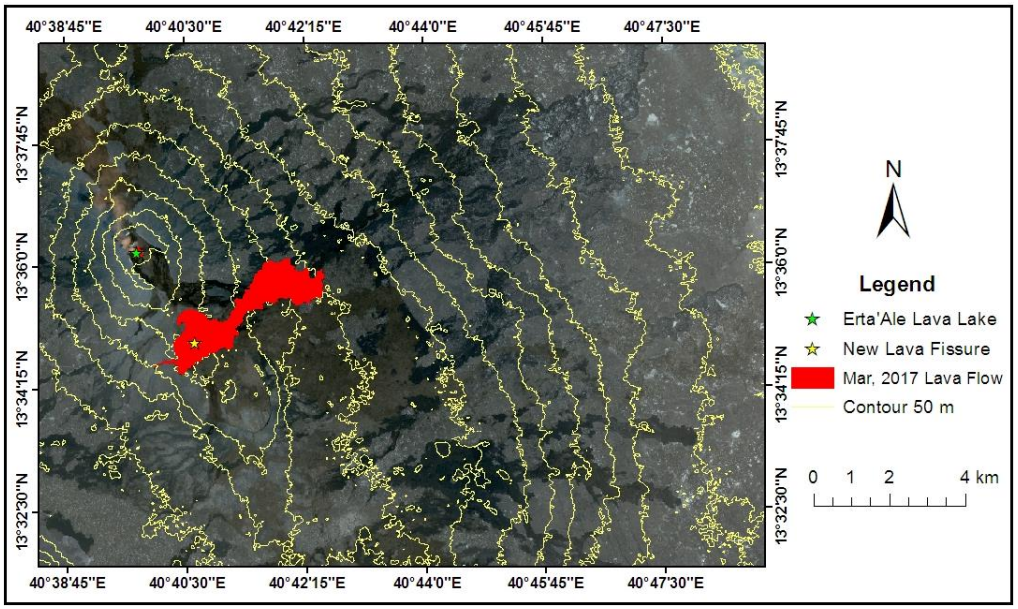

Figure 4.7: Lava flow map (March 2017).

The lava flow in east–northward of the caldera was continued on April 2017. The northern part of the new fissure eruption lava flowed become cooled and no flow on March which is shown in (Fig 4.8). The result also shows that whatever the lava flow in two consecutive months is the same in north−east direction but the area of lava flow cover in April is bigger than that of March.

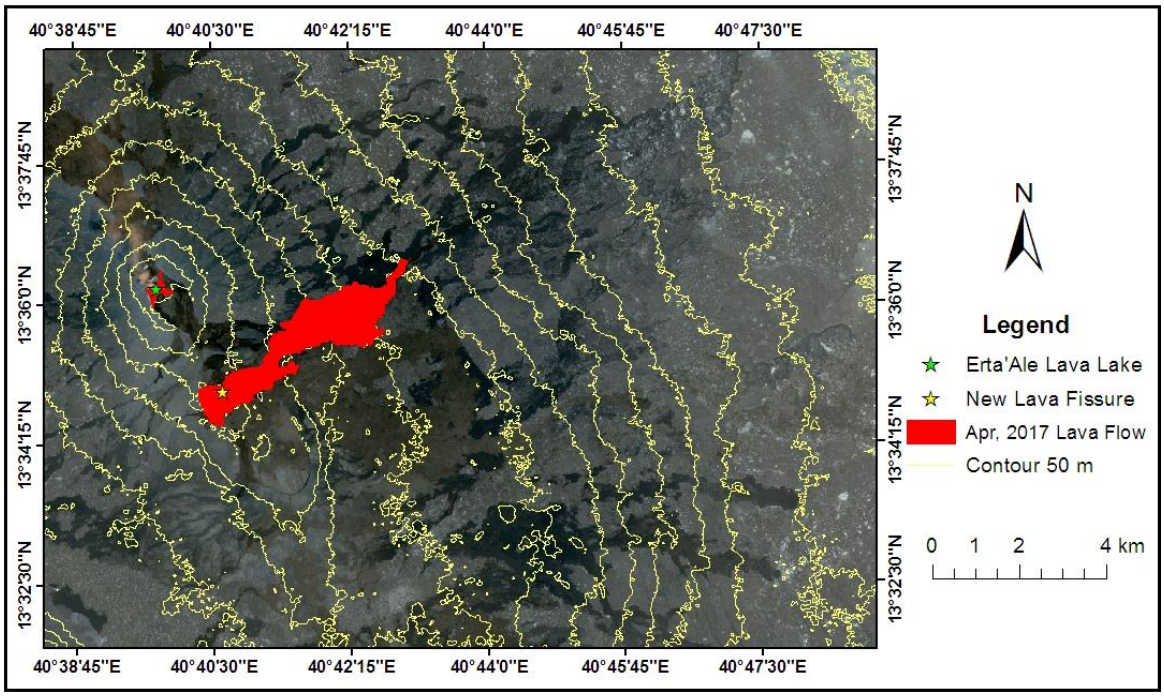

Figure 4.8: Lava flow map (April 2017).

At the same direction of the lava flow on April, the lava flow in May was increased. The lava was also flooded in the western part of the new fissure eruption. This lava flow covers a large area from the April lava flows. The result is presented in (Fig 4.9). Lava flows from the new fissure to the west and east direction were increased with compare to the April lava flow. The old lava center (Erta 'Ale volcanic lava lake) both northern and southern crater has no lava overflow on May 2017. The lava lake rises and falls at the rim.

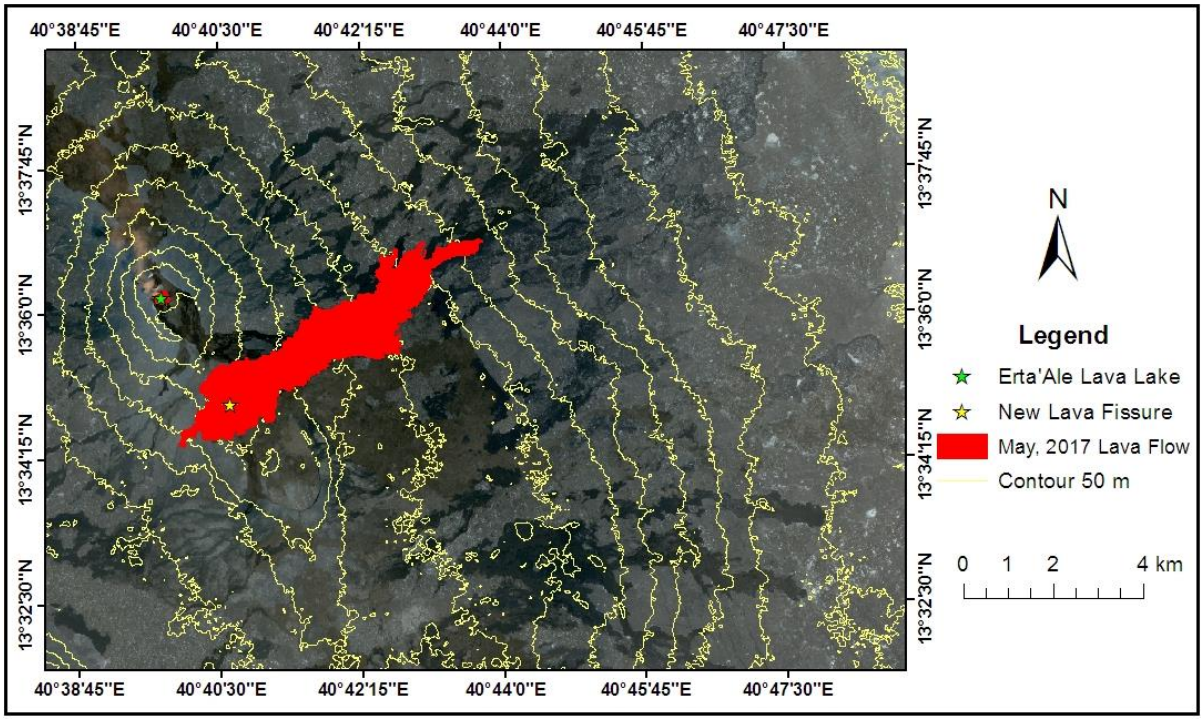

Figure 4.9: Lava flow map (May 2017).

Volcanic activity at the fissure vent increased during subsequent months, and by June 2017 a substantial new lava field that contained at least one new lava lake and flows long distance covered the area. The June lava flows were not different from the May lava flows at the direction of north−eastward rather the lava flow distance increased. The old lava lake at the southern pit crater overflows at the rim flank in this month. The northern crater has no volcanic activities shown. The assessment result indicates the west–south direction of new fissure eruption fed lava flow in two directions. After flooding a few distances, the lava flows become near to contact each other in June 2017. The result is shown in (Fig 4.10).

The recent lava flow assessment result (June–September 2017) shows an increased trend of lava flow area covering in the same flow direction. The northeast lava flow on September 2017 smoothly changes its direction to south-east with a single channel flow. This lava was overflooded for a long distance along the south-eastward of the Erta 'Ale volcanic range. The west–southward of two directional lava flows overcome together and made a large lava flow field at the western part of new fissure eruption. The result of September lava flow map is shown in (Fig 4.11).

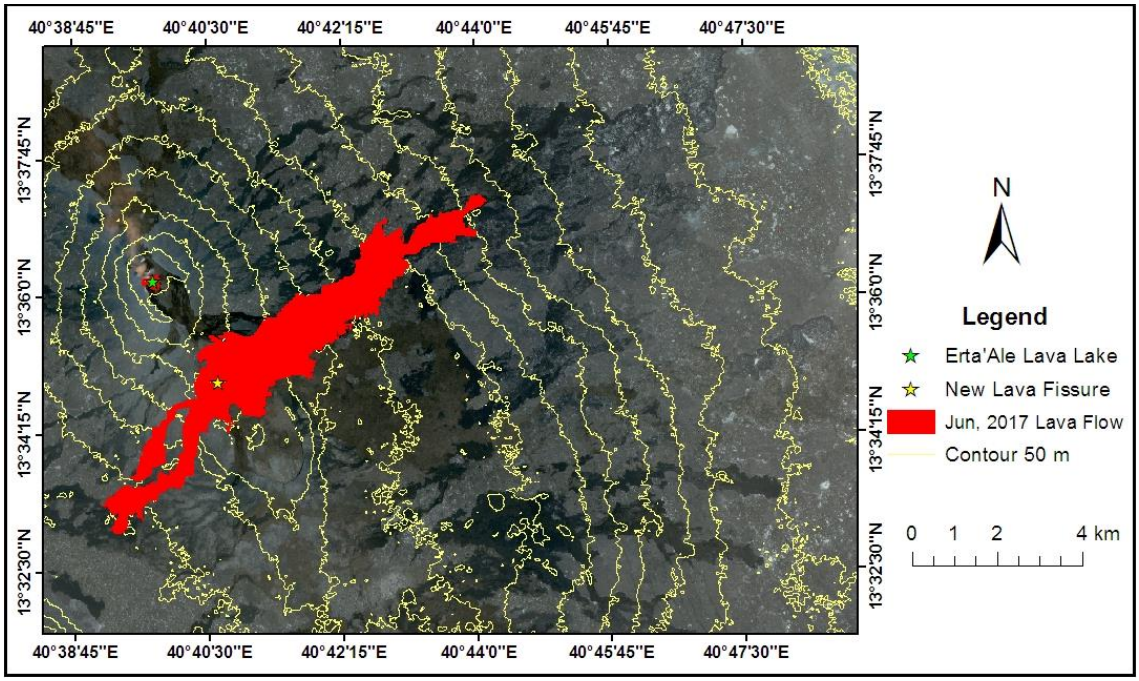

Figure 4.10: Lava Flow map (June 2017).

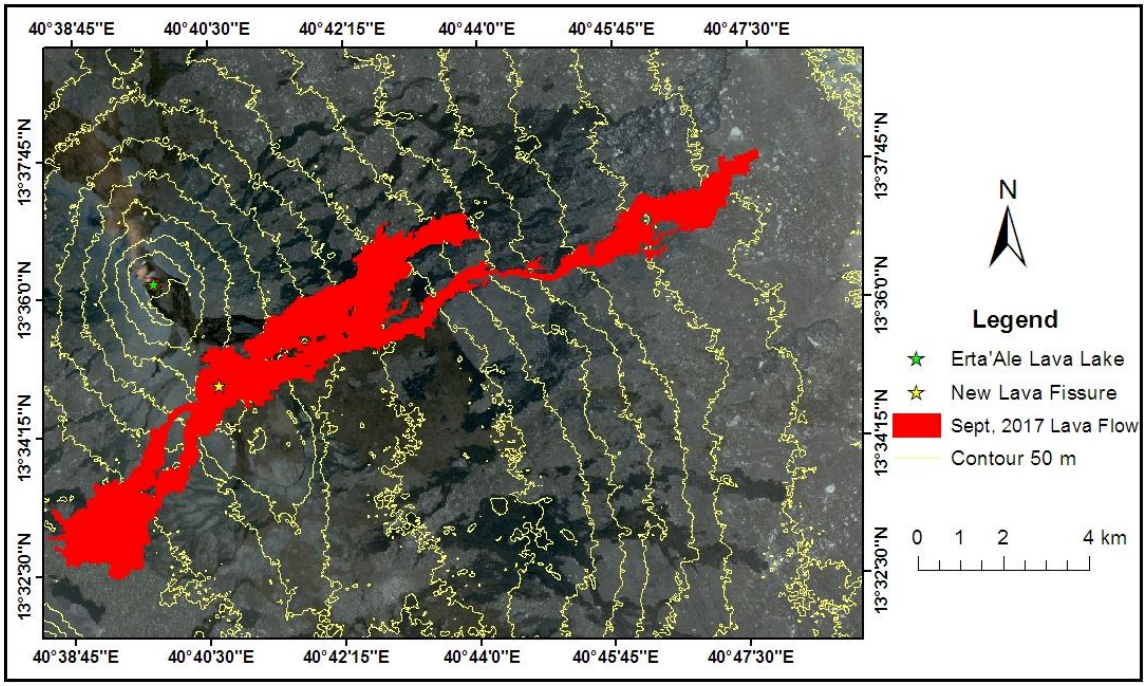

Figure 4.11: Lava flow map (September 2017).

The November lava flow covers a large area with compare to other flows and the result is mapped and presented in (Fig 4.12). The process of successive lava flows filling the crater and overflowing downslope into east and west direction of the new fissures. There was also lava overflown at the southern crater pit of the summit from the old lava lake.

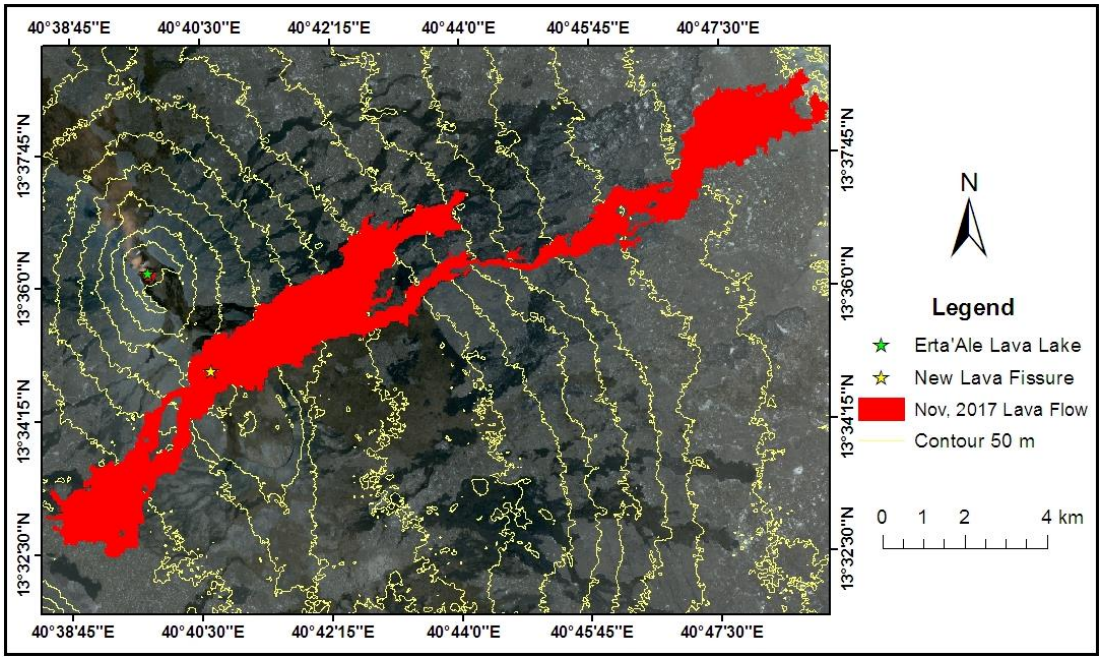

Figure 4.12: Lava flow map (November 2017).

Lava flows in December is presented in (Fig 4.13) and the resulting map shows that the lava flow was reduced in size with compare to the November lava flow but records the longest distance flown in an eastern direction. The Erta 'Ale lava lake at the southern pit was active in the summit of caldera on this month.

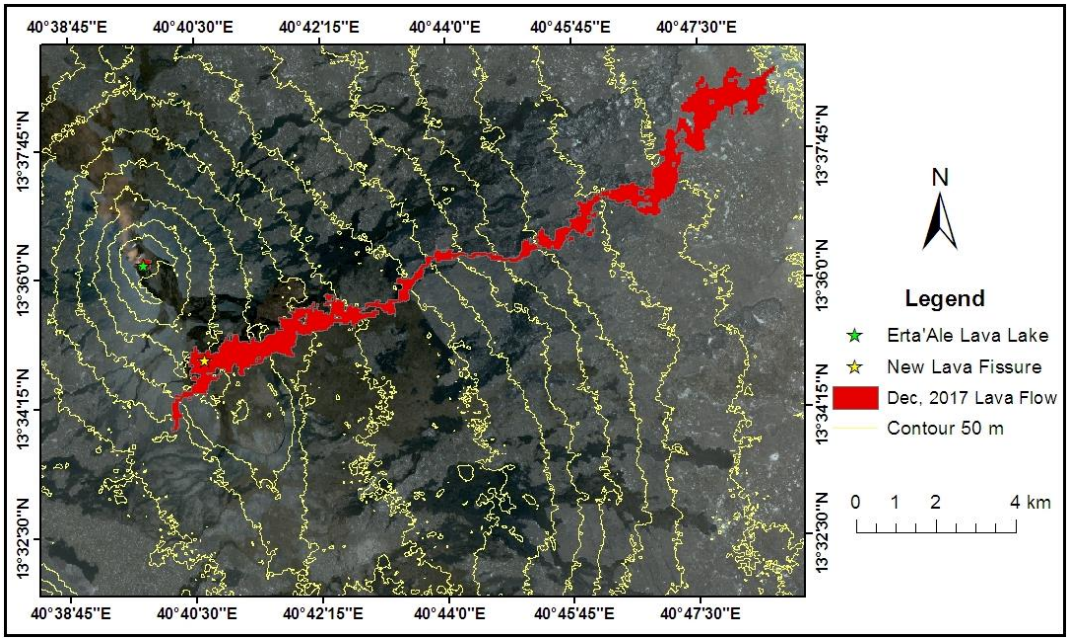

Figure 4.13: Lava flow map (December 2017).

The recent lava flows in Erta 'Ale volcanic range were overlaid together that it used easily to identify the range of lava flows from the youngest to the oldest (no lava flow). The recent volcanic lava flows assessment result indicates lava overflowed from the persistent lava lake of the southern crater and followed by new fissure eruption fed lava flows on January 2017. Before January 2017 the persistent lava lake was active at the north and southern pit crater but no overflow. The activities of a volcanic eruption in 2016−2017 are generally assessed and the result was mapped which is shown in (Fig 4.14) with the color range of dark red to dark blue. The dark red represents no lava flow (oldest lava flow) in the study area range and the dark blue indicates the youngest lava flow in 2016–2017.

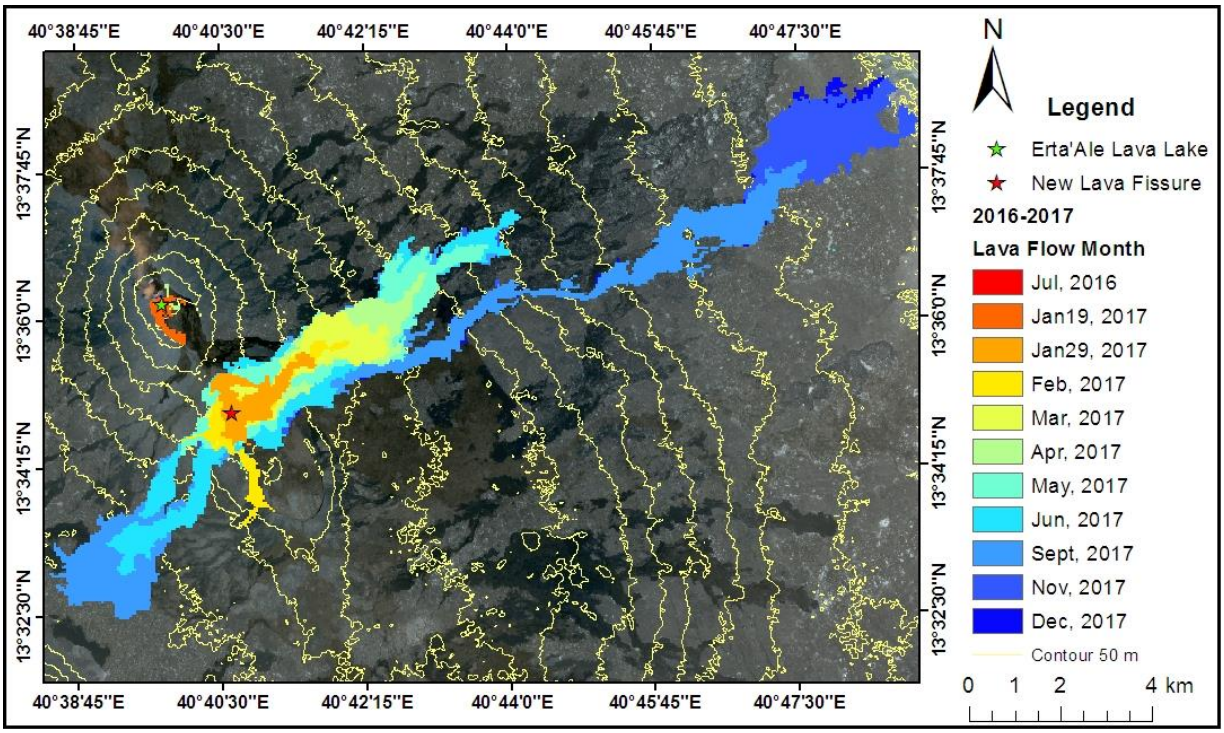

Figure 4.14: Recent lava flow map during (2016−2017).

4.2 Recent lava flow field area

The result of current volcanic lava eruption assessment using multiresolution sentinel-2A optical satellite image indicates that the lava flow field was calculated in km^2 for each lava flow months. The result was presented in (Table 4.1). The maximum area of lava flow field was recorded in November 2017 with its measured value of 24.24 km^2. There is the increasing trend of volcanic lava flow from January to November 2017 but the December lava flow was decreased by 15.89 km^2 and presented in the graph (Fig 4.15).

Table 4.1: Recent lava flow area cover during (2016−2017)

Lava flow (2016–2017)	Area (km^2)	Remark
July 2016	0.05	No lava flow
January 19 2017	0.35	Erta 'Ale lava lake
January 29 2017	1.61	New lava fissures
February 2017	2.50	New lava fissures
March 2017	3.82	New lava fissures
April 2017	4.76	New lava fissures
May 2017	8.05	New lava fissures
June 2017	11.63	New lava fissures
September 2017	19.65	New lava fissures
November 2017	24.24	New lava fissures
December 2017	8.35	New lava fissures

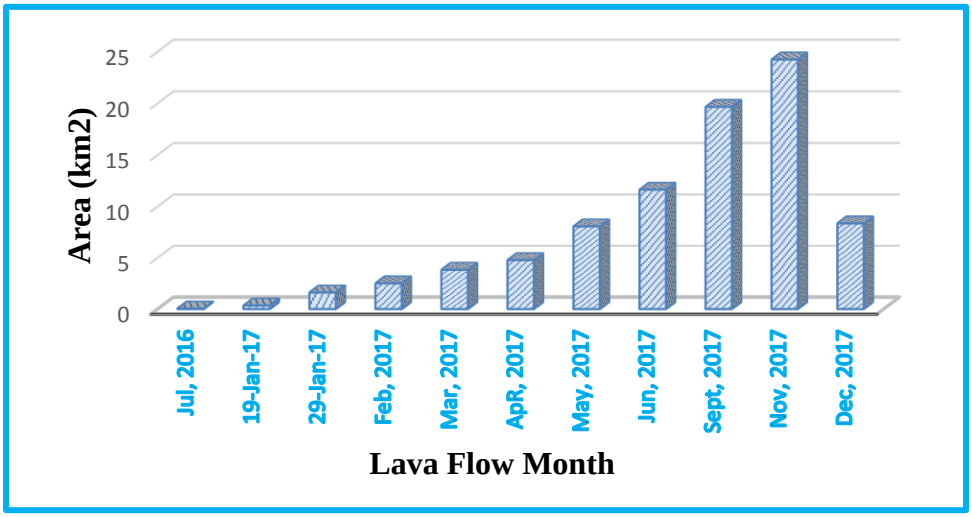

Figure 4.15: Recent lava flow area coverage in Erta 'Ale volcanic range.

The length of lava from the origin to the flow field was measured in km using the geospatial technology. The result indicates the longest lava flow with the measured value of 17.047 km recorded in December 2017. The assessment of recent lava flow shows that the movement of lava from the center to the eastward direction shows an increasing trend from 29th January 2017 to December 2017.

The result was presented in (Table 4.2) and the longest distance of recent lava flow in westward direction was 5.63 km in November 2017.

Table 4.2: Distance of recent lava flow from the origin to flow direction

Lava Flow Month	Distance (km)				
	Lava flow center	North	South	East	West
19th Jan 2017	Erta 'Ale lava lake	-	1.12	-	-
29th Jan 2017	New lava fissure	0.84	0.51	2.04	-
Feb 2017	New lava fissure	0.89	2.84	3.08	-
Mar 2017	New lava fissure	0.94	-	4.04	1.09
Apr 2017	Erta 'Ale lava lake	0.5	0.43	-	-
Apr 2017	New lava fissure	-	-	5.28	-
May 2017	New lava fissure	-	-	6.68	1.49
Jun 2017	New lava fissure	-	-	7.21	4.21
Sept 2017	New lava fissure	-	-	14.26	5.54
Nov 2017	New lava fissure	-	-	16.74	5.63
Dec 2017	New lava fissure	-	-	17.05	2.11

4.3 Recent lava flow direction

The lava that came out the surface from the magma chamber was overflown based on topography before it cools because it is too hot. During 2016−2017 volcanic lava flow assessment, the result indicates lava that flows from the Erta 'Ale lava lake and the new fissure eruption was determined by the downslope of the study area shown in (Fig 4.16). The January lava flow was the direction of the south–west part of the summit of Erta 'Ale volcano with a 1.12 kilometer and rapidly the flows cooled. The new fissure eruption at the southern part of persistent lava lake of Erta 'Ale overflows around all direction. This lava flow on February 2017 was increased in the north-eastward direction of the summit and the southward of the new fissure eruption. In June 2017 the lava flow increased in the south–westward direction and east–northward direction. The south–westward lava flow is cooled in December and no flow in a westward direction.

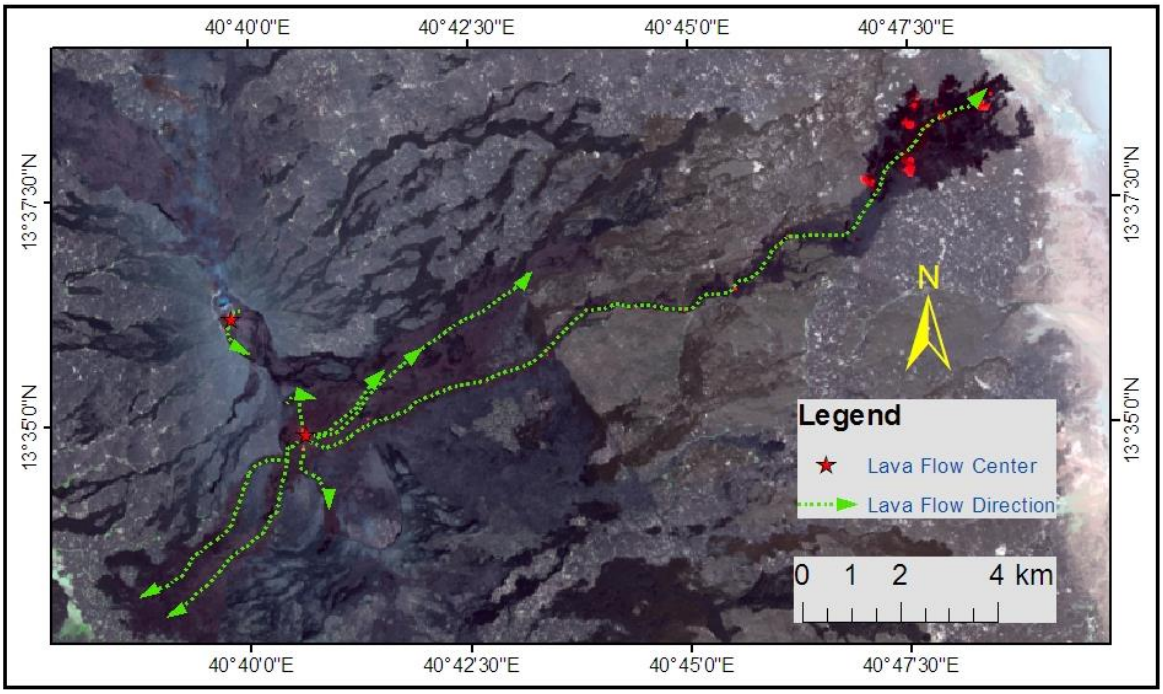

Figure 4.16: Recent lava flow direction map in Erta 'Ale volcanic range.

4.4 Land surface temperature mapping

Land surface temperature is the cumulative temperature of the surface material that is recorded in satellite sensor in the form of heat energy. So, the land surface temperature is estimated from the Landsat 8 thermal remote sensor of band 10 with a spatial resolution of 100 m which is resampled into 30 m for the end product. The land surface temperature variation over the surface of the study area was calculated and mapped in Kelvin. The distribution of land surface temperature in July 2016 was 336.24 k and 299.72 k maximum and minimum temperature, respectively. The result is presented in (Fig 4.17). The color range (blue–red) from the (Fig 4.17) shows the distribution of LST in the study area with red color indicating very high LST distribution value and the blue color indicate that low land surface temperature distribution over the study area. The LST distribution class level and its range were also described in (Table 4.3). The result indicates level I has an LST distribution range between 299.72–306.25 with the low or minimum temperature class unit. Level VI shows a very high land surface temperature distribution.

Table 4.3: Land surface temperature distribution range over the surface (July 2016).

Level	LST distribution Classes	LST distribution range (k)
I	Low	299.72−306.25
II	Moderate	306.25−311.56
III	High	311.56−316.49
IV	Very High	316.49−336.24

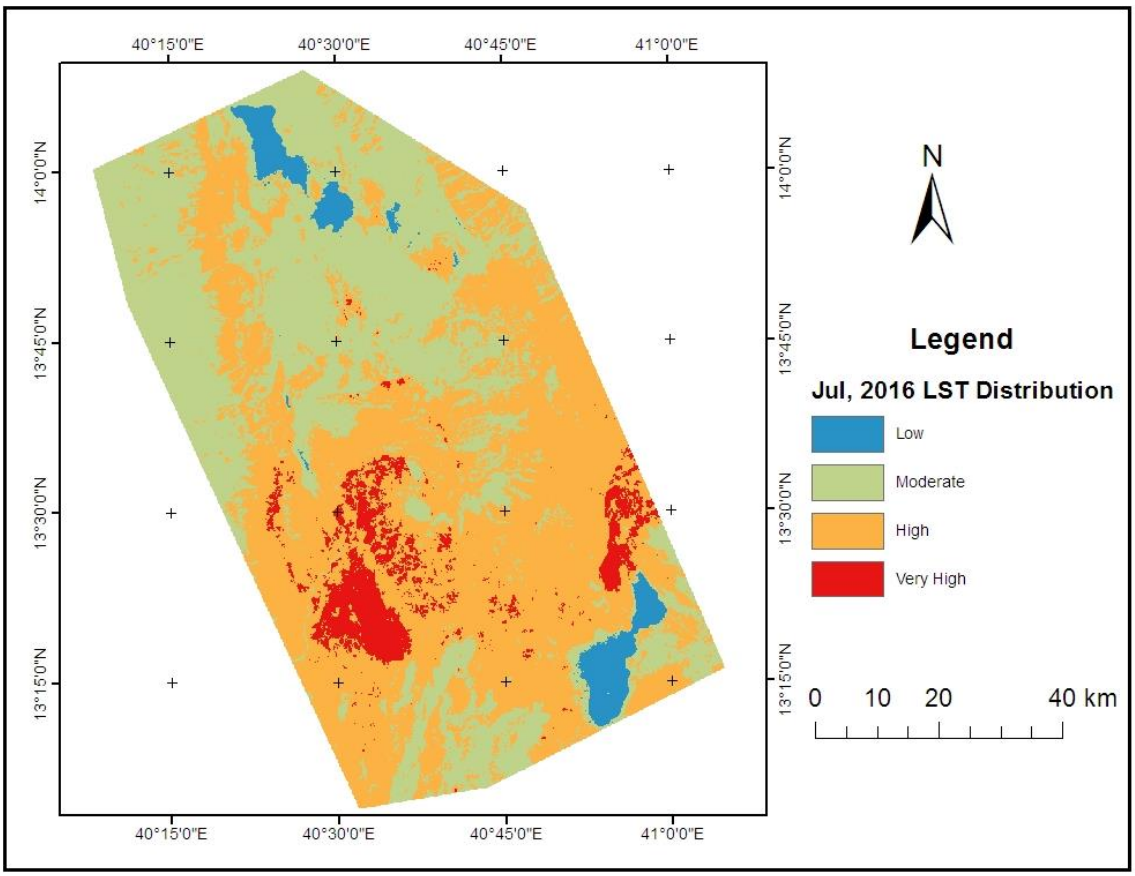

Figure 4.17: Land surface temperature distribution map (July 2016).

The distribution of land surface temperature in January 2017 was widely covered by level II (moderate) land surface temperature distribution. The very high LST distribution covers the small area which is around the Erta 'Ale and other volcanic edifices. The maximum LST recorded from satellite remote sensing was 338.64 k and the minimum was also 304.61 k.

The distribution of LST was mapped in color range from the blue to red and the result is presented in (Fig 4.18 and Table 4.4).

Table 4.4: Land surface temperature distribution range over the surface (January 2017).

Level	LST distribution classes	LST distribution range (k)
I	Low	301.34−304.64
II	Moderate	304.61−312.57
III	High	312.57−321.54
IV	Very High	321.54−338.64

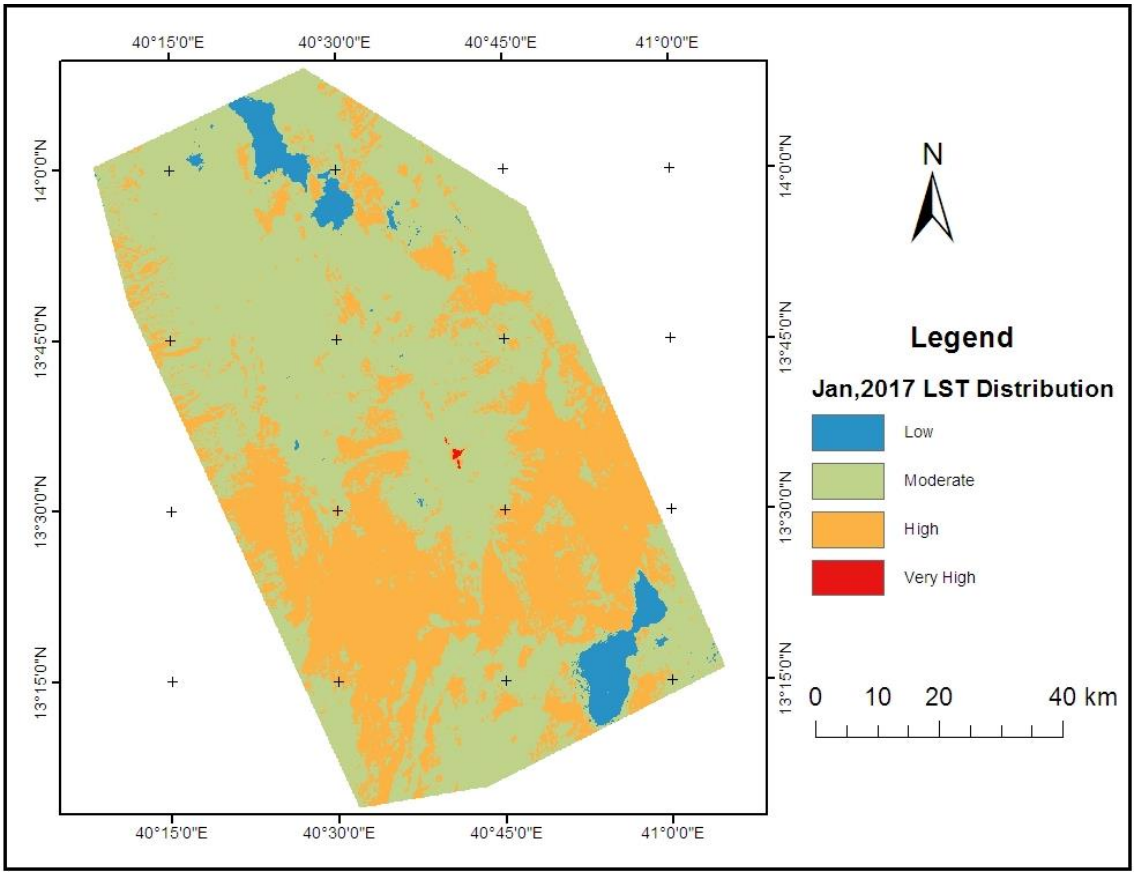

Figure 4.18: Land surface temperature distribution map (January 2017).

The February LST distribution is also presented in (Fig 4.19 and Table 4.5) with the maximum and minimum LST of 355.01 k and 297.13 k, respectively. This month is the top Maximum LST value recorded and distributed around the volcanic activity taking place.

The minimum values are distributed around the lake and different green covered places.

Table 4.5: Land surface temperature distribution range over the surface (February 2017).

Level	LST distribution classes	LST distribution range (k)
I	Low	297.13−304.34
II	Moderate	304.34−319.27
III	High	319.27−336.06
IV	Very High	336.06−355.01

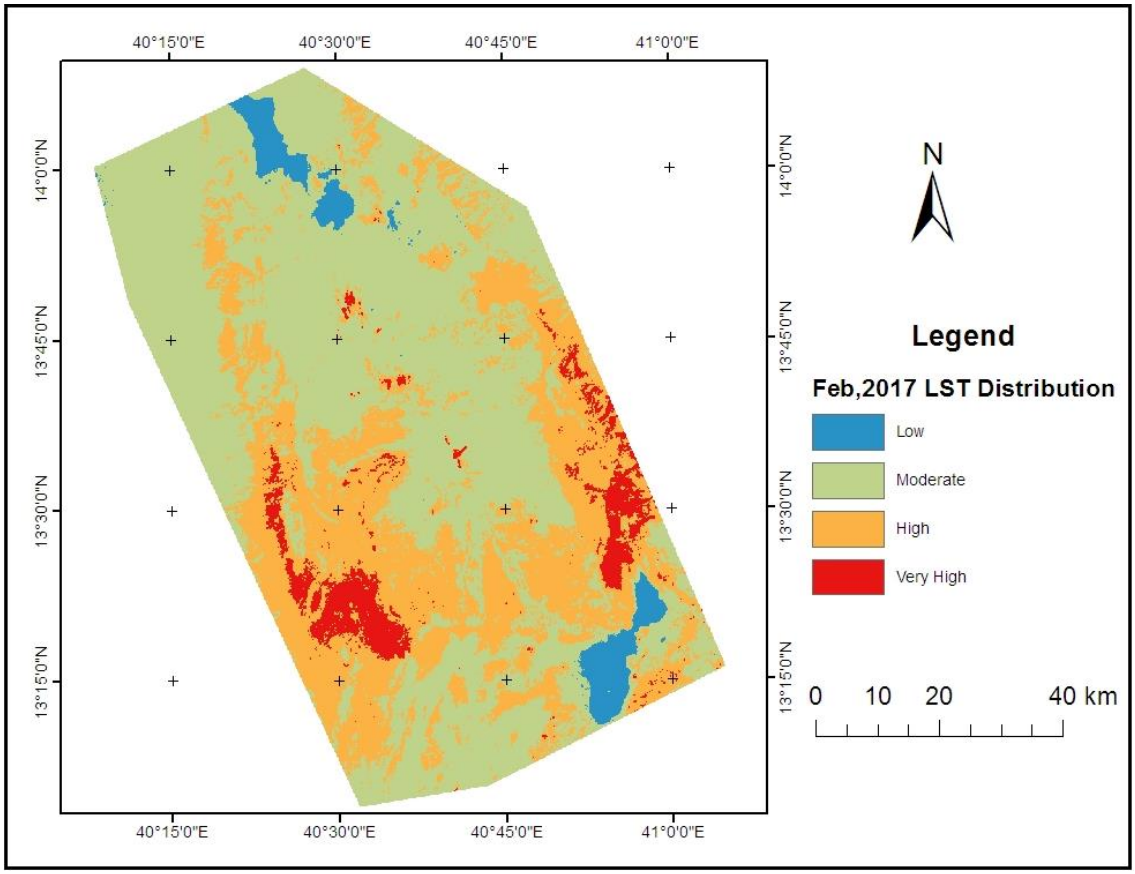

Figure 4.19: Land surface temperature distribution map (February 2017).

Land surface temperature variation in the surface was also mapped in June 2017. The result shows most of the study area was covered by level III (high) land surface temperature distribution on this month. Table 4.6 represents the LST value from 317.36−329.91 distribution covers a large area which was presented by Mango color in (Fig 4.20). The Apple Dust color LST is moderate distribution and the blue color is the list distribution from others.

Table 4.6: Land surface temperature distribution range over the surface (June 2017).

Level	LST distribution classes	LST distribution range (k)
I	Low	300.29−307.87
II	Moderate	307.87−317.36
III	High	317.36−329.91
IV	Very High	329.91−347.05

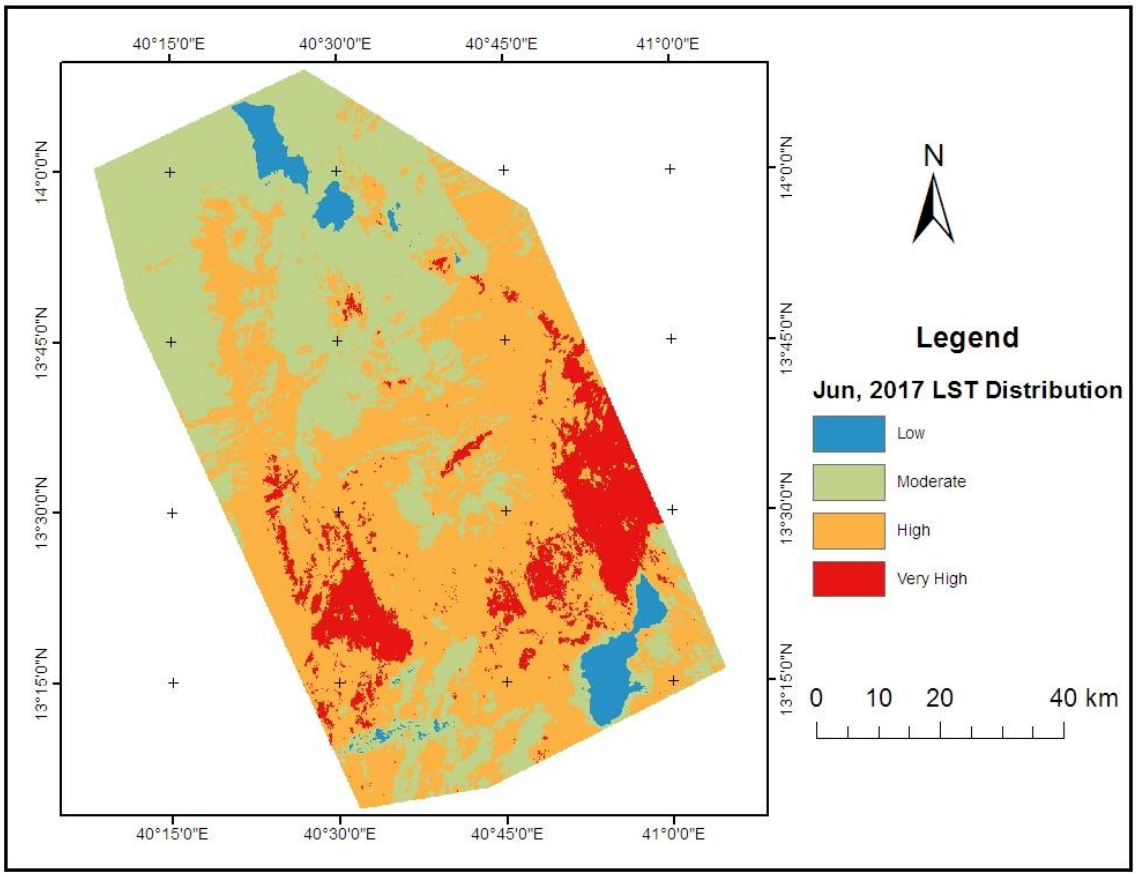

Figure 4.20: Land surface temperature distribution map (June 2017).

The land surface temperature in September 2017 from Landsat-8 thermal band 10 was also calculated with the maximum and minimum temperature of 350.20 k and 299.98 k, respectively. The result is presented in (Fig 4. 21 and Table 4.7). The red color indicates the LST value that is maximum and the blue color represents the distribution of minimum LST over the surface.

Table 4.7: Land surface temperature distribution range over the surface (September 2017).

Level	LST distribution classes	LST distribution range (k)
I	Low	299.98−306.98
II	Moderate	306.98−320.02
III	High	320.02−331.93
IV	Very High	331.93−350.20

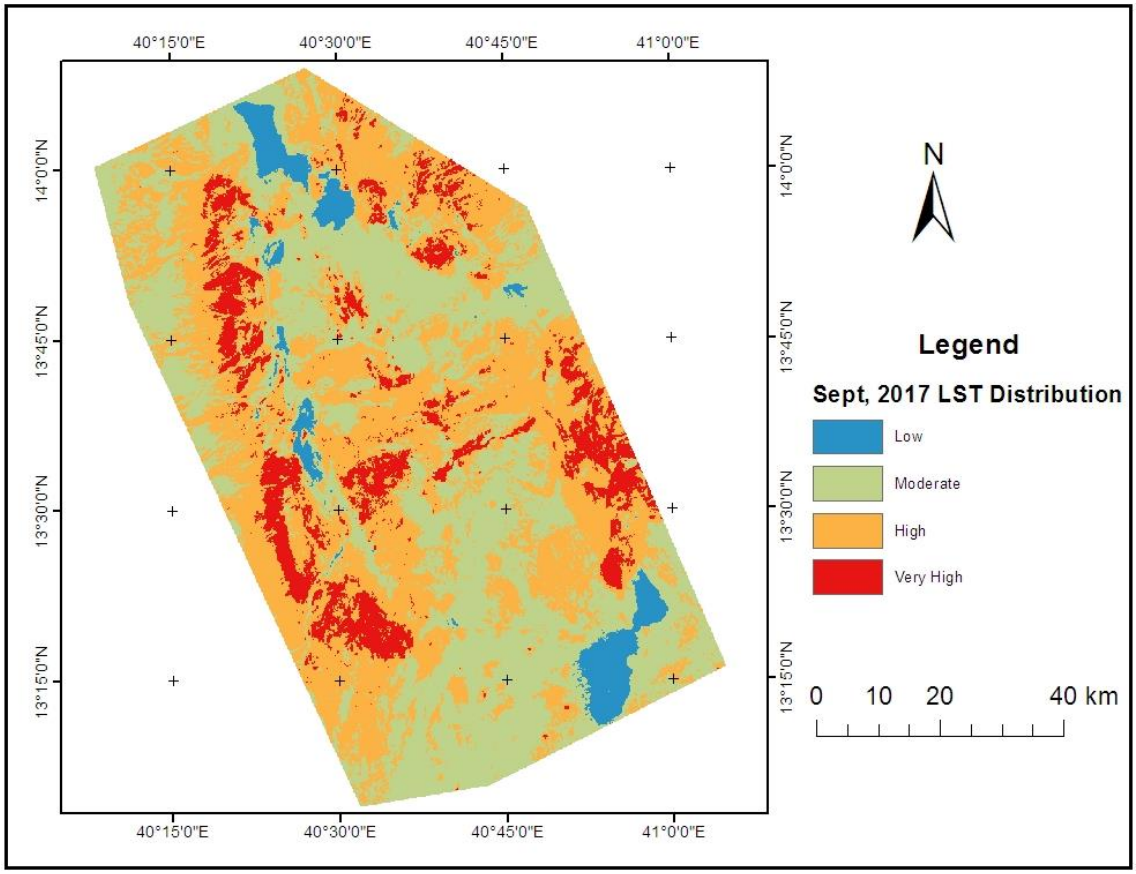

Figure 4.21: Land surface temperature distribution map (September 2017).

November 2017 LST result map which generated from the Landsat-8 thermal band 10 as shown in (Fig 4.22) and the result indicates the larger temperature distribution in the area for this month was level II or Moderate LST distribution. Table 4.8 also describes the maximum, minimum temperature range of the study area. The temperature varies from minimum and maximum LST of 297.81 k to 344.13 k, respectively. The very high LST distribution value was recorded in volcanic lava flow area and other volcanic edifices taking place.

Table 4.8: Land surface temperature distribution range over the surface (November 2017).

Level	LST distribution class	LST distribution range (k)
I	Low	297.81−305.16
II	Moderate	305.16−313.96
III	High	313.96−327.57
IV	Very High	327.57−344.13

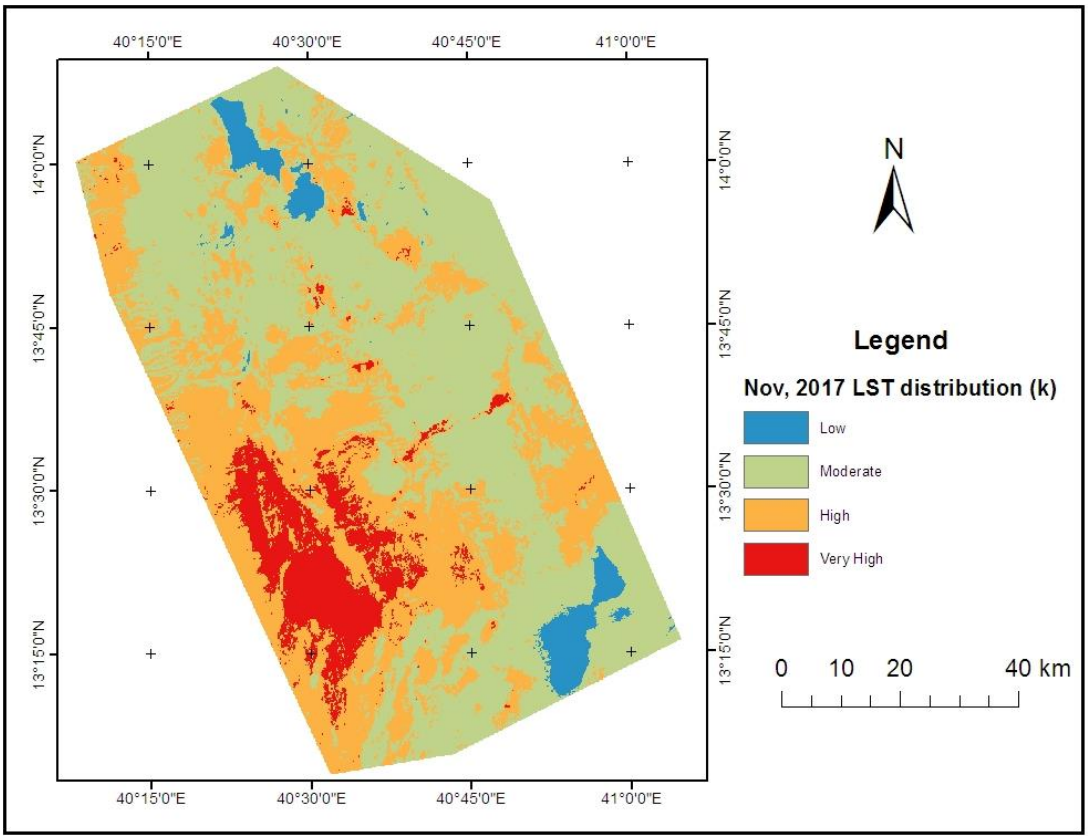

Figure 4.22: Land surface temperature distribution map (November 2017).

4.5 The correlation of lava flow field and land surface temperature

The correlation statistics shows that recent lava flow field and land surface temperature from Landsat 8 thermal infrared band 10 has a positive correlation. Volcanic lava came out the surface from the magma chamber that was too hot the temperature inside the earth's crust. The volcanic lava was formed where the temperature is too hot above such that lava flows and temperature have a positive correlation.

It is obvious to determine as the lava flow increases land surface temperature also increase. The result of the relation of land surface temperature distribution with recent lava flow is summarized and presented in (Fig 4.23). The LST assessment results show that the maximum temperature distribution range is between 316 k to 355 k and this distribution includes the recent lava flow field and those areas of tectonic activities taking place either inside the earth's crust or the surface which is shown in (Fig 4.23 a and b).

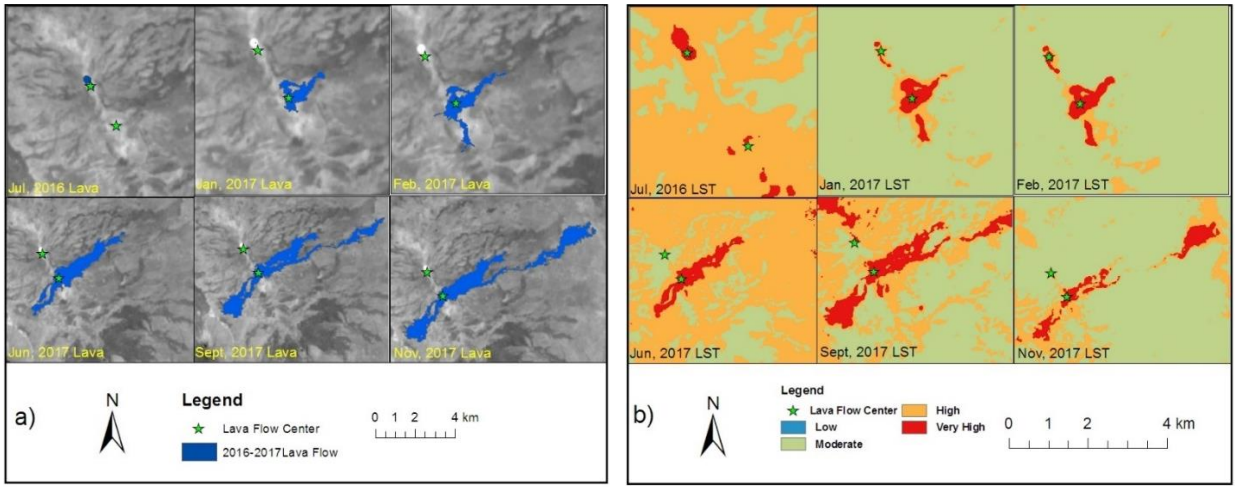

Figure 4.23: The correlation analysis map of the recent volcanic lava flows (a) and the LST distribution (b)

The recent lava flow field mapped from the Sentinel-2A optical satellite image have the maximum land surface temperature distribution record. The lava flow field and the LST distribution linear statistical correlation was shown in (Table 4.9).

Table 4.9: The correlation statistics of recent lava flow and land surface temperature.

	Very high LST distribution (k)	Lava flow area (km^2)
Very high LST distribution (k)	1	0.89
Lava flow area (km^2)	0.89	1

Land surface temperature distribution and the recent lava flow were highly significantly correlated ($r = 0.89$, $p = 0.0005$) to each other while assuming linear relationship and therefore selected for multiple linear regression model development which is shown in scatterplot (Fig 4.24). The result indicates as lava flow field increases the maximum value of LST distribution also increase which resulting in a strong positive linearly correlation.

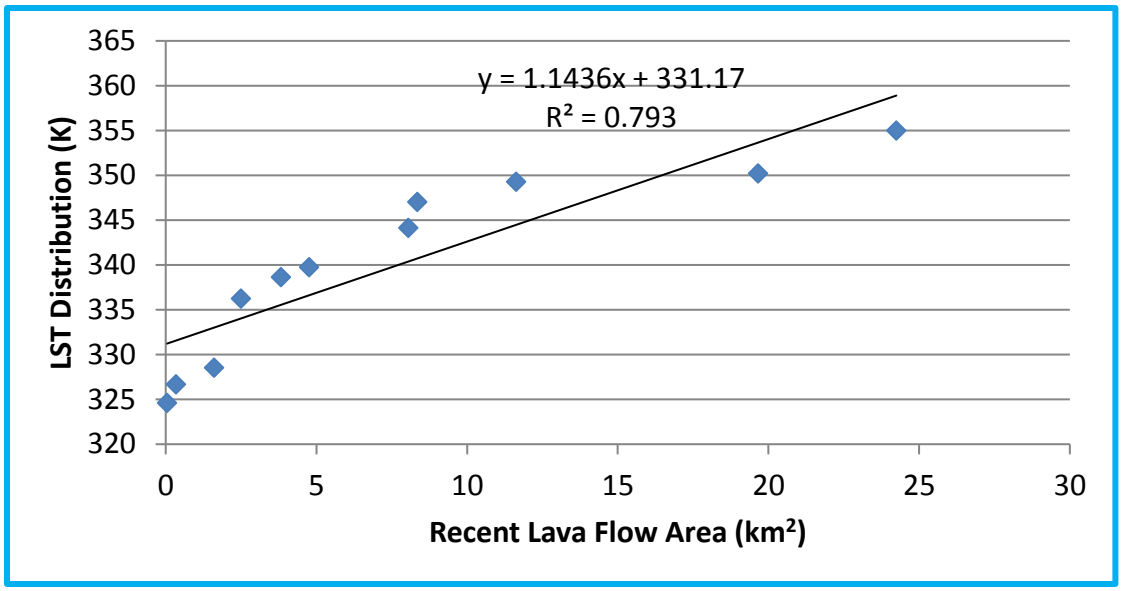

Figure 4.24: Scatterplot showing correlation of land surface temperature distribution and recent lava flow

4.6 Model validation

4.6.1 Modis Terra LST series product

Land surface temperature from Landsat-8 thermal remote sensor was validated by using MODIS Terra LST products were used. Five sample locations were selected using spatial polygons overlay over the land surface temperature to validate its results. Sample "A" polygon was located at the southern part of study area including some parts of Lake Afreda. Sample "B" locates the recent lava flow fields and "C" at the northern part of the study area. Sample polygons "D" and "E" were also distributed to the west and center of recent study area respectively. The result was also presented in Table 4.8 and the maximum, minimum and average temperature of both Modis Terra LST product and the Landsat-8 band10 results were comparatively described. Each result of Landsat-8 thermal band 10 LST was validated by the Modis data and the result shows that their maximum difference lies below 2^{o}C. Therefore, the result of LST from Landsat 8 thermal band 10 was validated by both the Modis LST product of the study area.

Table 4.10: Statistical comparison of Landsat-8 thermal Band 10 LST and Modis LST during 2016−2017.

Sample Location	Sensor	Spatial resolution	Minimum (k)	Maximum (k)	Average (k)	Standard deviation	Average difference
A	TIRs B10	30 m	297.44	321.95	311.99	3.91	1.08
	Modis	1 km	303.46	317.52	310.92	4.74	
B	TIRs B10	30 m	307.64	338.03	328.01	3.70	1.11
	Modis	1 km	323.48	329.92	326.89	2.93	
C	TIRs B10	30 m	304.04	331.76	320.94	1.46	1.35
	Modis	1 km	316	322.66	319.59	1.65	
D	TIRs B10	30 m	298.13	336.55	317.61	3.45	0.63
	Modis	1 km	306.12	321.86	316.98	4.70	
E	TIRs B10	30 m	307.40	334.38	323.86	1.05	0.50
	Modis	1 km	321.88	325.12	323.36	0.90	

4.6.2 Accuracy assessment

To validate recent lava flow map result, sample points were taken from the Landsat 8 LST results. These sample points were displayed on recent lava flow map to show whether the result was matched or not. This is because lava flow and land surface temperature have a positive correlation. The points that displayed on very high LST distribution area were also matched with recent lava flow field. The result indicates November 2017, total of 81 sample points, 29 were collected from inside a very high LST distribution area. This sample points were also displayed inside the recent lava flow field and the result was validated by matching the sample points both on LST and lava flow field map. There are no sample points outside the recent lava flows map and the result was 100 % accurate. The result was shown in (Fig 4.25).

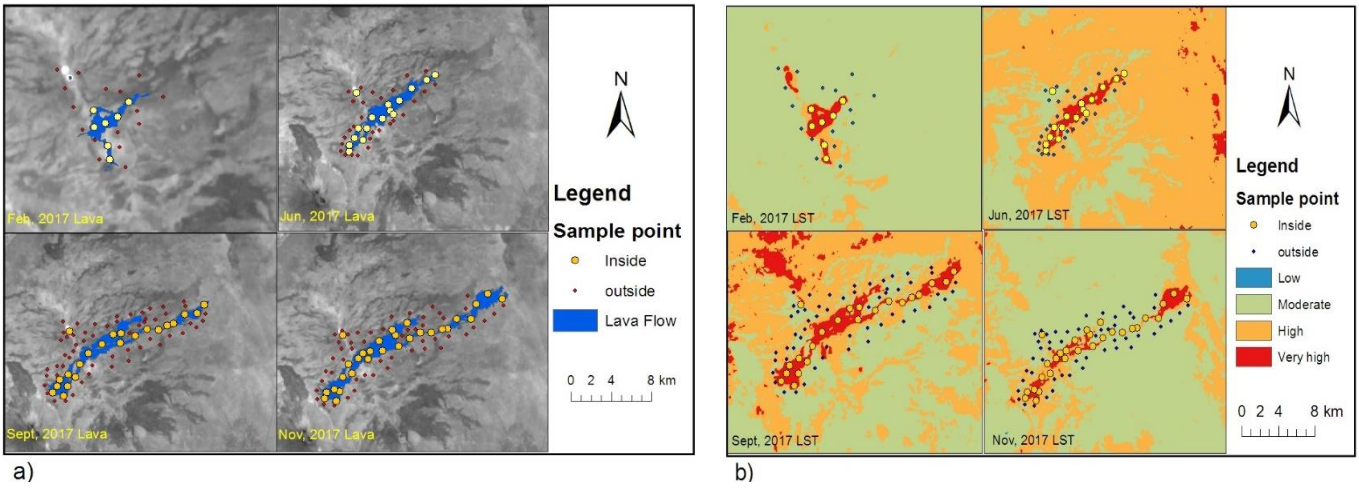

Figure 4.25: Accuracy assessment (a) recent lava flow map and (b) LST

CHAPTER FIVE

DISCUSSION

Danakil depression is a part of Afar depression that contains most of the Active volcanoes especially the shield basaltic volcano called Erta 'Ale lava lake. This active lava lake volcano in Ethiopia first confirmed historical observations were made in 1906 (Global volcanism program, 2017). Activities of the tectonic and related earth material movements can cause the surface temperature variability over the area because the magma that erupted in the surface of the earth is too hot as well after lava comes out into the surface so too cool. Some of the natural hazards especially volcanic eruption (Bell, 2002) largely and the regularly happening area is very difficult in situ measurement of the lava flow (Lu *et al.*, 2010) and the surface temperature. Geospatial technology has the power to collect, analyze, interpret and present the information about such circumstances.

The retrieval of land surface temperature requires a high quality of input data and the preprocessing of individual data set especially data calibration to output stages. Sensor brightness temperature is one of basic requirement to estimate Land surface temperature so far, the DN value of input Landsat 8 (band10) image should be converted to sensor radiance which is the intrinsic factor to estimate at sensor brightness temperature (Landsat 8, 2016). The other factors that used to calculate the land surface temperature from Landsat8 thermal remote sensor band10 are NDVI based emissivity estimation over the surface (Qin *et al*., 2011; Perez Hoyos, 2014). The range of emissivity value calculated using threshold (Sobrino *et al*., 2004) is for bare soil, vegetation and both the mixture of bare soil and vegetation. But the study area also includes the different types of geological units or rocks and their emissivity value considerably lies between the mixture of bare soil and vegetation.

There are different types of models, algorithms, and formula developed by different scholars and researchers to estimate sea surface temperature and land surface temperature for different types of sensors (Jimenez-Munoz and Sobrino, 2004; Jimenez-Munoz *et al*., 2014; Jin *et al.*, 2015). Landsat 8 has the thermal sensor with two thermal bands (Landsat 8, 2016) that record the emitted energy from the surface which is used to estimate the land surface temperature. Before Landsat 8 launched, the Landsat family group were also used to estimate land surface temperature.

These Landsat families are Landsat (Multispectral scanner, thematic mapper, and enhanced thematic mapper plus). The thermal band of this Landsat family is different from the Landsat 8 thermal band by their resolution, band number, and their preprocessing capability. Therefore, except for Operational Land Imagery, all Landsat family has a single thermal band. This family of the thermal band was processed by using single channel algorithm or mono-window algorithm (Artis and Carnahan, 1982; Jimenez-Munoz and Sobrino, 2004; Sobrino *et al*., 2004; Jimenez-Munoz *et al.*, 2014; Wang *et al*., 2016) to estimate land surface temperature. The recently launched Landsat 8 has two spectrally adjacent thermal channels i.e. band10 and band 11, both the single channel and split-window methods were employed for retrieving LST (Rozenstein *et al*., 2014; Wang *et al*., 2016). But Landsat 8 thermal band11 is not much important for LST calculation because a serious radiometric calibration error induced by stray light effects (Montanaro *et al*., 2014; Wang *et al*., 2016) such that even Landsat 8 has two thermal band, it is better using band 10 to retrieve LST (Wang *et al*., 2016; Xiaolei *et al*., 2014) because it is accurate and provide more information.

LST is a basic determinant of the terrestrial thermal behavior, as it controls the effective radiating temperature of the Earth's surface. Due to the extreme heterogeneity of most natural land surface, there are different kinds of factors that can fundamentally influence the derivation of LST such as: temperature variations with angles; sub-pixel in-homogeneities in temperature and cover; surface spectral emissivity at the channel wavelengths; atmospheric temperature and humidity variations; and clouds and large aerosol particles such as dust (Sentinel-3 online, 2018).

Erta Ale is one of active basaltic shield volcano having the persistent lava lake throughout the year. Its surface temperature is measured by many researchers using different thermal infrared instruments such as thermocouple and a pyrometer to measure the lava lake crust temperature (Burgi *et al*., 2002); Agema Thermovision 550 infrared camera equipped with a Stirling-cooled, focal plane array of PtSi detectors (Oppenheimer and Gezahegn, 2002); A handheld P65 thermal Infrared camera manufactured by FLIR (Forward Looking Infra-Red) Systems (Spampinato *et al*., 2008; Davies *et al*., 2011). These thermal infrared camera instruments acquire high spatial and temporal resolution images with the pixel size of 0.1meter (Spampinato *et al*., 2008).

The recent 2016−2017 LST distribution in Erta Ale volcanic range is estimated from Landsat-8 thermal infrared band 10 using single channel algorithm.

According to Oppenheimer and Francis (1997) by compiling a time series of Landsat MSS and TM, JERS-1, SPOT, and AVHRR digital imagery, and space-borne photographic data, non-saturated Landsat MSS and TM data could indicate that crust temperature (Ts) are much lower than they assumed, that there is significant absorption in band 6 of thermal emission from the lava lake surface by fumes, and/or that the lake occupies a smaller fraction of the sensor IFOV.

According to Flynn *et al*. (2001) using Landsat 7 thermal band 6 overpass they measured surface crust temperatures of just 40–111ºC on an active blocky lava flow emerging from Santiaguito's Caliente vent. These low temperatures were due to the very thick crusts covering the molten component of the flow. So that the surface crust away from the vent had undergone significant cooling. This conclusion basically supports the current result of land surface temperature (82ºC) even the study area is so different by considering the thermal sensor used was a Landsat group and the same kind of object measurement.

The current result LST was also validated by the Modis 11A2 Terra LST product data. Five sample locations were selected as a polygon to validate the statistics of both Landsat 8 and Modis LST products. For each polygon sample, the average values were used to validate the result. Modis Terra LST product with 1 km and Landsat-8 30 m was statistically analyzed and their maximum average difference is 1.35ºC. According to Qin *et al*. (2011), the average difference of Landsat LST and Modis LST is less than 2ºC then the result was acceptable. Therefore, the current LST from Landsat 8 thermal infrared band 10 is a valid result. Erta `Ale range, the normal faults and gaping fissures that slice it, and the summit caldera of Erta `Ale volcano, all share the same NNW-SSE (Eritrean) orientation, sub-parallel to the Red Sea rift (Oppenheimer and Francis, 1997).

Young lava eruptions field mapping is logistically difficult, Lu *et al*. (2004) and optical images from different kinds of sensors are very important and for this purpose are greatly reduced by persistent cloud cover. Recent lava eruptions (2017) was mapped using the geospatial tools and the result indicates that the lava flow starts from January 19, 2017. New volcanic lava center (fissure) was opened at the southern direction of the Erta `Ale lava lake in between January 19–29, 2017. Sentinel–2A provide the satellite images within the temporal resolution of 10 days. The exact date of new lava flow center is not identified but the flow starts from january19−29, 2017.

Before January 19 there is no new volcanic lava flow rather from the Erta `Ale lava lake. In general, the day of new volcanic lava opening center is between January 19, 2017, and January 29, 2017. During the assessment of 2016 volcanic activity, there was no new fissures eruption as well as lava

flow in this year. The global volcanism program (2017) report indicates also except January and November 2016 the lava lake is active on its caldera by rising and falling at the southern crater of the rim which is shown in (Fig 5.1). In mid-January and November 2016, the lava lake overflowed on its rim.

Figure 5.1: Erta 'Ale's lava lake at the S crater on 29 December 2016.

(Source: Photo by Jens Wolfram Erben, (https:// www.volcano discovery.com/ertaale/news/ 61284/Erta-Ale-volcano- Ethiopia- field-report-29-Dec-2016-1-Jan-2017.html).

To reduce the redundancy of map without any information, as the final output only July 2016 data was mapped and this also shows the progressive of lava from no flow to current flow. The 2017 lava flow was also mapped using Sentinel-2A satellite image. Recently mapped lava flow months are January-June, September, November, and December. Other three months namely; July, August and October lava flows were not mapped due to the quality of the satellite image. Almost all data were covered by the cloud and this produces an error during the processing and the final output map. The recent lava flows were identified and classified by eCognition software in false color composite (band 6, band 4, and band 3). The classification algorithm is geospatial object-based image classification and only recent lava flow was mapped because the objective of this paper is to map the recent lava flows. The current lava flow direction from the new opening volcanic lava was east–north and west–south of the Erta `Ale range.

CHAPTER SIX

CONCLUSION AND RECOMMENDATIONS

6.1 Conclusion

The Afar depression is one of the lowest elevated and the hottest place with its interesting topography due to the tectonic activities of the area. The location of current study area includes the Danakil depression of Erta 'Ale volcanic range and the surrounding environment. Erta 'Ale volcanic range contains a number of active volcanic edifices such that Erta 'Ale lava lake is one of the basaltic shield volcano having persistent lava lake throughout the year. The activity of this lava lake (southern crater) is active by rising and falling at the rim in 2016. Mid-January and November 2016 the lava lake overflowed around the rim. This overflow is not long and the same as the 2017 lava flow because it overflows around the rim and then rapidly ceased. The recent volcanic lava flows for a long distance from the new fissure eruption to the east-northward and west-southward direction. The result was processed using geospatial object-based image classification algorithm using the eCognition software and the recent lava flow field was mapped.

The assessment result using sentinel-2A optical satellite image indicates there was no a significant volcanic lava flow in the year of 2016. The recent lava flow from the southern crater of Erta 'Ale volcanic caldera and the new fissure eruption was assessed using the geospatial tools. The origin of the recent lava flow is from the Erta 'Ale volcanic caldera southern crater and the new lava fissure eruption at the southern part of Erta 'Ale lava lake within 4.5 km distance. The old lava flow moves for 1.12 km and cooled. Lava from new fissures starts overflowing at the end of January 2017 by increasing both the area coverage and distance of flow field. December 2017 the lava flow field reduced but the longest distance of lava flow was measured in kilometer. The maximum lava flow field measured was in November 2017 and its area is 24.24 km^2.

Land surface temperature is the temperature of the top surface condition and the effective emitting temperature of the features or the radiative skin temperature of the land derived from solar radiation which the sensor records emitted energy in the form of heat. The distribution of land surface temperature over the study area is assessed from the Landsat 8 thermal infrared band 10 and the result was also validated by Modis Terra LST products. NDVI based emissivity calculation was used to retrieve LST from the thermal infrared sensor of band 10 satellite image using the single-channel algorithm.

The maximum temperature distribution includes the recent lava flow field and it has a strong positive correlation with lava flow field. The moderate temperature class covers a large area for all study year and the result was also mapped.

6.2 Recommendations

Volcanic activity is a natural hazard that damages the resources and causes loss of life during the eruption. It should be better if the activity of each lava flow and a volcanic eruption is recorded, studied and documented for the future studies, prevention and prediction of hazard. It is also recommended to use high temporal resolution images to clearly identify and map the timing, extent and variation of the volcanic lava eruptions. Landsat 8 thermal sensor collects the data within 100 m with a temporal variability of 16 days at the height of 705 km. This sensor has no the ability to exactly measure the lava flow temperature during the eruption and lava flow. It is recommended to use a very high spatial and temporal resolution sensor mounted on aircraft or handheld thermal infrared instrument to measure volcanic lava temperature. Both thermal bands of Landsat-8, atmospheric gas constituent analysis from images and radar interferometry for Swelling of domes before lava eruption are required.

References

Abbate, E., Bruni, P., and Sagri, M. (2015). Geology of Ethiopia: A Review and Geomorphological Perspectives. *World Geomorphological Landscapes*. **2**(1): 132–64. DOI: 10.1007/978-94-017-8026-1-2.

Abrams, M., Abbott, E., and Kahle, A. (1991). The combined use of visible reflected infrared, and thermal infrared images for mapping Hawaiian lava flows. *Journal of Geophysical. Research*. **96**: 475–484.

Alebachew Beyene, and Mohamed, G. Abdeselam. (2005). Tectonics of the Afar Depression: A review and synthesis. *Journal of African Earth Sciences***. 41**: 41–59.

Aplin, P. and Smith, G.M. (2008). Advances in Object-Based Image Classification**.** *The Int. Archives of the Photogrammetry, Remote Sensing and Spatial Information Sciences.* **xxxvii**(B7): 725−728.

Artis, D.A., and Carnahan, W.H. (1982). Survey of emissivity variability in thermography of urban areas. *Remote Sensing of Environment.* **12**(4): 313–329.

Aspinall, M., Thea, A., Susan, H., Farrokh, M., Jenny, N., Sparks, P.S. and Syre, E. (2011). Volcano hazards and exposure in GFDRR priority counties and risk mitigation measures, Report Washington D.C.

Baker, B. H., Mohr, P. A., and Williams, L. A. J. (1972). Geology of the Eastern Rift System of Africa. *Geol. Soc. Am. Spec. Pap.* **136**: 1–67. Doi:10.1130/SPE136–p1.

Barberi, F., and Varet, J. (1970). The Erta Ale volcanic range (Danakil depression, northern Afar Ethiopia) Bull. *Volcanology*. **34**: 848–917.

Barnie, T. D., Keir, D., Hamling, I., Hofmann, B., Belachew, M., and Carn, S. (2015). A multidisciplinary study of the final episode of the Manda Hararo dike sequence, Ethiopia and implications for trends in volcanism during rifting cycle, in *Magmatic Rifting and Active Volcanism*. (eds., Wright, T. J., Ayele, A., Ferguson, D. J., Kidane, T., and Vye-Brown, C.) London. *Geological Society*. 420 pp.

Bell, F. G. (2002). *Geologic Hazard: their assessment avoidance and mitigation*. Tyler & Frances, 631pp.

Blaschke, T. (2010). Object-based image analysis for remote sensing. *ISPRS Journal of Photogrammetry and Remote Sensing.* **65**: 2–16.

Bonneville, A. (1992). La surveillance des volcans par satellite. *La recherche*. **24**(2) : 404–413.

Bonneville, A., and Kerr, Y. (1985). A thermal forerunner of the 28th March 1983, Mt Etna eruption from satellite thermal infrared data. *Journal of Geodynamics*. **7**: 1–31.

British geological survey. (1999). Global geohazards: volcanic hazard, vulnerability, and risk assessment. 1–34.

Brown, S.K., Sparks, R.S.J., Mee, K., Vye-Brown, C., Ilyinskaya, E., Jenkins, S.F., and Loughlin, S.C. (2015). Country and regional profiles of volcanic hazard and risk. *Global Volcanic Hazards and Risk.* Cambridge University Press, Cambridge.

Burgi, P.-Y., Callet, M., and Haefeli, S. (2002). Field temperature measurements at Erta'Ale Lava Lake. *Ethiopia Bull Volcanology*. **64**: 472–485.

Casadevall, T. J. (1991). First International Symposium on Volcanic Ash and Aviation Safety Program and Abstracts, Seattle, Wa., U.S. Geological Survey, Circular 1065.

Central Statistical Agency (2007). Summary and statistical report of 2007 population and housing census. *Addis Ababa Central Statistical Agency.*

Damiani, M.L., Groppelli, G., Norini, G., Bertino, E., Gigliuto, A., and Nucita, A. (2006). A lava flow simulation model for the development of volcanic hazard maps for Mount Etna (Italy). *Computers and Geosciences*. **32**: 512–526.

Davies, A. G., Keszthelyi, L., and McEwen, A. S. (2011). Estimating eruption temperature from thermal emission spectra of lava fountain activity in the Erta'Ale (Ethiopia) volcano lava lake: Implications for observing Io's volcanoes. *Geophysical Research Letter*. **38**, L21308. Doi:10.1029/2011GL049418.

Eagles, G., Gloaguen, R., and Ebinger, C. (2002). Kinematics of the Danakil microplate. *Earth and Planetary Science Letters.* **203:** 607–620.

Flynn, L.P., Harris, A.J.L., and Wright, R. (2001). Improved identification of volcanic features using Landsat 7 ETM+. *Remote Sensing of Environment***. 78**: 180– 193.

Galati, S.R. (2006). *Geographic Information Systems Demystified.* Artech House, Inc, Boston London, 297pp.

Gandhi, M.G., Parthiban, S., Thummalu, N., and Christy. A. (2015). Ndvi: Vegetation change detection using remote sensing and GIS – A case study of Vellore District. In: proceeding 3rd Int. Conf. on Recent Trends in Computing. *Procedia Computer Science*. **57:** 1199 – 1210.

Gao, B.C., and Kaufman, Y.J. (1995). Selection of the 1.375 micrometers MODIS Channel for Remote Sensing of Cirrus Clouds and Stratospheric Aerosols from Space. *Journal of the Atmospheric Sciences*. **52**(23): 4231–4237.

Geological Survey of Ethiopia, January 2015, Ministry of Mines, Addis Ababa.

Gezahegn Yirgu (2009). An outline of the East African Rift Volcanism. Advanced Workshop on Evaluating, Monitoring and Communicating Volcanic and Seismic Hazards in East Africa.

Glaze, L. S., Francis, P. W., Self, S., and Rothery, D. A. (1989). The Lascar September 16, 1986 eruption: Satellite Investigations. *Bulletin of Volcanology*. **51**: 149–160.

Global Volcanism Program, 2017. Report on Erta 'Ale (Ethiopia). In: Venzke, E (ed.), Bulletin of the Global Volcanism Network, 42:7. Smithsonian Institution.

Gong, L., Li, N., Fan, Q., Zhao, Y., Zhang, L., and Zhang, C. (2016). Mapping the topography and cone morphology of the Dalinor volcanic swarm in Inner Mongolia with remote sensing and DEM Data. *Front. Earth Sci*. **10**(3): 578–594. DOI: 10.1007/s11707-015-0536-1.

Gonnermann, H.M., and Manga, M. (2007). The Fluid Mechanics Inside a Volcano. *Annu. Rev. Fluid Mech*. **39**: 321–356. Doi: 10.1146/annurev.fluid.39.050905.110207.

Harris, A.J.L., Wright, R., And Flynn, L.P., (1999). Remote monitoring of Mount Erebus Volcano, Antarctica, using polar orbiters: Progress and prospects. *International Journal of Remote Sensing*. **20**. 3051–3071.

Jimenez-Munoz, J.C. and Sobrino, J. A. (2004). Correction to ''A generalized single-channel method for retrieving land surface temperature from remote sensing data''. *Geophysical Research.* **109**: D08112. Doi:10.1029/2004JD004804.

Jimenez-Munoz, J.C., Sobrino, J.A., Skokovic, D., Mattar, C., and Cristobal, J. (2014). Land surface temperature retrieval methods from Landsat-8 thermal infrared sensor data. *IEEE Geosci. Remote Sensing Letter*. **11:** 1840–1843.

Jin, M., Li, J., Wang, C., and Shang, R. (2015). A Practical Split-Window Algorithm for Retrieving Land Surface Temperature from Landsat 8 Data and a Case Study of an Urban Area in China. *Remote Sensing.* **7**: 4371–4390. Doi:10.3390/rs70404371.

Kervyn, M., Kervyn, F., Goossens, R., Rowland, S.K., and Ernst, G.G.J. (2007). Mapping volcanic terrain using high-resolution and 3D satellite remote sensing. *Geological Society London Special Publications*. **283**: 5–30. DOI: 10.1144/SP283.2.

Landsat-8, (2016). USGS Landsat8 data user's handbook. (http:// landsat.usgs.gov/ best spectral bands to use. php).

Latif, M.S. (2014). Land Surface Temperature Retrieval of Landsat-8 Data Using Split-Window Algorithm- A Case Study of Ranchi District IJEDR. *International Journal of Engineering Development and Research.* **2**(4): 3840–3849.

Lelisa, Seena, and Kifle, Woldemariam. (2006). Disaster prevention and preparedness in collaboration with the Ethiopia Public Health Training Initiative, The Carter Center, the Ethiopia Ministry of Health, and the Ethiopia Ministry of Education. unpublished document.

Levin, N., (1999). *Fundamentals of Remote Sensing.* International Maritime Academy. Trieste, Italy, 225pp.

Li, Z., Tang, B., Wu, H., Ren, H., Yan, G., Wan, Z., Isabel F. Trigo, I.F., and Sobrino, J.A. (2013). Satellite-derived land surface temperature: Current status and perspectives. *Remote Sensing of Environment*. **131**:14–37.

Lu, Z., Daniel, D., Hyung-Sup, J., Jixian, Z., and, Yonghong, Z. (2010). Radar image and data fusion for natural hazards characterization. *International Journal of Image and Data Fusion*. **1(**3): 217 – 242.

Lu, Z., Rykhus, R., Masterlark, T., and Dean, K. G. (2004). Mapping recent lava flows at Westdahl Volcano, Alaska, using radar and optical satellite imagery. *Remote Sensing of Environment*. **91**: 345–353.

Mallick, J., Singh, C.K., Shashtri, S., Rahman, A., and Mukherjee, S. (2012). Land surface emissivity retrieval based on moisture index from Landsat TM satellite data over heterogeneous surfaces of Delhi city. *International. Journal of Applied Earth Observation and Geoinformation*. **19**: 348–358.

Mesfin, Asfaw, and Yohannes, Ermias., (2014). The Geology of Northern Danakil Depression and its Geothermal Significance. **In** Proceedings 5th African Rift Geothermal Conference Arusha, Tanzania, Oct, 29–31. Ministry of Energy and Mines, Department of Mines. 1–6.

Michael, E. Z., Tobias, P. F., Maarten de Moor, J., Bernard, M., Laurent, Z., Dereje, A., Aleksey, N., and Vasilii, K. (2013). Trace elements in the gas emissions from the Erta Ale volcano, Afar, Ethiopia. *chemical geology*. **357**: 95–116.

Miyamoto, H., Haruyama, J., Kobayashi, T., Suzuki, K., Okada, T., Nishibori, T., Showman, A.P., Lorenz, R., Mogi, K., Crown, D. A., Rodriguez, J. A. P., Rokugawa, S., Tokunaga, T., and Masumoto, K. (2005). Mapping the structure and depth of lava tubes using ground penetrating radar. *Geophysical Research Letters*. **32**: 1–5. Doi:10.1029/2005GL024159.

Montanaro, M., Gerace, A., Lunsford, A., and Reuter, D. (2014). Stray light artifacts in imagery from the Landsat 8 Thermal Infrared Sensor. *Remote Sensing*. **6**(11): 10435–10456.

Naranjo, M. F., Ebmeier, S. K., Vallejo, S., Ramon, P., Mothes, P., Biggs, J., and Herrera, F. (2016). Mapping and measuring lava volumes from 2002 to 2009 at El Reventador Volcano, Ecuador, from field measurements and satellite remote sensing. *Journal of Applied Volcanology*. **5**(8): 1–11. Doi: 10.1186/s13617-016-0048-z.

Nussbaum, S., and Menz, G., (2008). *Object-based image analysis and treaty verification*. In: New Approaches in Remote Sensing - Applied to Nuclear Facilities in Iran. Springer, Heidelberg. 218pp.

Offer, R., Zhihao, Q., Yevgeny, D., and Arnon, K. (2014). Derivation of Land Surface Temperature for Landsat 8 TIRS Using a Split Window Algorithm. **4**:5768–5780.

Oppenheimer, C., and Gezahegn Yirgu (2002). Thermal imaging of an active lava lake: Erta 'Ale volcano, Ethiopia. *International Journal of Remote Sensing*. **23**(22): 4777–4782. Doi: 10.1080/01431160110114637.

Oppenheimer, C., and Francis, P. (1997). Remote sensing of heat, lava and fumarole emissions from Erta 'Ale volcano, Ethiopia. *International Journal of Remote Sensing*. **18**: 1661–1692.

Perez Hoyos, I.C. (2014). Comparison between Land Surface Temperature Retrieval Using Classification Based Emissivity and NDVI Based Emissivity. *Int. Jour. of Recent Dev't. in Engi. and Tech.* **2**(2):26–30.

Prata, A.J. (1993). Surface temperatures derived from the Advanced Very High-Resolution Radiometer and the Along Track Scanning Radiometer. *Journal of Geophysical Research*. **98**: 16689–16702.

Prata, A.J. (1994). Land surface temperatures derived from the Advanced Very High-Resolution Radiometer and the Along-Track Scanning Radiometer 2. Experimental results and validation of AVHRR algorithms. *Journal of Geophysical Research*. **99**: 13025–13058.

Qin, Q., Zhang, N., Nan, P., and Chai, L. (2011). Geothermal area detection using Landsat ETM+ thermal infrared data and its mechanistic analysis–A case study in Teng Chong, China. *International Journal of Applied Earth Observation and Geoinformation.* **13**: 552–559.

Ring, U. (2014). The East African Rift System. *Austrian Journal of Earth Sciences.* **107**(1):132–146.

Rosen, P.A., Hensley, S., Zebker, H.A., Webb, F.H., and Fielding, E.J. (1996). Surface deformation and coherence measurements of Kilauea Volcano, Hawaii, from SIR-C radar interferometry. *Journal of Geophysical Research*. **101**(E10): 23109−23125.

Rossi, C., Minet, C., Fritz, T., Eineder, M., and Bamler, R. (2016). Temporal monitoring of subglacial volcanoes with TanDEM-X–Application to the 2014–2015 eruption within the Bárðarbunga volcanic system, Iceland. *Remote Sensing of Environment.* **181**: 186–197.

Rothery, D. A., Francis, P. W., and Wood, C. A. (1988 a). Volcano monitoring using short wavelength infrared data from satellites. *Journal of Geophysical Research*. **93**: 7993–8008.

Rothery, D. A., Francis, P. W., and Wood, C. A. (1988 b). Emitted short wavelength infrared radiation for detection and monitoring of volcanic activity. Signature Spectral D'Objets en Teledetection Aussois, 18–22 Janvier 1988 (Toulouse, ESA). 399– 402.

Roy, D. P., Wulder, M. A., Loveland, T. R., Woodcock, C. E., Allen, R. G., Anderson, M. C., and Scambos, T. A. (2014). Landsat 8: Science and product vision for terrestrial global change research. *Remote Sensing of Environment*. **145**. 154–172.

Rozenstein, O., Qin, Z., Derimian, Y., and Karnieli, A. (2014). Derivation of land surface temperature for Landsat-8 TIRS using a split window Algorithm. *Sensors*, **14**(4): 5768–5780.

Sentinel-2 MSI. (2015). Product Types". European Space Agency.

Sentinel-3 online, (2018). SLSTR, land surface temperature application. https://sentinel.esa.int/ web/sentinel/ user-guides/ sentinel-3- slstr/overview /geophysical- measurements/ land-surface-temperature. Accessed online on May 1, 2018.

Simpkin, T. & Siebert, L. (1994). *Volcanoes of the World*. 2nd ed.**,** Tucson**,** Geoscience Press for the Smithsonian Institution. xi + 349 pp.

Sobrino, J. A., Li, Z. L., Stoll, M. P., and Becker, F. (1996). Multi-channel and multi-angle algorithms for estimating sea and land surface temperature with ATSR data. *International Journal of Remote Sensing.* **17**(11): 2089–2114.

Sobrino, J. A., Caselles, V., and Becker, F. (1990). Significance of the remotely sensed thermal infrared measurements obtained over a citrus orchard. *ISPRS Journal of Photogrammetry and Remote Sensing.* **44**: 343–354.

Sobrino, J. A., Jimenez-munoz, J. C., Labed-nachbrand, J., and Nerry, F. (2002). Surface emissivity retrieval from Digital Airborne Imaging Spectrometer data. *Journal of Geophysical. Research.* **107**: 4729.

Sobrino, J.A., Jimenez-munoz, J.C., Elkharraz, J., Gomez, M., Romaguera, M., and Soria, G. (2004). Single-channel and two-channel methods for land surface temperature retrieval from DAIS data and its application to the Barrax site. *International Journal of Remote Sensing*. **25**(1): 215–230.

Sobrino, J.A., Jiménez-Muñoz, J.C., Sòria, G., Romaguera, M., Guanter, L., Moreno, J., Plaza, A., and Martínez, P. (2008). Land Surface Emissivity Retrieval from Different VNIR and TIR Sensors. *IEEE transactions on geoscience and remote sensing*. **46**(2): 316–327.

Spampinato, L., Oppenheimer, C., Calvari, S., Cannata, A., and Montalto, P. (2008). Lava lake surface characterization by thermal imaging: Erta 'Ale volcano (Ethiopia). *Geochemistry Geophysics Geosystem*. **9**: Q12008. Doi:10.1029/2008GC002164.

Sparks, R.S. J., Aspinall, W.P., Crosweller, H.S., and Hincks, T.K. (2013). Risk and uncertainty assessment of volcanic hazards. *Cambridge University Press*. 364–397. DOI: 10.1017/CBO9781139047562.012.

Tatjana, V., Kanjir, U., and Oštir, K. (2011). Object-Based Image Analysis of Remote Sensing Data. *Geodetski ves tnik.* 55(4): 665−688.

Thouret, J.C. (1999). Volcanic geomorphology—an overview. *Earth-Science Reviews*. **47**: 95–131.

Tian, J., Yan, Y. and Chen, S.B., (2004). The advances in the application of the remote sensing technique to the estimation of vegetation fractional cover. *Remote Sensing for Land and Resources*. **59**: 1–5.

Varet, J., (1973). Geology of Northern Afar (Ethiopia) CNRS-CNR Afar Team y c. *Rev. Geogr. Phys. Geol. Dyn*. **15**(2)**:** 443–490.

Wadge, G., Biggs, J., Lloyd, R., and Kendall, J. M. (2016). Historical Volcanism and the State of Stress in the East African Rift System. *Front. Earth Sci.* **4**(86). Doi: 10.3389/feart.2016.00086.

Wang, M., Zhang, Z., He, G., Wang, G., Long, T., and Peng, Y. (2016). An enhanced single-channel algorithm for retrieving land surface temperature from Landsat series data. *Journal of Geophysical Research. Atmosphere.* **121**: 11712–11722. Doi:10.1002/2016JD025270.

Weng, Q., (2010). *Remote Sensing and GIS Integration Theories, Methods, and Applications*. McGraw-Hill, New York, 433pp.

Xiaolei, Y., Xulin, G., and Zhaocong, W., (2014). Land Surface Temperature Retrieval from Landsat 8 TIRS–Comparison between Radiative Transfer Equation-Based Method, Split Window Algorithm, and Single Channel Method. *Remote sensing*. **6**: 9829–9852.

Yu, X., Guo, X., and Wu, Z. (2014). Land Surface Temperature Retrieval from Landsat 8 TIRS–Comparison between Radiative Transfer Equation-Based Method, Split Window Algorithm, and Single Channel Method. *Remote Sensing.* **6**: 9829-9852. Doi:10.3390/rs6109829.

Zebker, H. A., Amelung, F. and Jonsson, S. (2000). Remote sensing of volcano surface and internal processes using radar interferometry. *Remote Sensing of Active Volcanism*. **116**:179–205.

Zhang, X., Yan, G., Li, Q., Li, Z.-L., Wan, H., and Guo, Z., (2006). Evaluating the fraction of vegetation cover based on NDVI spatial scale correction model, *International Journal of Remote Sensing*. **27**(24): 5359–5372. DOI: 10.1080/01431160600658107.

https://sentinel.esa.int/ web/sentinel/user-guides/ sentinel-2-msi/ data-formats.

https:// sentinel. esa.int/ web /sentinel/ user-guides /sentinel-2-msi /resolutions /radiometric.

http:// landsathandbook.gsfc.nasa.gov.

http:// www.npl.co.uk /reference /faqs /what-is- emissivity -and- why- is- it- important- (faq-thermal.